Analysis, Development, and Control of Multi-Degree-of-Freedom Passive Haptic Devices

by

Maciej Łącki

A thesis submitted to the School of Graduate and Postdoctoral Studies in partial fulfillment of the requirements for the degree of

Master of Applied Science in Mechanical Engineering

University of Ontario Institute of Technology (Ontario Tech University)
Faculty of Engineering and Applied Science
Oshawa, Ontario, Canada
August 2020

Thesis Examination Information

Submitted by:

Maciej Łącki

Master of Applied Science in Mechanical Engineering

Thesis Title:

Analysis, Development, and Control of Multi-Degree-of-Freedom Passive Haptic Devices

An oral defense of this thesis took place on August 6, 2020 in front of the following examining committee:

Examining Committee

Chair of Examining Committee	Dr. Martin Agelin-Chaab
Research Supervisor	Dr. Carlos Rossa
Examining Committee Member	Dr. Scott Nokleby
Examining Committee Member	Dr. Jaho Seo
Thesis Examiner	Dr. Andrew Hogue

The above committee determined that the thesis is acceptable in form and content and that a satisfactory knowledge of the field covered by the thesis was demonstrated by the candidate during an oral examination. A signed copy of the Certificate of Approval is available from the School of Graduate and Postdoctoral Studies.

Abstract

STABILITY and transparency are key design requirements in haptic devices. Replacing conventional electric motors with passive actuators such as brakes or dampers can improve both stability and transparency as passive actuators can display a wide range of impedance while guaranteeing stability. However, passive haptic devices suffer from a serious drawback; their force output is difficult to control. This issue was addressed extensively for planar manipulators but devices with higher degrees-of-freedom (DOF) have not been examined. This thesis proposes a generalized framework for analyzing and controlling higher-DOF devices and examining the effects of the kinematic structure on the force output capability. A first of its kind 3-Degree-of-Freedom (DOF) parallel passive haptic device was developed along with a novel controller designed specifically for the 3-DOF passive device. This thesis also investigates the use of a nonlinear disturbance observer to aid in the control of passive haptic devices.

Keywords: Haptics, Force-Feedback, Passive Actuators, Brakes, Performance Metrics, Force Approximation, Force Estimation

Author's Declaration

I hereby declare that this thesis consists of original work of which I have authored. This is a true copy of the thesis, including any required final revisions, as accepted by my examiners.

I authorize the University of Ontario Institute of Technology (Ontario Tech University) to lend this thesis to other institutions or individuals for the purpose of scholarly research. I further authorize University of Ontario Institute of Technology (Ontario Tech University) to reproduce this thesis by photocopying or by other means, in total or in part, at the request of other institutions or individuals for the purpose of scholarly research. I understand that my thesis will be made electronically available to the public.

Statement of Contribution

Parts of the work described in this thesis have been published in peer-reviewed journal, conferences, and academic books.

Chapter 1

M. Łącki and C. Rossa, "Towards the Ideal Haptic Device: Review of Actuation Techniques for Human-Robot Interactions," in Human-Robot Interaction: Control, Analysis, and Design, Cambridge University Press, [in press]

Chapter 2

M. Łącki and C. Rossa, "On the feasibility of multi-degree-of-freedom haptic devices using passive actuators," in IEEE Int. Conf. on Intell. Robots and Syst. (IROS), Nov 2019, 10.1109/IROS40897.2019.8968164 pp. 7282–7287. Macau, China.

Chapter 3

M. Łącki, B. DeBoon, and C. Rossa, "Impact of kinematic structure on the force displayability of planar passive haptic devices," IEEE Transactions on Haptics, 10.1109/TOH.2020.2970906, vol. 13, no. 1, pp. 219–225, 2020. Also, selected for presentation at 2020 Haptic Symposium.

Chapter 4

M. Łącki and C. Rossa, "Design and Control of a 3 Degree-of-Freedom Parallel Passive Haptic Device," IEEE Transactions on Haptics, 10.1109/TOH.2020.2983037, [in press].

I performed the theoretical analysis, simulations, experimental work, device construction, and majority of manuscripts writing, for contents of all chapters. BD wrote one section of paper constituting chapter 2 (section not included in the thesis) and helped in editing the original manuscript. CR helped in theoretical analysis, experiment design, and editing the manuscripts.

Acknowledgments

THIS thesis is a culmination of two years of hard work by me and the people who actively helped me along the way. First, I would like to thank my thesis supervisor, Dr. Carlos Rossa, for providing numerous opportunities, challenges, the help, the invaluable guidance, and for the countless hours spent in his office trying to solve problems. I am also grateful for his harsh but fair and useful feedback, when it comes to text, in plentiful quantities; For adding ever more words to the titles of our papers; For patiently correcting each *then* to *than* and vice versa; For removing hundreds of commas. Most of all I am thankful for Dr. Rossa persevering with me over the past two years even though, or especially when, I did not make it easy.

Thanks also go out to my lab mates Brayden DeBoon, Brayden Kent, Olivia, and Rick who helped me along the way by listening to my problems, offering advice, and, on more than one occasion, reading my papers and correcting my appalling spelling. I am also thankful for all the chats we had, especially the ones less related to our work, which brightened long days of work.

I would also like to thank all the people who indirectly helped me along the way. Thanks go to my family, particularly my Mom and my Grandma, whose encouragement and support helped me especially in the most hectic times. For their understanding when I responded with *It's complicated* to their questions about my work. I would like to also thank Tomasz and Nina Maczugowie, whose selfless kindness and generosity helped me in my academic journey.

Table of Contents

List of Figures

List of Tables

List of Abbreviations and Symbols

Abbreviations	
DOF	Degrees-of-Freedom
DOD	Degree-of-Displayability
NDO	Nonlinear Disturbance Observer

Symbols (all chapters)	
θ_i	angular position of actuator i
$\boldsymbol{\theta}$	vector of all angular positions
τ_i	torque at the actuator i
τ_a	applied torque
τ_d	desired torque
$\circ$	Hadamard product
B	damping of the virtual environment
b	viscous damping of the device
$\mathbf{F}_{out}$	force output of a device
$\mathbf{F}_{in}$	force applied to a device by a user
H	Heaviside step function
$\mathbf{J}$	Jacobian matrix
J	polar moment of inertia
K	stiffness of the virtual environment
$\mathbf{N}$	net force
$\mathbf{N}_d$	desired net force
$\mathbf{R}_i$	reference force resulting from applying τ_i (excluding Chapter 2)
sgn	Signum function
T	sampling period
$\dot{\square}$	first time directive of x
$\ddot{\square}$	second time directive x

Symbols in **Chapter 1**	
α_{obs}	velocity coefficient
α_i	scaling factor for force approximation
η_t	mechanical transparency
τ_r	torque applied to the real tool
τ_v	torque applied to the virtual tool
θ_r	position of the real tool
θ_v	position of the virtual tool
$\dot{\theta}_d$	velocity of the virtual coupling
τ_c	torque between the virtual coupling and the virtual environment
b	viscous damping of a device
b_b	controllable viscous damping
B_c	viscous damping of the virtual coupling
E_{obs}	energy exchange observed
H	virtual environment
K_c	stiffness of the virtual coupling
Z	mechanical impedance
Z_v	impedance of virtual environment
Z_d	desired impedance
Z_a	applied impedance
Z_{max}	maximum impedance generated by a device
Z_{min}	minimum impedance generated by a device
Z_L	impedance resulting from losses
Z_u	user modeled as passive impedance

Symbols in **Chapter 2**	
α_n	scaling factor of a partially displayable reference force
β_n	controllable parameter for a stationary brake
η	relative size of a region

i	number of actuators
k	number of partially displayable regions
$\mathbf{P}$	end-effector position and orientation
$\mathbf{R}_{V_i}$	reference velocity vector for actuator i
$\mathbf{R}_{F_i}$	reference force vector for actuator i
$\mathbf{T}$	transformation matrix of forward kinematics
$\mathbf{V}$	end-effector velocity

Symbols in **Chapter 3**

α	angle between velocity and positive x axis
$\boldsymbol{\mu}$	vector of area fractions of regions with varying displayability
$\boldsymbol{\mu}_a$	mean value of $\boldsymbol{\mu}$ for all values of ϕ_a
$\bar{\boldsymbol{\mu}}$	mean value of $\boldsymbol{\mu}_a$ for all values of α_a
ϕ	angle between velocity and the desired force
A	area
$\mathbf{A}$	vector of all area components
A_t	total workspace area
l_i	length of link i
$\mathbf{P}$	point in workspace satisfying desired constraint
r_l, θ_k, σ_k	polar coordinates of the device workspace
$\square_n$	relates to non-displayable region
$\square_p$	relates to the partially displayable region
$\square_d$	relates to the displayable region

Symbols in **Chapter 4**

α_i	scaling factor for reference force i in a passive haptic device
β_f	torque scaling factor for the fully displayable case
θ_{ij}	the angular position of joint i in leg j
ϕ_i	angle between the base frame and link a of leg i
a, b, c, d, e	link lengths of the device

f, g, r, s	
$t_i, l_{0i}, l_{1i}, l_{2i}$	variables used in half tangent substitution
a_i	scaling factor for reference force i
c	net force constant
d	surface penetration depth
E	error between the estimated and actual position
G	adaptive scaling factor for damped Newton's Method
$\mathbf{L}_r$	range of possible solutions satisfying the sliding constraint
$\mathbf{L}$	direction vector of $\mathbf{L}_r$
$\mathbf{N}^{\perp}$	component of normal force perpendicular to the virtual surface
$\mathbf{N}_d$	desired Net force
$\mathbf{N}_d^*$	intersection point between $\mathbf{L}$ and $\mathbf{N}_i$
$\mathbf{N}_d'$	projection of $\mathbf{N}_d$ onto plane defined by $\mathbf{P}$
$\mathbf{X}_{xyz}$	position of the end-effector
$\mathbf{X}_{uvw_i}$	attachment point position of leg i in uvw_i reference frame
$\mathbf{O}$	origin of the spherical surface
$\mathbf{P}$	normal unit vector of a plane
$\hat{\mathbf{u}}$	unit vector normal to the virtual surface
U_i, V_i, W_i	components of $\mathbf{X}_{uvw_i}$
$\mathbf{X}_f$	vertical offset of the plane from workspace origin
r	radius of the spherical surface
$\square_p$	refers to an inclined plane
$\square_{vex}$	refers to convex surface
$\square_{con}$	refers to concave surface

Symbols in **Chapter 5**

α_h	lower excitation threshold
β_h	upper excitation threshold
$\boldsymbol{\tau}_{in}$	torque input
$\hat{\boldsymbol{\tau}}_{in}$	estimate of disturbance torque

$\boldsymbol{\tau}_a$	torque applied
$\gamma_{\alpha,\beta}$	hysteron in Preisach model
$\mu(\alpha, \beta)$	Preisach density function
c	NDO gain
c_d	viscous damping of the actuator
$\mathbf{C}$	Coriolis and centrifugal matrix
$\mathbf{G}$	gravity vector
I_m	mass moment of inertia of the end-effector
$\mathbf{L}$	NDO gain matrix
$\mathbf{M}$	inertia matrix
m_a	mass of link a
m_b	mass of link b
m_c	mass of the end-effector
$\mathbf{p}$	NDO auxiliary variable
t	input into a nonideal relay
y	output of a nonideal relay
$\mathbf{z}$	internal states of the observer

Chapter 1

Towards the Ideal Haptic Device:

Review of Actuation Techniques for Human-Machine Interfaces

THE kinesthetic sense of touch plays a key role in humans' capability to perform even basic tasks [1]. In some situations, like in teleoperated surgery [2–4], fly-by-wire [5], drive-by-wire systems [6, 7], or surgical simulation [8–12], the mechanical linkage between the user and the tool is broken or inexistent. In such situations, haptic force-feedback devices can restore the connection between the user and the tool, virtually.

Haptic devices are robotic manipulators designed to provide force-feedback to a human user. A haptic device acts like a universal coupling between a virtual or distant tool and the user by conveying the dynamics and the forces acting on the tool to the user, like in Fig. 1.1(a). From a control perspective, the interaction between the user and the virtual tool can be represented as a network diagram as in Fig. 1.1(c). In a haptic force-feedback system, the device captures the motion of the user θ_r and transmits it to the virtual environment. Based on the transmitted motion, the virtual environment simulates the motion of a virtual tool θ_v. As the user moves the device, the virtual tool can encounter an object which may impede its motion. The virtual environment determines the desired torques τ_v required to render the mechanical impedance acting on the tool $Z_v = \tau_v/\dot{\theta}_v$ [13–15]. This signal is then sent to the haptic device which generates a torque τ_r.

An ideal haptic device should accurately transmit the position and forces between the virtual environment and the user i.e., it should act as a universal coupling such that

$$\begin{bmatrix} \tau_v \\ \theta_r \end{bmatrix} = \begin{bmatrix} h_{11} & h_{12} \\ h_{21} & h_{22} \end{bmatrix} \begin{bmatrix} \theta_v \\ \tau_r \end{bmatrix} \tag{1.1}$$

where $h_{21} = h_{12} = 1$ and $h_{11} = h_{22} = 0$, resulting in $\tau_r = \tau_v$ and $\theta_r = \theta_v$. To this end, the device should render objects with an infinite range of impedance, infinite bandwidth, experience no delays, all the while having no dynamic losses, and no discernible mass m or inertia J.

Being physical objects, haptic devices have a mass and they are subject to losses such as viscous friction causing $h_{11} \neq 0$ and as such $\tau_r \neq \tau_v$. Furthermore, as digital

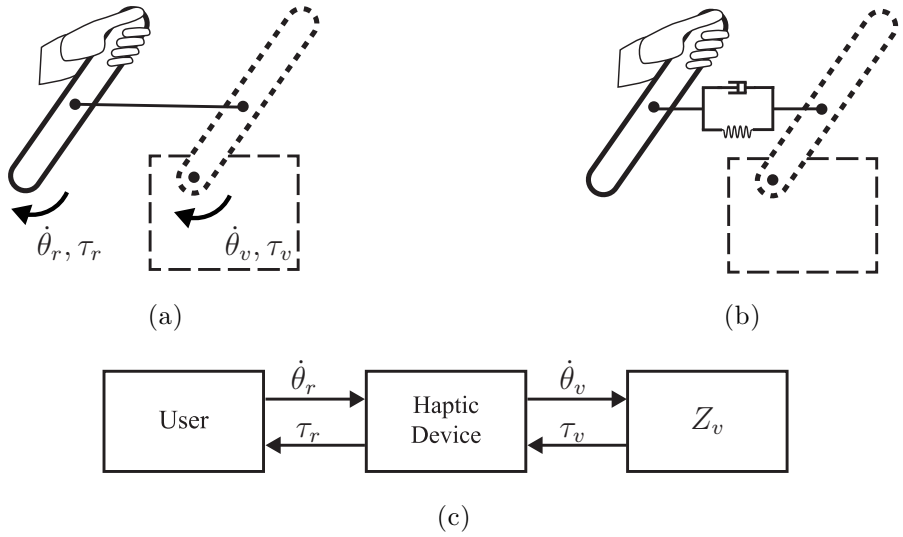

Figure 1.1: Universal coupling shown in (a) conveys the motion and forces acting on the virtual tool (dashed) to the user. A haptic device functions according to (c) where Z_v represents the virtual environment, $\dot{\theta}_r$ and $\dot{\theta}_v$ the user and the virtual tool motion, while τ_r and τ_v are the torques acting on the user and on the virtual tool. In reality, the coupling between the user and the tool reassembles the one shown in (b), where the spring-damper system represents the viscous friction and the rigidity of the device.

systems, their position measurements are subject to delays resulting from quantization and discretization of continuous signals, meaning that $h_{21} \neq 1$ and $\theta_r \neq \theta_v$.

The performance of a haptic device can be assessed against the ideal device using mainly three metrics. First, the mechanical transparency defined as [16],

$$\eta_t = \frac{Z_d}{Z_a} \tag{1.2}$$

where Z_d represents the desired impedance and Z_a the output impedance, quantifies the disparity between the generated impedance and the desired impedance. In other words, (1.2) measures the distortion of the output force resulting from mechanical imperfections and limitations of the physical mechanism. An ideal device should be transparent, meaning that there should be no difference between the desired and the output impedance, i.e, $Z_a = Z_d$, results in $\eta_t = 1$. However, the impedance of the device, represented by Z_L, results in $Z_d/(Z_a + Z_L) < 1$.

Second, the Z-width is a measure of haptic device's impedance range defined as [17]

$$\eta_z = \frac{Z_{max}}{Z_{min}} \tag{1.3}$$

where Z_{max} and Z_{min} respectively represent the maximum and the minimum impedance generated by the device. An ideal device should render impedances varying from zero to infinity, thus, ideally $\eta_z \to \infty$ [17, 18]. The device's inertia and friction, however, mean that $Z_{min} = Z_L \neq 0$ and the physical limitations of the actuators mean that Z_{max} is finite, resulting in η_z with a finite value.

Lastly, the bandwidth is the frequency range of force generated by the device. Low-frequency, high-amplitude forces render the geometry of a virtual object while minute details of the shapes, like their texture, are rendered using low-impedance at high-frequencies. An ideal device with an infinite bandwidth can render both shape and its texture. As a result of inertia and delays in the actuators, haptic devices are typically able to render only a finite band of frequencies. This band may be situated either in the lower or higher end of the frequency spectrum constraining the device to rendering either low or high frequency forces.

Consider the model of a haptic system shown in Fig. 1.2. A user moves the haptic device, which has an inertia J and a viscous damping b, to interact with a virtual environment $H(z)$ modelled as a stiff virtual wall with some damping characteristics. The virtual wall cannot exert energy on the user in excess of what is provided to it, i.e., the environment acts as a passive impedance $H(z) = Z(v)$ [18]. The user is the only source of energy in the haptic loop. From the perspective of a haptic device, however, the user impedes motion and, in fact, stabilizes the haptic device. The user is, therefore, modelled as a passive impedance Z_u [13, 14, 19–22]. Since all components in Fig. 1.2 are passive, the entire system should be passive as well [23]. Note, however, that the virtual environment is a discrete system that measures the position of the user θ at a sampling period of T. The actuator acts like a zero-order-hold function, $(1-e^{-Ts})/s$, converting the discrete desired torque into a continuous signal. The delay induced by the discretization of a continuous signal injects energy into an otherwise passive system possibly leading to instability.

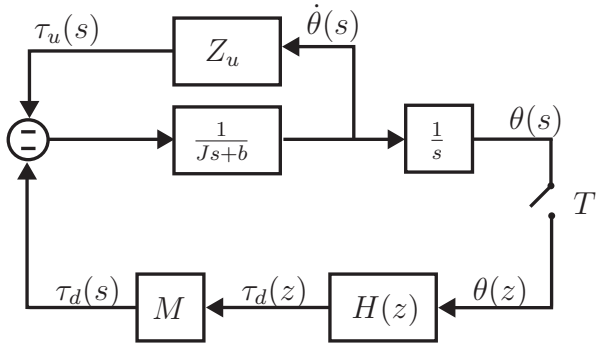

Figure 1.2: The user, modelled as impedance Z_u, applies $\tau_u(s)$ to the device with inertia J and damping b, resulting in angular velocity $\dot{\theta}(s)$. The position $\theta(s)$ is sampled at a sampling period T, resulting in a discrete position signal $\theta(z)$, which is conveyed to the virtual environment $H(z)$. The virtual environment calculates the desired torque $\tau_d(z)$ and directs it to the motor M, which acts like a zero-order-hold function $(1-e^{-Ts})/s$, converting it into a continuous signal $\tau_d(s)$.

The response of the haptic loop to the injected energy depends on the type of actuator used. Conventional haptic devices, for instance, use electric motors to generate forces. As it will be shown in Section 1.1, to maintain stability these devices need to dissipate energy, through viscous damping, proportionally to the impedance of the virtual environment. Due to the presence of damping, active haptic devices have a limited upper and lower bound of the Z-width and as a result they cannot be perfectly transparent. Passive actuators, on the other hand, only dissipate energy making them intrinsically stable. As a result, passive devices have higher Z-width and transparency than active devices. Their inherent passivity, however, limits the forces they can generate as they cannot restore energy to the user, as discussed in Section 1.2. Haptic devices equipped with hybrid actuators, ones comprising motors, brakes, and other components, can generate a wider Z-width than active devices and they do not suffer from the same limitations as purely passive or active devices. Section 1.3, discusses various implementations of hybrid actuators as well as their associated control schemes. The limitations, challenges, and considerations associated with active, passive, and hybrid actuation methods are addressed in Section 1.4. Finally, Section 1.5 provides recommendations and applications for each type of actuator.

1.1 Active Actuators

Conventional haptic devices, which includes all devices on today's market, use active actuators, most commonly DC motors [7, 18, 24–26], to render impedances. These actuators rely on an external source of energy to generate forces allowing them to provide energy to the system. These actuators are relatively inexpensive and exhibit a relatively linear current response making them easy to control [27]. Electric motors, however, tend to generate relatively small torque and often rely on gearboxes or capstan transmissions to amplify the torque. The gearboxes increase the inertia, amplify viscous friction, and introduce nonlinearities [28–30].

Specialized haptic interfaces can use other types of active actuators. A planar device presented in [31] uses linear induction motors to render forces in the plane of the desk. The actuators in this type of system do not move but, instead, generate a magnetic field which results in a force applied directly to the tool. Since there is no mechanical linkage between the tool and the actuator, these devices can be very transparent, but their force range is relatively small [32]. Air muscles are another type of active actuator. They generate force by expanding or contracting like human muscles using compressed air. Air muscles generate high forces while having relatively low mass, but due to the compressibility of air they experience delays and a nonlinear force response making them difficult to control [33, 34]. Irrespective of the actuator, however, there is an inherent trade-off between the stability and transparency of an active haptic device.

1.1.1 The Trade-off Between Stability and Transparency

For an illustrative example, consider a haptic loop composed of a haptic device with a typical sampling rate $T = 1$ kHz [35] rendering a virtual environment composed of a relatively soft spring with a stiffness of $K = 500$ kN/m. The user approaches the virtual wall at a steady speed $\dot{x} = 100$ mm/s. Assume that at sample $k = n$ the distance between the user and the virtual wall $\Delta x = 0$ mm and no force is applied to

impede the user. At $k = n + 1$ the user moved $\Delta x = -100$ μm into the wall which should require an energy input of 50 J. Even though the user has not provided any significant energy into the system, the virtual environment exerts 10 N of force on the user. The excessive force generated by the device pushes the user out of the wall at a rapid velocity and leads to instability [36, 37].

To minimize the amount of energy injected into the system, the resolution of position sensors must be maximized, the sampling delay minimized, and the velocity signal must be filtered [17]. Reducing the amount of injected energy, however, will not stabilize the haptic system as stability requires dissipation of all the excess energy. Haptic devices can only dissipate energy through mechanical losses in the form of viscous damping b. The amount of friction required to stabilize the device depends on the sampling period of the control loop and the impedance of the environment. For a haptic device to be stable it must satisfy the *stability condition*, defined as

$$b > \frac{TK}{2} + B \tag{1.4}$$

where B and K respectively represent the viscous damping and stiffness of the virtual wall [18]. In other words, the impedance range of an active haptic device depends on its ability to dissipate energy. Since energy is only dissipated through viscous damping, an active haptic device cannot be perfectly transparent while maintaining stability.

1.1.2 Stabilizing Active Haptic Devices

The stable impedance range of an active haptic device can be expanded beyond the limit imposed by the stability condition (1.4) by using specifically developed control schemes. There are two methods of extending the impedance range: rejecting the excess energy resulting from delays or filtering the force output of the virtual environment using a virtual coupling.

Virtual Coupling: Let us replace the rigid universal coupling in Fig. 1.1(a) with a

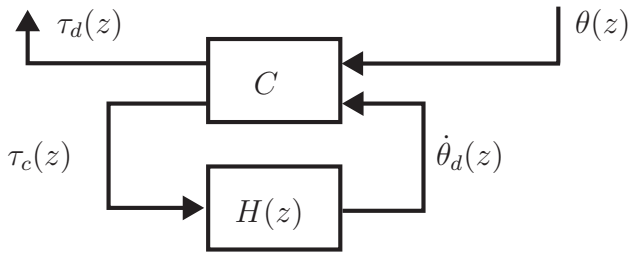

Figure 1.3: The virtual coupling C acts as an intermediary between the main haptic loop and the virtual environment $H(z)$ in Fig. 1.2. The torque applied to the user $\tau_d(z)$ is a function of the user position $\theta(z)$ and the velocity of the virtual coupling $\dot{\theta}_d(z)$, while $\tau_c(z)$ is the force between virtual environment.

coupling comprised of a spring with stiffness K_c and a damper with a viscous friction coefficient B_c connected in parallel like in Fig. 1.1(b). As a result, a user in contact with an infinitely stiff virtual wall will not sense the impedance of the virtual wall but instead the impedance of the virtual coupling. In other words, the desired torque τ_d is not directly determined by the virtual environment, but instead by the coupling such that

$$\begin{bmatrix} \tau_d(z) \\ \tau_c(z) \end{bmatrix} = \begin{bmatrix} -\frac{K_c T z}{z-1} - B_c & K_c + \frac{B_c(z-1)}{Tz} \\ -\frac{K_c T z}{z-1} - B_c & K_c + \frac{B_c(z-1)}{Tz} \end{bmatrix} \begin{bmatrix} \dot{\theta}_d(z) \\ \theta(z) \end{bmatrix} \tag{1.5}$$

where τ_c and $\dot{\theta}_d$ are the torque and velocity, respectively, between the coupling and the virtual environment [15, 38, 39].

The coupling effectively acts like a filter that limits the maximum impedance displayed to the user guaranteeing system stability [15]. However, it limits the maximum impedance of the haptic device, while also introducing a discrepancy between the position of the real and the virtual tools [40]. These limitations can be avoided altogether if the actuator is restricted from providing energy in excess to that provided by the user.

Passivity Observation and Control: In an interaction with a virtual wall the energy provided by the user to the system is calculated using a passivity observer,

$$E_{obs}(n) = T \sum_{k=0}^{n} \tau_{in}(k)\ \dot{\theta}(k) \tag{1.6}$$

where τ_{in} is the force input of the user and k represents some sampling period between zero and n. For the device to be passive $E_{obs} < 0\ \forall k$. Given an estimate of system energy and the desired torque τ_d, the torque output of the device becomes,

$$\tau_a = \tau_d + \alpha_{obs}\dot{\theta} \tag{1.7}$$

where

$$\alpha_{obs} = \begin{cases} \dfrac{-E_{obs}}{T\dot{\theta}} & \text{if } E_{obs} > 0 \\ 0 & \text{otherwise} \end{cases} \tag{1.8}$$

which virtually dissipates the energy injected by the delay [40, 41].

The time-domain passivity observer was improved in [42–45] and adapted for multi-DOF devices in [46]. Eliminating excess energy in the haptic device using this scheme is limited by the accuracy of the energy estimation. Thus, the scheme stabilizes a haptic device for a wide, but finite, range of operating conditions [43, 47]. Absolute stability of a haptic device can be achieved by replacing the motor with a device that is physically incapable of providing energy.

1.2 Passive Actuators

A brake is an actuator that generates torque by dissipating kinetic energy making it intrinsically stable. As a result, only the magnitude of a brake's torque can be controlled while the direction depends on its velocity, as indicated in Fig. 1.4 by the diagonal line crossing the brake B. The choice of brake type for a passive haptic device is a key consideration. Friction brakes, commonly used in automotive applications, are not suitable as their response is nonlinear, prone to high hysteresis, and they are difficult to control. Haptic devices, instead, employ electromechanical actuators such

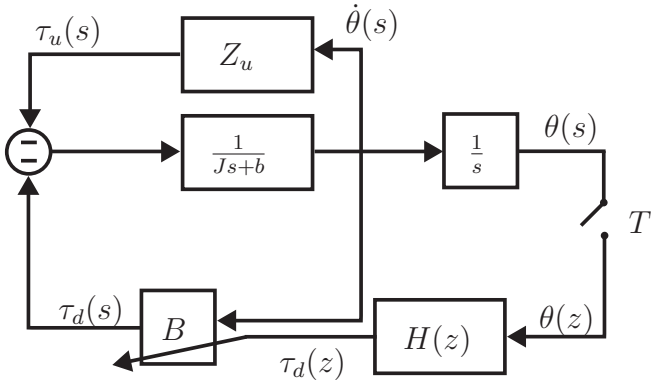

Figure 1.4: The user, modeled as impedance Z_u, applies a torque $\tau_u(s)$ to the device with inertia J and damping b, resulting in angular velocity $\dot{\theta}(s)$. The position $\theta(s)$ is sampled at a sampling period T, resulting in a discrete position signal $\theta(z)$, which is conveyed to the virtual environment $H(z)$. The virtual environment calculates the desired torque $\tau_d(z)$ and directs it to the brake B which acts like a zero-order-hold function $(1 - e^{-Ts})/s$, converting it into a continuous signal $\tau_d(s)$. The brake torque depends on the velocity, thus only the magnitude of torque is controllable, as indicated by the diagonal arrow.

as electrorheological (ER), magnetorheological (MR), eddy current, or particle brakes.

MR and ER brakes use a liquid substance that changes its viscosity under the influence of a magnetic or an electric field, respectively. These brakes generate a wide range of impedance but they suffer from response time greater than that of a motor. ER brakes require high voltages, on the scale of kilovolts, to function, further complicating their control [48, 49]. MR brakes, on the other hand, operate at much lower voltages, but they have a higher off-state torque resulting from the remanent magnetic flux in the core [50]. Both MR and ER brakes have a higher torque-to-mass ratio than DC motors resulting in devices that have a higher Z-width [49, 51–53].

Instead of using a fluid that changes viscosity depending on the magnetic flux, particle brakes use a fine magnetic powder that binds together when subjected to a magnetic field. Moving the rotor through these particles applies a resistive force on the rotor, resulting in torque at the output shaft. Particle brakes are neither as strong nor as efficient as MR or ER brakes, but they have a relatively linear current-torque response [54, 55].

Unlike other actuators employed in haptic applications, eddy current brakes act like

a controllable viscous damper; their torque output depends on the relative velocity of the input and output shafts. An eddy current brake is composed of a rotor made from an electric conductor and a stator generating magnetic field. As the rotor moves through the magnetic field an eddy current is induced, creating a magnetic field that opposes that of the stator [56]. These actuators are easy to control due to their linear current-torque response, fast response time, and minimal losses resulting from the lack of physical connection between the rotor and the stator [57].

Passive actuators offer fast response times, linear current-torque responses, and low energy consumption. As most of these actuators can also generate higher torque than a similarly sized motor, they do not require a gearbox, minimizing losses of the resulting device [58, 59].

There are two major issues involving the use of passive actuators in haptic devices. The first one, stiction, is a result of the difference between the static and the dynamic friction coefficient of physical objects. When a brake stops moving, its torque output increases leading to the rendered objects feeling sticky. Additionally, brake's inability to add energy into the system inhibits them from rendering a force in arbitrary directions.

1.2.1 Force Output of a Passive Haptic Devices

A brake has two modes of operation. When moving, the brake can only generate torque opposing its velocity. While stationary, the torque of the brake opposes any torque input i.e.,

$$\tau_a = \begin{cases} -\operatorname{sgn}(\dot{\theta})|\tau_d| & \text{if } \dot{\theta}\ \tau_d < 0, \quad \dot{\theta} \neq 0 \\ -\operatorname{sgn}(\tau_{in})|\tau_d| & \text{if } \tau_d\ \tau_{in} < 0, \quad \dot{\theta} = 0 \\ 0 & \text{otherwise} \end{cases} \tag{1.9}$$

where τ_{in} is the torque input and τ_a the torque output [60]. Clearly, only the magnitude of the brake's torque is controllable. As a result, passive devices cannot generate a force in an arbitrary direction making them incapable of rendering some virtual

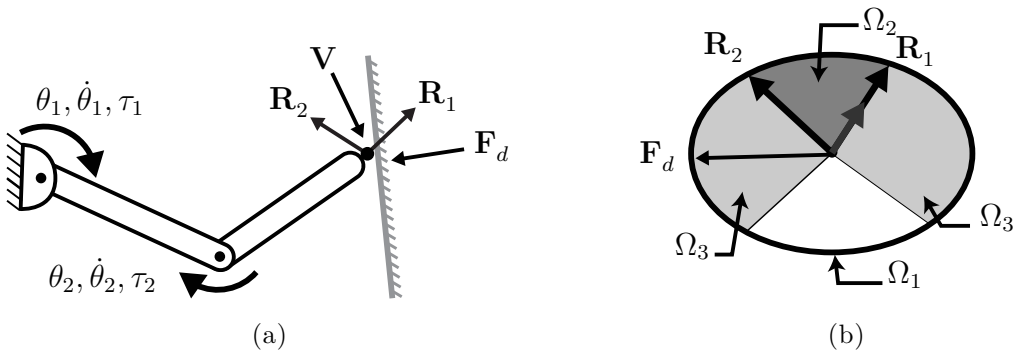

(a) (b)

Figure 1.5: The 2-DOF haptic device in (a) moves with a velocity $\mathbf{V}$ and attempts to render a virtual wall, represented as a grey line, by generating force $\mathbf{F}_d$ using combination $\tau_1 < 0$ and $\tau_2 < 0$ resulting in forces $\mathbf{R}_1$ and $\mathbf{R}_2$, respectively. The device can generate forces in the region Ω_2, compared to the range of an active device represented by Ω_1. Lastly, Ω_3 represents the regions where the passive device can approximate forces.

environments; even ones that are totally passive.

For instance, consider a simple passive environment composed of a linear spring. As the user compresses the spring, the brake opposes the compression by dissipating energy. Assuming that eventually the user stops compressing the spring, the stored energy should be released by applying the force to the user. With a passive device, however, this is impossible as the brake cannot restore energy. The issues with force displayability are further complicated by the nonlinear relationship between the velocity and force at the end-effector, and the angular velocity and torque at the joints.

Consider a 2-DOF device attempting to render a stiff virtual wall with no friction shown in Fig. 1.5(a). The end-effector of the device moves with a velocity $\mathbf{V}$ towards the wall, with which it collides. To render the wall, the device must apply a force $\mathbf{F}_d$, which acts perpendicular to the wall. Through the manipulator kinematics, $\mathbf{V}$ results in $\dot{\theta}_1 > 0$ and $\dot{\theta}_2 > 0$. As a consequence of (1.9), the device can only generate torques such that $\tau_1 < 0$ and $\tau_2 < 0$. Applying only τ_1 results in a force $\mathbf{R}_1$ and applying τ_2 results in $\mathbf{R}_2$, while applying both torques simultaneously results in forces contained in region Ω_2 in Fig. 1.5(b). Since $\mathbf{F}_d$ is not located in Ω_2, the force cannot be rendered even though the desired force opposes velocity i.e., $\mathbf{F}_d \cdot \mathbf{V} < 0$.

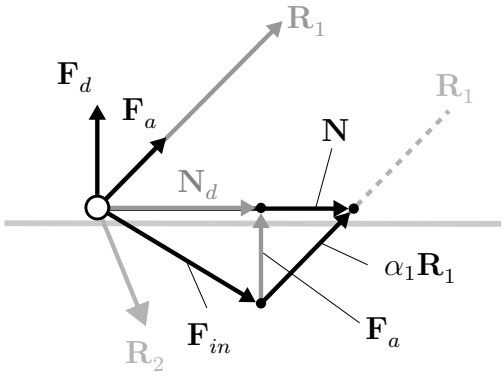

Figure 1.6: When rendering a stiff virtual wall, the force input $\mathbf{F}_{in}$ and the desired force $\mathbf{F}_d$ should result in a net force at the end-effector $\mathbf{N}_d$, parallel to the surface. If $\mathbf{F}_d$ cannot be rendered, one of the actuators, $\mathbf{R}_1$ in this case, can be used to apply a force that will result in the net force on the end-effector $\mathbf{N}$ parallel to $\mathbf{N}_d$.

1.2.2 Improving Force Output of a Passive Haptic Devices

The controllers intended for passive haptic devices must address the two key issues: limited range of displayable forces and stiction. To date, two types of controllers have been developed to address these two issues.

Alternate Brake Locking: The first class of control methods for passive haptic devices locks all but one brake to induce motion along a single DOF path to approximate the motion of the virtual object [61]. The control scheme was refined in [62] where a narrow band above the virtual surface was introduced. Inside of the band, the controller switches the actuated and the un-actuated brake, creating a zig-zag motion approximating the geometry of the surface. These controllers eliminate stiction, as there is always at least one brake allowing free motion, by approximating the motion along the virtual surface; a trait that motivated the development of other controllers for passive haptic devices.

Force Approximation: As an alternative, it is possible to approximate a desired force by imitating its effects using a displayable force, increasing the displayable force range to Ω_3 in Fig. 1.5(b). Originally developed for underactuated wire-based devices [63], the force approximation scheme was refined and adapted for 2-DOF passive

device in [64].

Consider Fig. 1.6, where the user applies a force $\mathbf{F}_{in}$ into the end-effector which is in contact with a stiff, frictionless virtual wall. By applying the desired force, the user is stopped from penetrating the virtual environment resulting in the net force on the end-effector $\mathbf{N}_d$ acting parallel to the surface and preventing penetration. The device cannot render the desired force, however, it is possible to generate a force $\mathbf{F}$ such that the resulting net force is also parallel to the virtual surface. This is achieved by determining the magnitude of a scaling factor

$$\alpha_i = -\frac{\mathbf{F}_d \cdot \mathbf{F}_{in}}{\mathbf{F}_d \cdot \mathbf{R}_i} \tag{1.10}$$

such that $\mathbf{F} = \mathbf{R}_1 \alpha_i$, like in Fig. 1.6 [64]. Apart from increasing the displayable range of forces, this control scheme eliminates stiction since the net force at the end-effector induces sliding along the virtual surface.

For the force approximation scheme to work, the controller must have an accurate estimate of the user input force, thus, requiring a heavy, noisy, and costly force sensor [65, 66]. The reliance on the force sensor can be reduced using a modified force approximation scheme, presented in [66], where the energy of the system is used to calculate α.

Force approximation control of the passive device increases the range of displayable forces and eliminates stiction; addressing the main issues of a passive haptic device.

1.3 Hybrid Actuators

Passive haptic devices are intrinsically stable but they cannot restore energy to the user or generate forces in arbitrary directions. Active devices, in contrast, generate forces in arbitrary directions but the magnitude of the impedance they can render is constrained to a narrow stability range. A hybrid transducer combines the advantages of both motors and brakes. Hybrid actuators can be designed with combinations

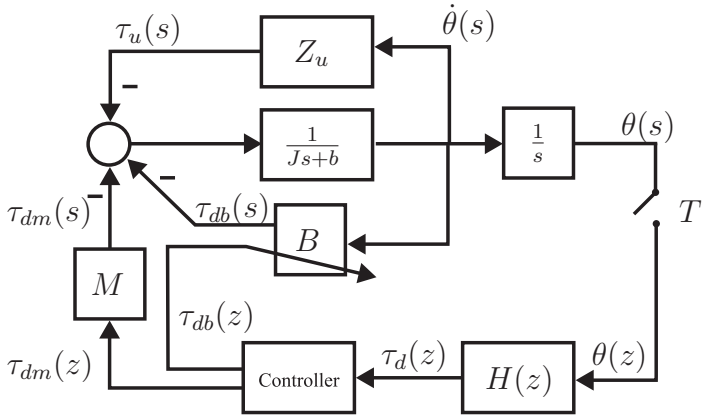

Figure 1.7: The user, modelled as an impedance Z_u, applies a torque $\tau_u(s)$ to the device with inertia J and damping b, resulting in angular velocity $\dot{\theta}(s)$. The position $\theta(s)$ is sampled at a sampling period T, creating a discrete position signal $\theta(z)$, which is conveyed to the virtual environment $H(z)$. The virtual environment calculates the desired torque $\tau_d(z)$ and sends it to the controller, which divides the desired torque into $\tau_{db}(z)$ and $\tau_{dm}(z)$ directed to the brake B and the motor M, respectively. The two actuators convert the discrete signal into a continuous one using the zero-order-hold function $(1-e^{-Ts})/s$, resulting in $\tau_{db}(s)$ and $\tau_{dm}(s)$. The brake torque depends on the velocity, thus only the magnitude of its torque is controllable, as indicated by the diagonal arrow.

of active and passive actuators as well as using dampers [67, 68], springs [55], and transmissions [69]. These actuators increase the Z-width of a haptic device in one of two ways: increase the maximum impedance Z_{max} by improving the stability and force range of the actuators, or by minimizing inertia and mechanical losses to lower the minimum impedance Z_{min}.

The cross-section view of several hybrid actuator configurations are shown in Fig. 1.8. The user interacts with the end-effector represented by a black dot connected to the actuator shaft, shown as an empty narrow rectangle. Actuators, represented by pairs of blocks labelled 'B' for brakes and 'M' for motors, apply the torque to the shaft.

1.3.1 Increasing the High End of the Z-width (Z_{max})

The actuator shown in Fig. 1.8(a) is the most common hybrid configuration for haptic devices [26, 70–75], where a motor and a brake are connected to the same shaft in parallel. The fusion of the two actuators allows the system to render high impedance

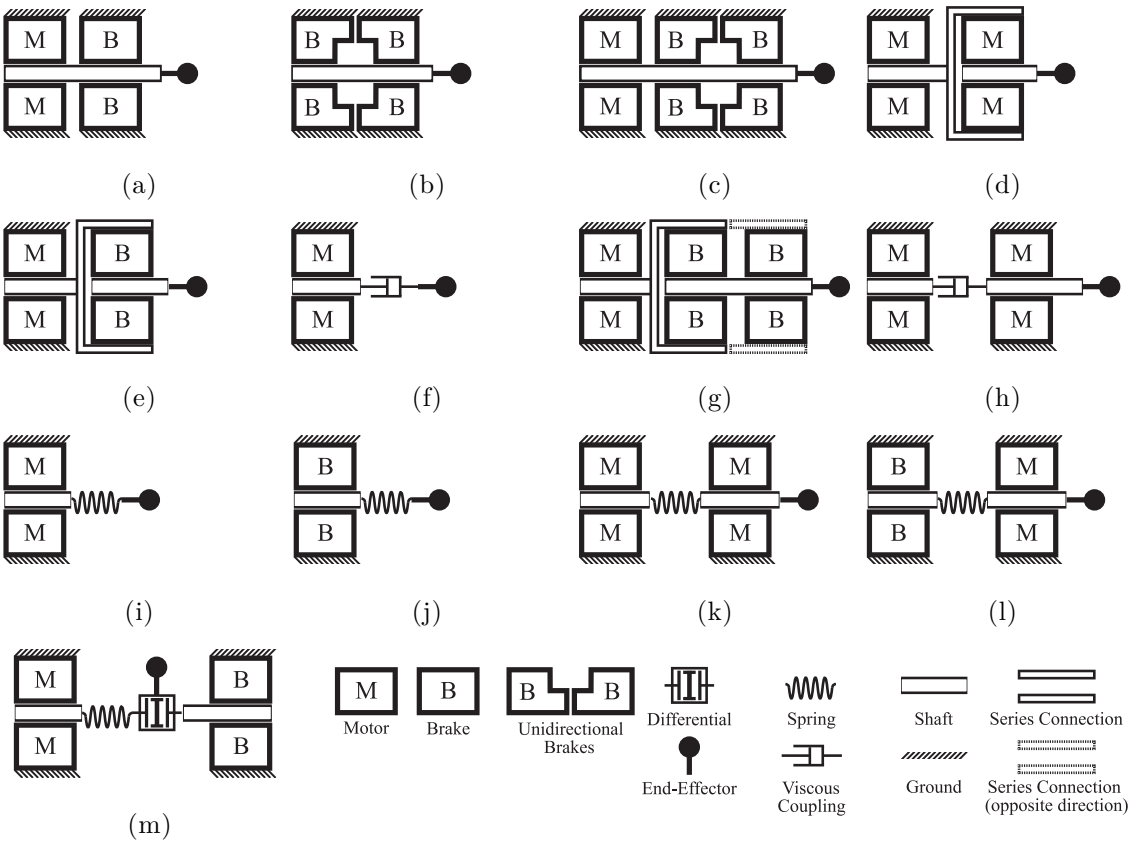

Figure 1.8: Schematic cross-section view of hybrid actuators. The user interacts with the end-effector represented by a black circle connected to the actuator shaft, shown as a hollow narrow rectangle. Brakes, labelled 'B', and motors, 'M', may be attached to the housing, represented by dashed lines, like in (a), or to the shaft of another actuator, represented by a 'U' shaped bracket like in (d). A geared serial connection that rotates in the direction opposite to the shaft, like the one in (g) is indicated by dashed lines. Other components like springs, viscous dampers, unidirectional brakes, and differential are represented using symbols shown above.

in many directions while maintaining stability. Note, however, that the use of two actuators increases the total inertia $J_{total} = J_m + J_b$. Additionally, this actuator is prone to stiction just like the brake alone.

One way of addressing the issue of stiction is the same as with a passive device; adding a force sensor and releasing the brake when needed. Another method of eliminating stiction was proposed in [76], where two unidirectional brakes were used in parallel in a passive device, as shown in (b). Each unidirectional brake, represented by an 'L' shaped block 'B', can generate torque in only one direction. Consequently, impeding the user's motion in one direction does not affect his ability to move in the other direction. This design was modified to include an electric motor in [77], resulting in configuration (c).

The maximum torque τ_{max}, of parallel hybrid actuators varies from the peak torque of the motor τ_m to the peak torque of both the motor and the brake τ_b, depending on the control scheme. For instance, one way to increase the maximum impedance of the device is to use a brake as a programmable damper b_b so that the stability condition becomes [26, 57, 73],

$$b + b_b > \frac{TK}{2} + B. \tag{1.11}$$

Assuming that b_b is sufficiently high to satisfy the stability condition, the maximum torque of the actuator is limited only by the torque of the motor. Considering that brakes can often generate higher torque than a similar-sized motor, a controller capable of utilizing the brake alongside the motor should further increase Z_{max} of this hybrid configuration.

Another class of control scheme for parallel hybrid actuators divides the torque output between the motor and the brake. The energy-bounding approach [77] employs an energy observer to determine the total energy of the system. If the energy is negative, the system is passive and the motor generates the desired torque. If, however, the energy becomes positive, the torque is directed to the brake which dissipates the

energy. The controller guarantees stability but it still underutilizes the brake. This issue was addressed in the same paper by stiffness-bounding algorithm [77]. The controller estimates the stiffness and damping of the virtual environment, compares the estimated stiffness to the limit imposed by (1.4) and uses the motor to render the maximum stable stiffness while the remainder is rendered by the brake. In [78, 79], a low-pass filter feeds the desired position to the brake, while the motor renders high-frequency, low-amplitude forces. As a result, the brake generates most of the torque output improving stability, increasing Z_{max}, and reducing the actuator response time. Lastly, the controller presented in [80] uses an artificial neural network to determine the optimal division of torque among the two actuators by considering motor stability, brake's ability to generate forces, and model-based friction compensation. As a result, this controller not only increases Z_{max} but it also lowers Z_{min}.

1.3.2 Lowering the Low End of the Z-width (Z_{min})

Using the parallel configurations in Fig. 1.8(a) or (c) with a large brake for rendering impedance and a small motor for friction [74, 81, 82], gravity [83], inertia [84] compensation, can improve the lower end of the Z-width Z_{min}. The motor can also compensate for the response time of the brake increasing the bandwidth of the device [75]. These compensation schemes will reduce the apparent inertia and friction allowing the user to better sense low impedances.

Parallel hybrid actuators are intrinsically limited in their ability to render the lower boundary of the Z-width and high-frequency torques. As the frequency of the torque increases, the compensation of friction and inertia becomes more challenging due to the limited response time of the motors. There are, however, hybrid actuator arrangements designed specifically for rendering low impedances at high frequencies.

The configuration (d) referred to as the micro-macro or course-fine manipulator, introduced in [85, 86] and adapted for haptic applications in [87, 88], uses a large grounded motor (the macro manipulator) to move a smaller motor (micro manipulator) coupled directly to the end-effector. Since there is no direct connection between the larger

motor and the end-effector, the user senses the inertia and friction of the smaller motor. The smaller motor responds quickly and, thus, is able to render a high-frequency impedance. Note that the torque developed by the smaller motor is also the maximum torque of the actuator, thus it cannot render a high impedance.

To increase the impedance range, the smaller motor can be replaced by a small brake, like in (e) [89], or a controllable damper similar to (f) [67]. The brake, acting as a clutch or a viscous damper controls the torque transmission between the motor and the user. Much like configuration (d), it can generate a high-frequency impedance, but the upper torque limit is bounded by the brake [67,89]. As opposed to the micro-macro manipulator, this configuration struggles to render forces in arbitrary directions. The brake can rapidly change the amount of torque provided to the user but only if the direction of motion stays constant. Once the direction changes, the macro actuator must change its direction of motion, introducing additional response latency. Adding a second brake connected to a shaft spinning in the opposite direction, like in (g), eliminates this issue [90].

In configuration (h), a large motor is connected to an eddy current brake, acting as viscous coupling, and to a smaller motor [68]. Like in the previous examples, the large motor provides high torques, while the eddy current brake controls the amount of torque transmitted to the end-effector. The smaller motor, on the other hand, compensates for the delay introduced by the eddy current brake. When interacting with the device, the user only senses the inertia and friction of the smaller motor.

1.3.3 Other Hybrid Configurations

Series Elastic Actuators (SEA) form another class of hybrid actuators characterized by inclusion of elastic elements in their design. The simplest forms of SEAs, in Fig. 1.8(i) and (j) combine, respectively, a motor or a brake connected in series with a spring. The presence of the spring decouples the dynamics of the actuator from the end-effector. As a result, the apparent inertia is reduced and the torque output is controlled through deflection of the spring. The compliance introduced by the

spring makes it unsuitable for haptic applications. A refined design, presented in (k), eliminates the issue of deflection by adding a second motor into the design. The first motor can apply a torque directly to the user, while the second motor controls the energy stored in the spring. The torque of the spring and the torque of the first motor sum together exposing the user to the inertia of just the first motor.

By replacing one of the motors with a brake, like in (l), the device can also collect energy from the user while minimizing energy consumption [55]. The device presented in [55] uses a large brake to control the energy stored in the spring enabling it to both dissipate and restore energy. The motor, on the other hand, activates only when the torque in the spring acts opposite to the desired torque. In such a situation, the motor provides the torque to the user, while the brake dissipates the energy stored in the spring.

Lastly, a design proposed in [69] uses a motor connected to a high reduction gearbox connected in series with a spring, like in (i), with a brake and a differential, as shown in (m). This configuration provides multiple operating modes for the actuator. When the brake is unlocked and the motor is stationary, the user can move the end-effector freely while perceiving only the inertia of brake and the differential. By locking the brake, all the energy provided by the user is stored by the spring. Both the brake and the motor can control the amount of energy stored by the spring and the torque exerted on the user.

Clearly, there are many hybrid actuator designs, many of which have properties desirable in haptic devices. Let us now discuss the design considerations, challenges, and opportunities related to the design of haptic devices using active, passive, and hybrid actuators.

1.4 Discussion

Most, if not all, haptic devices available today use only active actuators despite their limitations [7,91–95]. Passive and hybrid actuation techniques are an alternative that

can improve stability, impedance range, and bandwidth of a haptic interface. To develop devices using these actuation techniques, however, a designer must consider a number of challenges and fundamental limitations of each type of actuator.

1.4.1 Passive Haptic Devices

Due to their high torque-to-mass ratio and relatively low response time, MR or ER brakes are the most suitable passive actuators for haptic applications. These actuators, however, must be custom designed and built due to their limited market availability [51, 52]. Particle brakes, in contrast, have a lower torque-to-mass ratio but they are widely available for purchase making them far easier to implement [54, 55].

Passive haptic devices are difficult to design and control due to their restricted range of displayable forces as well as the fact they are prone to stiction. To date, most passive haptic devices are constrained to planar 2-DOF [58, 61, 62, 64, 66, 96–98]. There have been only a handful of attempts at developing higher DOF devices, which included four 3-DOF devices [53, 99, 100], one 4-DOF [101], and one 6-DOF device [102] as shown in Fig. 1.9. Apart from the device introduced in [99] which uses the energy based control developed for 2-DOF devices in [66], the higher-DOF devices do not seem to be using any control scheme capable of improving their force output range through force approximation or limit constriction.

Apart from force approximation, the range of displayable forces a passive haptic device generates can be increased by redundantly actuating the device [96,97,103,104]. Note, however, that even a redundantly actuated device will not be able to restore energy to the user, therefore, it will never render forces such that $\mathbf{F} \cdot \mathbf{V} > 0$, as it would require the brake to add energy into the system. Adding additional actuators also increases the friction and inertia of the device.

A passive device must always be equipped with a force sensor further increasing its mass. The reliance on the force sensor varies from requiring accurate measurement of the force at all times in [64] to only requiring the force measurement when the device sticks [66], but the sensor is an indispensable component of the device.

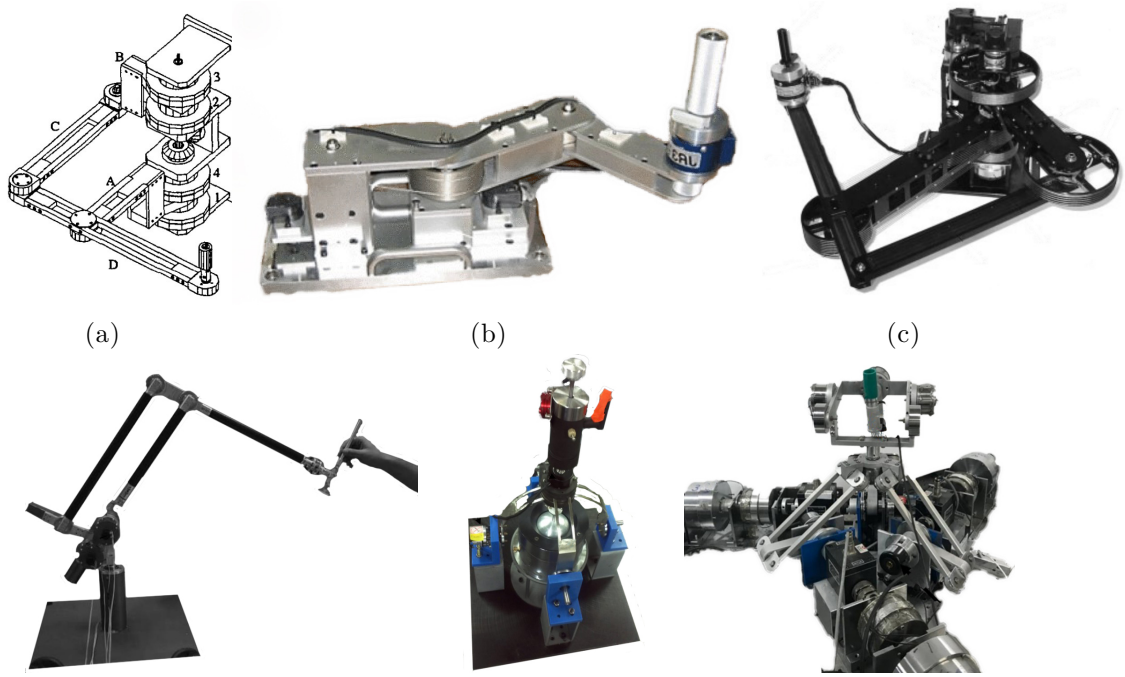

Figure 1.9: Passive haptic devices with varying design characteristics. The device shown in (a) has a 5-bar parallel kinematic structure with 2 planar DOF and 4 clutches, making it over-actuated (©2004 IEEE) [103]. (b) shows a 2-DOF device constructed by Cho *et al.* in [66]. It has a serial kinematic structure and uses a tendon-drive to actuate the second link (©2007 IEEE). Another device designed by Cho *et al.* is shown in (c). This device uses a 2-DOF parallel kinematic structure and like the device shown in (a), it is over-actuated with 4 brakes (©2005 Wiley) [96]. The device shown in (d) is a 3-DOF device using a 5-bar regional kinematic structure actuated by 3 MR brakes (©2011 Massachusetts Institute of Technology) [96]. (e) shows a 4-DOF passive haptic device with 3 rotational DOF, provided by a spherical ER brake, and one translational DOF actuated by an ER piston brake (©2013 IOP Publishing) [101]. The device shown in (f) has 6 decoupled DOF. It uses a modified delta kinematic structure for the 3-DOF translational motion with an attachment for the 3 rotational DOF, actuated by MR brakes (©2018 Elsevier) [102].

The mass of a planar passive device working perpendicular to the force of gravity does not affect transparency. For higher DOF devices, however, gravity becomes a significant concern that can be compensated using one of two passive methods. The first method attempts to statically balance each link using a counterweight, such that the sum of moments due to gravity on any link is zero [105]. Adding counterweights increases the inertia of the device leading to a poorer display of low impedances. Alternatively, the moment at each link can be balanced by springs attached to the links of the device [106]. This method is not as effective at canceling the forces of gravity, but it does not increase the inertia of the device.

1.4.2 Hybrid Haptic Devices

There are few documented haptic devices using hybrid actuators. The devices developed thus far spanned from 2-DOF [75, 75, 107, 108], 3-DOF [33, 55, 109], and one partially hybrid 6-DOF device [110]. The lack of multi-DOF hybrid devices suggests that the design of such devices poses a considerable challenge.

The first challenge is the selection of a hybrid actuator configuration. There are numerous configurations with varying characteristics and no single configuration can simultaneously expand the top and bottom ends of the device's Z-width; the two objectives are in conflict. Parallel hybrid actuators are the most suitable for the majority of haptic devices as they can easily replace electric motors. Serial actuators, on the other hand, have limited utility due to the relatively low forces they generate.

The second challenge pertains to the use of hybrid actuators in multi-DOF devices. Hybrid actuators have a much higher mass and volume than either a brake or a motor, which can increase the inertia of the resulting haptic devices. For a higher-DOF device to remain transparent, they must use active inertia compensation schemes [84] or hardware designs that minimize the inertia caused by the actuators. To this end, the motion of the actuator relative to the base of the device must be eliminated using one of the following two methods. Tendon drives convey torque of a motor to a distant joint through tension of the 'tendon' connecting the two [111]. This method increases

the complexity of the mechanism and introduces nonlinearities making the resulting device more difficult to control [112]. Parallel kinematic structures, on the other hand, connect multiple kinematic chains together, such that only the first joint in each link requires actuation [113]. The reduced inertia of the device comes at the expense of the workspace size, as parallel manipulators have smaller workspace than comparable serial configurations.

The next challenge relates to control. There is no single universal control scheme addressing all the issues of a hybrid haptic device. The control schemes developed thus far focus on addressing a subset of associated issues and limitations. An optimal control scheme for hybrid actuators should use both the motor and the brake to render high impedances. The brake should always stabilize the motor, while the motor should compensate for the friction, inertia, and gravity of the haptic system. Preferably, the majority of the torque should be generated using the brake to minimize energy consumption. The optimal control scheme should not require high computational power, such that it can be implemented on a standard micro-controller.

1.5 Conclusions

An ideal haptic device has no mass, no inertia, no friction, infinite bandwidth, and it can render a wide range of impedance. Currently, active actuators are the predominant actuation method for haptic devices, but they are known to have a limited impedance range due to stability concerns. Passive actuators, on the other hand, are intrinsically stable so they can generate higher impedance ranges. Their inability to generate energy, however, promotes stiction and limits the direction of forces they can generate. Hybrid actuators generate force in arbitrary directions while maintaining stability when rendering high impedance.

Each type of actuator has key characteristics that make it uniquely suitable for specific haptic applications. For instance, active haptic devices are the simplest type to implement due to their relatively simple construction and control. This makes them

ideal for low-cost interfaces, where the stability and accuracy of the force reproduction are of lesser importance. Active devices will most likely find use in applications like gaming, computer control, or computer-based visual design, among many others. The key attribute of passive haptic devices, on the other hand, is their unparalleled stability. This makes them ideal for mission-critical applications, where stability is paramount to haptic fidelity. These applications include automotive driver's assistance, guiding systems for surgical applications, and master devices for teleoperation robots. Finally, hybrid devices have the widest Z-width that is, theoretically, only bounded by the physical actuator limitations. Depending on the configuration, these hybrid actuators can improve the low or the high end of the impedance range. The low impedance configurations are well suited for rendering textures and the subtle forces such as the ones involved in neurosurgery. Simulators and teleoperated systems, on the other hand, benefit from the high impedance variants of hybrid actuators, since they can accurately render impedance acting on the virtual or teleoperated tool.

Of various actuation techniques, the passive actuators are the best choice for medical applications. For instance, the intrinsic stability of these devices makes them ideal for teleoperated robotic surgery where any instability may jeopardize the life of a patient. On the other hand, the transparency of passive devices can aid in the development of surgical simulators which require minimal damping to be realistic [8,114–116]. Majority of these applications, however, require devices with at least 3 translational DOF. As discussed previously, there have been only a handful of attempts at developing such passive haptic devices. This is possibly due to the lack of control schemes for passive haptic devices with more than 2-DOF, the lack of guidelines for the design of these devices, and their reliance on the force sensors.

1.6 Thesis Objectives and Outline

The goal of this thesis is to develop a new passive haptic device with 3-DOF for tele-operated robotic surgery and surgical simulation, specifically designed for the percutaneous nephrolithotomy (PCNL) simulator presented in [8]. To achieve this, the device must have at least 3 translational DOF, with an option of adding additional DOF later, and at least 15 cm of vertical workspace to enable the user to freely interact with a virtual patient. To render contact with human tissue, the device needs to generate a minimum force of 10 N. Additionally the device needs to have minimal viscous damping, and low inertia to make it transparent to the user. In pursuit of this goal the thesis builds on the analysis and control techniques developed for planar devices by leveraging unique displayability regions found in higher DOF haptic devices.

First, a feasibility analysis of higher-DOF passive haptic devices is presented in **Chapter 2**. The analysis reveals the challenges associated with increasing the number of DOF in a passive haptic device focusing on the force displayability and force approximation. The chapter introduces a new concept, called *Degree-of-Displayability*, which helps to describe various partially displayable regions found in higher DOF devices. The findings of this chapter pave the way for the design of controller for haptic devices with more than 3 DOF.

Next, **Chapter 3** investigates the impact of the kinematic structure on force displayability of planar passive haptic device. Using novel performance metrics designed to measure the ability of a passive haptic device to generate a force in an arbitrary direction a comparison of planar serial and parallel manipulators is performed. The chapter compares the force displayability of devices with serial and parallel kinematic structures and provides design guidelines for their use.

Chapter 4 documents the design of a novel 3-DOF passive haptic device and the development of a new controller. The device uses a parallel kinematic structure making it the first parallel passive haptic device with 3 spatial DOF. The controller devel-

oped for the device eliminates stiction and expands the range of displayable forces by adapting the force approximation scheme designed for 2-DOF devices to 3-DOF devices. A series of experiments involving the 3-DOF device proves the effectiveness of the proposed controller.

Next, **Chapter 5** attempts to tackle one of the major drawbacks of the controller proposed in Chapter 4, namely the reliance on the force measurement. To this end a nonlinear disturbance observer (NDO) is proposed to estimate the user's force input. The proposed NDO is evaluated using a series of simulations to test its ability to render a wide range of force inputs. Simulation results show that the observer can estimate the force input and can effectively replace a force sensor under certain operating conditions. Furthermore, it is shown that despite the error between the force input and its estimate NDO produces similar results as the use of the actual force input.

Finally, **Chapter 6** concludes the thesis with discussion of significant contribution and a set of recommendations for further development and improvements of passive haptic devices.

Chapter 2

Feasibility of Multi-DOF Passive Haptic Devices:

Evaluation of Control Challenges in Higher Degree-of-Freedom Passive Haptic Devices

ROBOTIC surgery and surgical simulators require devices that can produce forces in at least the three spatial dimensions. Yet, as discussed in Chapter 1, the majority of passive haptic devices are constrained to planar 2-DOF which leads to a question: Are multi-DOF, non-redundant passive manipulators feasible? To answer this question, this chapter proposes an analytical framework for passive haptic devices with any number of DOF to identify different workspace regions where forces can be displayed or approximated as well as regions where the force cannot be generated at all. Based on the analysis, the challenges and opportunities associated with developing higher DOF passive haptic devices are discussed.

2.1 Force Modelling of Passive Haptic Devices

Let us begin our analysis by examining the behaviour of a 2-DOF, non-redundant, passive manipulator.

2.1.1 Passivity Constraint

The force produced by a brake is a result of energy dissipation. For instance, applying a brake in a moving vehicle results in a force acting opposite to the car's direction of motion. If a force is applied to a stationary vehicle the brake will produce a force equal and opposite to the applied force. A haptic device using brakes behaves in much the same way. Typically, the brakes used in haptic devices are rotary; instead of linear velocity they experience an angular velocity $\dot{\theta}$, and instead of force they produce a torque τ_{out}. When a brake is moving ($\dot{\theta} \neq 0$), the torque it produces is:

$$\tau_{out} = \begin{cases} -\operatorname{sgn}(\dot{\theta})|\tau_a| & \text{if } \operatorname{sgn}(\dot{\theta}) \neq \operatorname{sgn}(\tau_d) \\ 0 & \text{otherwise} \end{cases} \tag{2.1}$$

In other words, a brake can only generate a desired torque τ_d if its direction opposes that of its angular velocity, i.e. $\tau_d\ \dot{\theta} < 0$ [60]. When the brake is stationary ($\dot{\theta} = 0$) the output torque opposes the torque input τ_{in}, thus,

$$\tau_{out} = \begin{cases} -\operatorname{sgn}(\tau_{in})|\tau_d| & \text{if } \operatorname{sgn}(\tau_{in}) \neq \operatorname{sgn}(\tau_d) \\ 0 & \text{otherwise} \end{cases} \tag{2.2}$$

Throughout this chapter, (2.1) and (2.2) will be referred together as the *Passivity Constraint*. To create a force at the end-effector an actuator must satisfy this constraint.

Now, consider the 2-DOF manipulator shown in Fig. 2.1, which has one brake at each joint. The end-effector of the device is moving with a velocity $\mathbf{V}_1$ while attempting to generate either a force $\mathbf{F}_{d_1}$ or $\mathbf{F}_{d_2}$. In order to apply the passivity constraint to the device, one must first relate the torque and angular velocity at each joint to the force and velocity at the end effector.

2.1.2 Manipulator Kinematics

Let $\mathbf{T} \in \mathbb{R}^{j\times 1}$ represent a transformation matrix relating the angular position of each joint to the position and orientation $\mathbf{P} \in \mathbb{R}^{j\times 1} = \mathbf{T}(\boldsymbol{\theta})$ of the end effector where $\boldsymbol{\theta} = [\theta_1 \ \theta_2 \ \cdots \ \theta_i]^{\mathrm{T}}$ and for a non-redundant, non-under-actuated device $j = 1, 2, \cdots, i$. This convention will be used through the chapter. Similarly, let $\mathbf{J} \in \mathbb{R}^{j\times i}$ represent a Jacobian matrix relating angular velocity to the linear velocity $\mathbf{V} \in \mathbb{R}^{j\times 1} = \mathbf{J}\,\dot{\boldsymbol{\theta}}$ of the end effector, where $J_{nm} = \partial \mathbf{T}_m / \partial \theta_n$, and $\dot{\boldsymbol{\theta}} = d\boldsymbol{\theta}/dt$ with $1 \leq m, n \leq j$. This chapter will only consider non-redundant manipulators ($i = j$) the Jacobian is a square matrix.

The inverse transpose of the Jacobian matrix relates the torque of all joints to the force at the end effector:

$$\mathbf{F} = \left(\mathbf{J}^{-1}\right)^{\mathrm{T}} \boldsymbol{\tau} \tag{2.3}$$

where $\mathbf{F} \in \mathbb{R}^{j\times 1}$ [117]. Using these relationships one can apply the passivity constraint to each joint thereby identifying regions in the workspace where the passivity constraint is satisfied, that is, the torque and velocity at a given joint have opposite

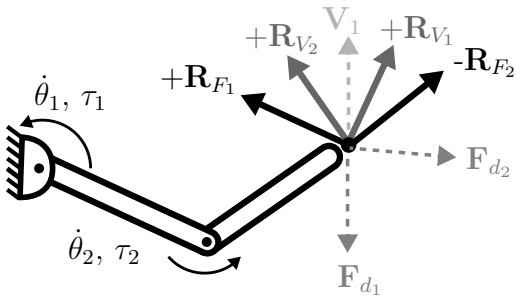

Figure 2.1: The reference vectors, desired force, and velocities acting on a 2-DOF manipulator, where each joint is actuated.

directions. The boundaries or these regions can be found using the reference vectors described below.

2.1.3 Reference Vectors

Going back to Fig. 2.1, the vectors $+\mathbf{R}_{V_1}$ and $+\mathbf{R}_{V_2}$ are the velocities resulting from positive (counter-clockwise) motion of either joint 1 or 2 whereas the other joint is not moving, i.e., $+\mathbf{R}_{V_1} = \mathbf{J}[1\ 0]^{\mathrm{T}}$ (with $\dot{\theta}_1 = 1$ and $\dot{\theta}_2 = 0$), and $+\mathbf{R}_{V_2} = \mathbf{J}[0\ 1]^{\mathrm{T}}$. Let us call vectors obtained using this operation *Reference Velocity Vectors*. Note that this operation simply extracted the n^{th} column from the Jacobian Matrix. Therefore, the reference velocity vectors are the column space of the Jacobian Matrix:

$$\mathbf{J} = \begin{bmatrix} J_{x_1} & J_{x_2} & \cdots & J_{x_i} \\ J_{y_1} & J_{y_2} & & J_{y_i} \\ \vdots & & \ddots & \vdots \\ \underbrace{J_{\gamma_1}}_{\mathbf{R}_{V_1}} & \underbrace{J_{\gamma_2}}_{\mathbf{R}_{V_2}} & \cdots & \underbrace{J_{\gamma_i}}_{\mathbf{R}_{V_n}} \end{bmatrix}_{j \times i} \tag{2.4}$$

Applying the same procedure to torques and forces gives $+\mathbf{R}_{F_1} = (\mathbf{J}^{-1})^{\mathrm{T}}[1\ 0]^{\mathrm{T}}$ with $\tau_1 = 1$ and $\tau_2 = 0$ and $+\mathbf{R}_{F_2} = (\mathbf{J}^{-1})^{\mathrm{T}}[0\ 1]^{\mathrm{T}}$. Let us call these vectors the *Reference Force Vectors* (see Fig. 2.1). Together, they determine the sign of angular velocity and torque resulting from the velocity and force at the end-effector as shown in Fig. 2.2. For example, from Fig. 2.2(a), it is clear that so long as $\mathbf{V}_1$ is within $+\mathbf{R}_{V_1}$ and $+\mathbf{R}_{V_2}$, the joint angular velocities are $\dot{\theta}_1 > 0$ and $\dot{\theta}_2 > 0$. Similarly, from Fig. 2.2(b), one

observes the torques required to create $\mathbf{F}_{d_1}$ are $\tau_1 < 0$ and $\tau_2 < 0$. Likewise, $\mathbf{F}_{d_2}$ requires $\tau_1 > 0$ and $\tau_2 < 0$.

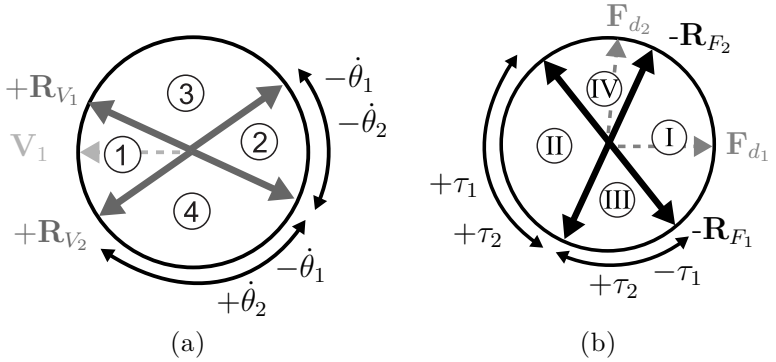

Figure 2.2: Intersecting the velocity vectors in (a) and force vectors in (b) produces region pairs. Regions with matching numbers are fully displayable.

2.1.4 Displayability Regions

As described before, if the force $\mathbf{F}$ and velocity $\mathbf{V}$ have directions comprised between two of the reference vectors, the direction of torques and angular velocity they create do not change. As a result, the workspace may be divided into 4 distinct regions. In Fig. 2.2, these regions are labelled with numbers from I to IV for force, and 1 to 4 for velocity. Force and velocity regions can now be paired according to the passivity constraint.

Fully Displayable Region

In Fig. 2.2(a), the input velocity is in region (1), and the forces the device can display are within region (I) in Fig. 2.2(b). This is because the passivity constraint is satisfied for all actuators. Let us refer to region (1) as the *fully-displayable region*. Notice that the size of the fully-displayable region is always a fraction of the total workspace.

Partially Displayable Regions

Consider again the end-effector moves with a velocity $\mathbf{V}_1$ and the desired force is $\mathbf{F}_{d_2}$. In this case $\theta_1\tau_1 > 0$ and $\theta_2\tau_2 < 0$ and the passivity constraint is only satisfied in one of the joints. In this region, it is necessary to approximate $\mathbf{F}_{d_2}$ using the actuator that

satisfies the constraint. Let us name regions where at least one actuator can be used to approximate the desired force as a *partially displayable region* whose boundaries do not correspond to those from Fig. 2.2(b) and will now be defined.

Fig. 2.3(a) shows the reference force and two desired forces $\mathbf{F}_{d_2}$ and $\mathbf{F}_{d_3}$, both laying in Ⓘⓥ. Since the passivity constraint is not satisfied in joint 1, the only force that the device can create is a component of -$\mathbf{R}_{F_2}$ (i.e. $\tau_1 = 0$, -$\mathbf{R}_{F_1} = 0$). For $\mathbf{F}_{d_2}$, the resulting force output is the projection of $\mathbf{F}_{d_2}$ onto -$\mathbf{R}_{F_2}$ i.e. $\mathbf{F}_{out_2}$, and for $\mathbf{F}_{d_3}$ the output force is $\mathbf{F}_{out_3}$. The output force has the same direction as -$\mathbf{R}_{F_2}$, with magnitude equal to the projection of the desired force on to the reference vector. Note, however, as the angle between the desired force and reference vector approaches 90°, the component of the displayable force tends to zero. Therefore, the output force generated by the n^{th} actuator in the partially displayable region is

$$\mathbf{F}_{out_n} = -\operatorname{sgn}(\dot{\theta}_n)\mathbf{R}_{F_n}\alpha_n \tag{2.5}$$

for $\dot{\theta}_n \neq 0$, and $0 \leq \alpha_n \leq 1$ where α_n is a controllable parameter modifying the magnitude of the output force, i.e.,

$$\alpha_n = \frac{\mathbf{F}_d \cdot \mathbf{R}_{F_n}}{||\mathbf{R}_{F_n}||^2}. \tag{2.6}$$

The boundary of the partially displayable region is a vector orthogonal to the reference force direction. Since the reference velocities are columns of a Jacobian while the reference force vectors are rows of an inverse Jacobian, their product is an identity matrix:

$$\begin{bmatrix} 1 & 0 & 0 \\ 0 & \ddots & 0 \\ 0 & 0 & 1 \end{bmatrix} = \mathbf{J}^{-1}\,\mathbf{J} = \begin{bmatrix} \mathbf{R}_{F_1} \\ \vdots \\ \mathbf{R}_{F_i} \end{bmatrix} \begin{bmatrix} \mathbf{R}_{V_1} & \cdots & \mathbf{R}_{V_i} \end{bmatrix}. \tag{2.7}$$

Note that the multiplication of each term is equivalent to taking a dot product of the corresponding terms. If the dot product is 0 the vectors are orthogonal. Clearly, from the definition of the inverse matrix, each velocity vector is orthogonal to $i - 1$

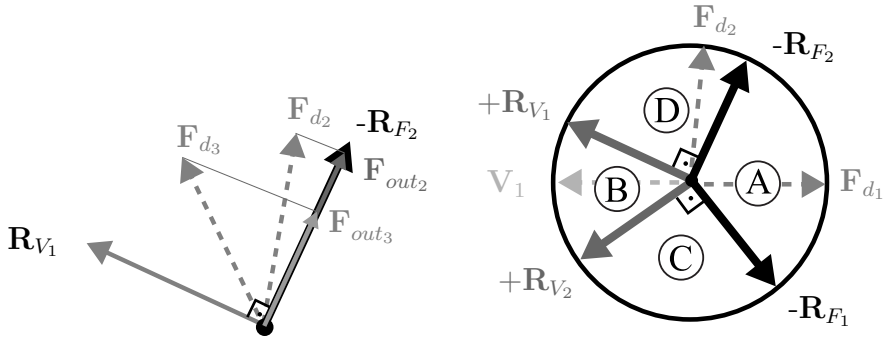

Figure 2.3: (a) A projection of the desired forces along the force reference direction -$\mathbf{R}_{F_2}$. (b) For given velocity, $\mathbf{V}_1$, Ⓘ ≅ Ⓐ is fully displayable, ① ≅ Ⓑ is non-displayable, while Ⓒ and Ⓓ are partly-displayable.

reference force vectors, and vice versa. Therefore, the limit of the partly-displayable region is defined by $\mathbf{R}_{F_i}$ and the $i-1$ orthogonal reference velocity vectors. For the manipulator in Fig. 2.1 the partially-displayable region Ⓒ is bounded by $+\mathbf{R}_{V_1}$ and -$\mathbf{R}_{F_2}$, while region Ⓓ is bounded by $+\mathbf{R}_{V_2}$ and -$\mathbf{R}_{F_1}$.

Non-Displayable Region

The unaccounted range of forces that cannot be generated forms the *non-displayable region*, which is bounded by the velocity reference vector. For instance, the non-displayable region of $\mathbf{V}_1$ is ① ≅ Ⓑ as shown in Fig. 2.3(b).

Uncontrollable Force Output

So far, only a case where actuators are moving was considered. Let us now consider the case where an actuator is stationary. In Fig. 2.4(a), the input velocity $\mathbf{V}_2$ acts along $+\mathbf{R}_{V_1}$, making only the magnitude of -$\mathbf{R}_{F_1}$ controllable. The velocity along $\mathbf{R}_{V_2}$ (and $\dot{\theta}_2$), on the other hand, is zero. As a result, the force along $\mathbf{R}_{F_2}$ is no longer dependent on the velocity of the actuator but per (2.2) it depends only on the force input.

In Fig. 2.4(b), one observes the possible outputs of $\mathbf{R}_{F_2}$ resulting from $\mathbf{F}_{in_1}$ and $\mathbf{F}_{in_2}$. Since force $\mathbf{F}_{in_1}$ acts in line with the reference force direction, $\mathbf{F}_{out_1}$ is equal to -$\mathbf{R}_{F_2}$.

On the other hand, $\mathbf{F}_{in_2}$ acts at an angle from the reference force, resulting in $\mathbf{F}_{out_2}$. The magnitude of the force output is equal to the projection of the force on the reference vector. Similar to the partial force displayed by a moving brake, the force output of a stationary actuator is

$$\mathbf{F}_{out_n} = -\frac{\mathbf{R}_{F_n}(\mathbf{F}_{in} \cdot \mathbf{R}_{F_n})}{||\mathbf{R}_{F_n}||^2}\beta_n \tag{2.8}$$

for $\dot{\theta}_n = 0$, and $\beta_n = \{0, 1\}$. Note that neither the magnitude nor the direction of the force output can be controlled. However, the brake may be turned off by setting $\beta_n = 0$. Whether the brake should be on or off is calculated with:

$$\beta_n = \text{sgn}\left(\left[\mathbf{R}_{F_n}(-\mathbf{F}_{in} \cdot \mathbf{R}_{F_n})\right] \cdot \mathbf{F}_d\right) \tag{2.9}$$

This equation describes the force output of a static actuator and will be combined with (2.5) to form a general form of the output force equation in Section 2.2.

2.2 Modelling a multi-DOF Device

The analysis developed in the previous section can be generalized to model a non-redundant device with n-DOF and determine the total force output. One can also determine all displayability regions found in any non-redundant passive device.

2.2.1 General Form of the Output Force

By combining (2.8) and (2.5) one can describe any force, in any of the displayability regions, for cases where actuators are moving or not, by summing the force output of each actuator i:

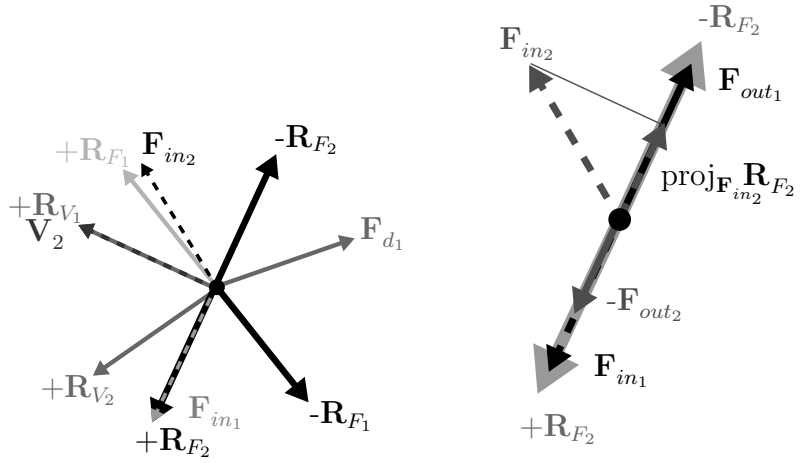

Figure 2.4: (a) Depending on the force input, $\mathbf{F}_d$ can or cannot be produced. (b) Force output of a stationary actuator for different force inputs.

$$\mathbf{F}_{out} = \sum_{n=1}^{i} \begin{cases} -\operatorname{sgn}(\dot{\theta}_n)\mathbf{R}_{F_n}\alpha_n & \text{If } \dot{\theta}_n \neq 0, \\ & \text{and } 0 \leq \alpha_n \leq 1 \\ -\dfrac{\mathbf{R}_{F_n}(\mathbf{F}_{in} \cdot \mathbf{R}_{F_n})}{||\mathbf{R}_{F_n}||^2}\beta_n & \text{If } \dot{\theta}_n = 0, \\ & \text{and } \beta_n = \{0, 1\} \\ 0 & \text{Otherwise.} \end{cases} \tag{2.10}$$

To display $\mathbf{F}_{d_1}$ in Fig. 2.4(a), given $\mathbf{F}_{in_1}$ one must use the output of the stationary and moving actuator. Fig. 2.5b shows that the combined force output of the two actuators generates $\mathbf{F}_{out_1}$, which has the same direction as the $\mathbf{F}_{d_1}$. Note, however, that the magnitude of $\mathbf{F}_{out_1}$ is different from the magnitude of the desired force. As shown in Fig. 2.5a, the controllable force adds to the stationary actuator force and together they generate $\mathbf{F}_{out}$ = -$\mathbf{R}_{F_2}$-$\mathbf{R}_{F_1}\alpha_i$. Note, however, that one can only control either the magnitude or the direction of $\mathbf{F}_{out}$, but not both.

In contrast, when the same desired force is to be displayed with $\mathbf{F}_{in_2}$ acting on the device, the stationary brake must be off ($\beta_2 = 0$). The brake opposes the desired force, as shown in Fig. 2.5b, and the force output is the force of moving brake, i.e., $\mathbf{F}_{out_2}$=-$\mathbf{R}_{F_1}$ α. Further, (2.10) can be used to determine the number and type of

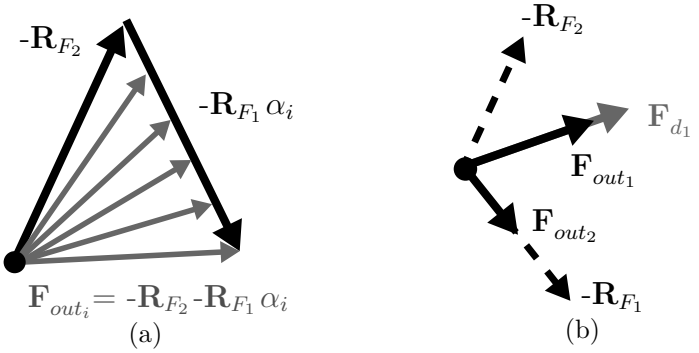

Figure 2.5: (a) The force range generated using a controlled and an uncontrolled actuators. (b) The force generated due to $\mathbf{F}_{in_1}$ and $\mathbf{F}_{in_2}$

regions in an n-DOF device.

2.2.2 Displayability Regions in an n-DOF Device

Let us examine the cases where all actuators are moving. The summation in (2.10) with a n-DOF device will involve n terms; one term for each actuator. The following three cases can be inferred:

- If the summation has no zero terms, the desired force is fully displayable.
- If at least one term of the summation is zero, the force is partially displayable
- If all terms are zero the forces are non-displayable.

Clearly, each combination of zero and non-zero terms corresponds to one displayability region. Considering all these 2^i combinations, one can find the number of regions in a device with i actuators. Moreover, the number of regions where k actuators can produce force is

$$\#\text{ of regions} = \frac{i!}{(i-k)!\,k!} \tag{2.11}$$

where $k = 0, 1, 2, \cdots, i$. The result for devices with-DOF between 1 and 6 is summarized in Table 2.1.

Irrespective of the number of DOF, a passive haptic device always has 1 fully dis-

playable ($k = i$) and 1 non-displayable region ($k = 0$); the remaining regions are partially displayable. These regions, however, differ from each other in the number of actuators they can use to partially display a force. Let us refer to this number as the *degree-of-displayability* (DOD), where DOD= k. In a 1-DOD region a force may be partially displayed using only one actuator, in a 2-DOD, two actuators, etc. So far, one has not seen regions with DOD greater than one. To understand the importance of these regions, let us examine a 3-DOF device which, according Table 2.1, has two types of partially-displayable regions.

2.3 Analyzing a 3-DOF Passive Device

Fig. 2.6(a) shows a 3-DOF non-redundant device with revolute joints. Its reference force and velocity vectors are found using (2.4) and are also shown in the figure. In this pose, all joints are orthogonal to one another. As a result, both force and velocity reference vectors will have the same direction. Note, however, if joints are not orthogonal these reference vectors will not be collinear, as was the case in Section 2.1.

By using a single actuator, a force can be generated only along the reference direction. By controlling the magnitude of two reference vectors the resultant force vector forms an arc. Drawing the arcs for all combinations of the 3 reference forces forms a sphere with spherical triangles on the surface (see Fig. 2.6(b)). The surface area enclosed by these triangles represents the directions produced using all 3 reference vectors, similar

Table 2.1: Number of all regions in passive devices with various DOF.

DOF	Fully Disp.	Partly-Displayable with DOD = k					Non Disp.	Total Reg.
		$k=5$	$k=4$	$k=3$	$k=2$	$k=1$		
1	1	0	0	0	0	0	1	2
2	1	0	0	0	0	2	1	4
3	1	0	0	0	3	3	1	8
4	1	0	0	4	6	4	1	16
5	1	0	5	10	10	5	1	32
6	1	6	15	20	15	6	1	64

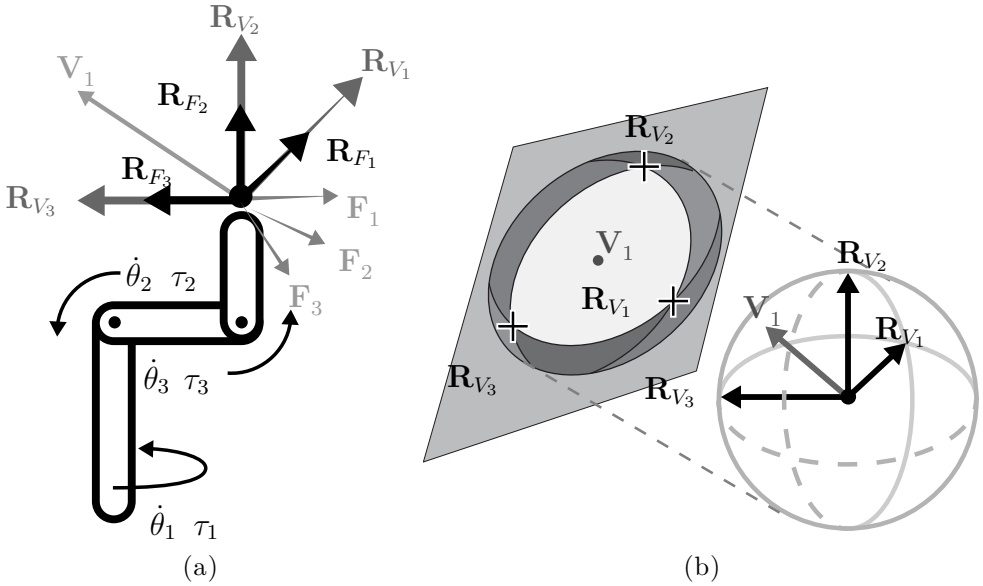

Figure 2.6: (a) Reference vectors for a 3-DOF device, along with forces and velocities acting on the device. (b) A sphere representing all vector directions, and its projection onto a plane. The signs of the reference vectors are used to specify their position.

to the regions found in a 2-DOF device.

For clarity, in Fig. 2.6(b), let us shade in the surface of each triangle and project the resulting sphere onto top and bottom planes. In this representation, a direction vector appears as a point on the surface of the sphere (notice $\mathbf{V}_1$). Using this representation, Fig. 2.7 shows the reference vectors, velocity, and forces acting on the manipulator in Fig. 2.6(a).

As predicted by (2.11) and Table 2.1, the device has a total of 8 regions: 1 displayable, 3 partly-displayable with 2 actuators (2-DOD), 3 partly-displayable with 1 actuator (1-DOD), and 1 non-displayable. These regions are the triangles on the projected spheres. The three displayable reference force vectors define the fully displayable region, while the non-displayable region is bounded by the reference velocity vectors. The remaining 6 regions are partially displayable.

The two types of partially displayable region can be seen in Fig. 2.7. Since arcs are formed by forces generated using 2 actuators, the regions sharing a side with the fully displayable region are partially displayable with the same two actuators.

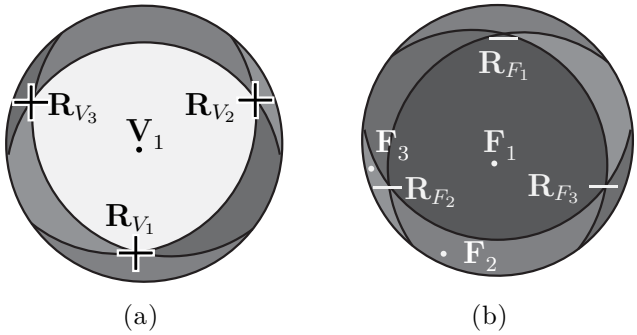

Figure 2.7: Projections of the sphere: (a) top showing the non displayable region (b) bottom showing fully displayable region

Consequently, the regions that share only a corner, that is a single reference vector, with the displayable region are partially displayable using only that one actuator. From this, one find that $\mathbf{F}_1$ is fully displayable, $\mathbf{F}_2$ can be partially displayed using a combination of -$\mathbf{R}_{F_2}$ and -$\mathbf{R}_{F_3}$, while $\mathbf{F}_3$ is partly-displayable using only -$\mathbf{R}_{F_2}$.

The displayable forces in regions with 1-DOD work in much the same way as the partly-displayable regions in a 2-DOF device described earlier. In these regions, the direction of the force is defined, and only the magnitude may be controlled. In the regions with 2-DOD, however, the direction of the force, along with its magnitude may be controlled using various combinations of the reference forces.

Lastly, moving from a 2-DOF to a 3-DOF device, there are significantly more directions that can be displayed using fewer than i actuators, i.e., there are 6 single actuator reference vectors, but there are also 12 regions where the force uses 2 actuators. Thus, a 3-DOF device may be more prone to stiction and to control the force output, the controller will rely more on the user's force input. From the control perspective, increasing the number of DOF has antagonistic effects on performance. On one hand, a larger portion of the workspace falls within partially displayable regions and the force approximation becomes more challenging.

2.4 Discussion

Based on the analysis of n-DOF devices in Section 2.2 one can compare devices with various DOF and gain insight into their feasibility. First, let us consider the relative size of the displayable region. This size varies widely depending on the configuration of the manipulator, therefore let us assume that all directions act orthogonal to one another, as was the case with the 3-DOF manipulator in Fig. 2.6(a). In this configuration, all regions are equal in size. The number and type of each region can be found through (2.11). For any DOF, the number of fully-displayable and the non-displayable regions is 1. Thus, the relative size η of each of these two regions is

$$\eta = \frac{\text{\# of displayable regions}}{\text{\# of regions}} = \frac{1}{2^i} \tag{2.12}$$

Two observations can be made right away. For one, the relative size of the fully displayable region decreases exponentially as the number of DOF increases. Secondly, the size of the non-displayable region decreases at the same rate. As a result, forces can be displayed in an increasingly limited range of directions but there are also fewer forces that cannot be displayed at all.

To put it into perspective, the fully-displayable and the non-displayable regions account for 25% of all direction in a 2-DOF device. In 3-DOF manipulators, this number is only 12.5%, and at 6-DOF it drops to 1.6%. Since there is a small range of forces that can be displayed accurately, and an equally small range of forces that cannot be displayed at all, the majority of the force range is partially displayable.

Table 2.1 shows that as the number of DOF increases, so do the DOD of these regions. Increasing the DOD is crucial in improving the displayability of a passive device. Thus, in a 1-DOD region, like in partly-displayable regions found in a 2-DOF device, only the magnitude of the force output can be controlled. In contrast, both the magnitude and direction of the force in a 2-DOD region is controllable.

A well-designed controller should be able to make use of this additional freedom to

improve the quality and/or accuracy of the forces produced by a passive device with many DOF. The controller could direct the user towards or away from regions with higher or lower DOD, respectively. Finally, with increasing DOF, the probability of one or more actuators in a device being stationary increases. As a result, a device with many DOF is likely to experience more stiction issues.

2.5 Conclusions

Passively-actuated haptic devices are an alternative to the conventional haptic displays that employ electric motors but their passivity makes them difficult to control. Several authors have highlighted issues with force control in passive devices. The majority of these analyses, however, have been limited to 2-DOF devices.

This chapter, introduces a new framework to analyze the performance of an n-DOF haptic device using brakes as actuators. First, it reviews the modelling techniques for a 2-DOF manipulator then expands and generalizes the analysis to examine the characteristics of an n-DOF device. The proposed formulation describes the quality of the force output generated in different regions of the workspace.

The analysis showed that as the number of DOF increases, the size of each region in the device decreases. In any non-redundant device, there is one fully and one non-displayable regions. As a result, the relative range of forces a device cannot produce decreases as the number of DOF increases. In fact, the range of forces in a haptic device with many DOF is mostly composed of partly-displayable regions.

An n-DOF device, additionally, contains many types of partly-displayable regions. These regions differ from each other in their degree-of-displayability (DOD), which represents the amount of control over a force produced in the partly-displayable regions. Higher DOD regions found in higher DOF devices offer better control over the force output. Using the partly-displayable forces and their full DOD, control algorithms may be able to greatly expand the range of a passive haptic device by approximating the desired force. In fact, using all the partly-displayable regions, the

relative force range of an n-DOF device should approach the range of an equivalent active device.

Further, the analysis highlighted that a stationary actuator limits the control over the force output of a device. The number of directions where one or more actuators is stationary increases with the number of DOF. As a result, a passive device with a high number of DOF will be more prone to stiction. However, [61, 64, 66] showed that the stiction may be, in part, mitigated by using clever control schemes. As a result, the feasibility of a device with n-DOF also depends on the controller's ability to alleviate problems caused by stiction and approximate a desired force.

Using partly-displayable forces produces an error in the reproduction of the force. For purposes of simulation, however, these forces do not have to be perfectly accurate. Humans have well-studied perception thresholds. For instance, according to [118], the sensory threshold of a human user is 7% for a differential change in force magnitude and, according to [119], 5° for change in direction. If the controller can maintain these differential errors within this range, a device with n-DOF will be feasible in many applications.

This chapter examined how the number of DOF affects the number of displayability regions of a passive device. The analysis did not take into account the shape and size of the displayability regions as these feature depends on the characteristics of the device; specifically their kinematic topology. Assessing the displayability characteristics of all passive devices is impossible as there are infinite possible kinematic configurations. By restricting the analysis to a small subset of devices, however, it may be possible to identify defining characteristics and differences between the structures. To this end, the next chapter compares the force displayability characteristics of planar passive devices with differing topologies.

Chapter 3

Impact of the Kinematic Structure on Passive Haptic Devices:

Comparison of Force Displayability in Planar Serial and Parallel Passive Devices

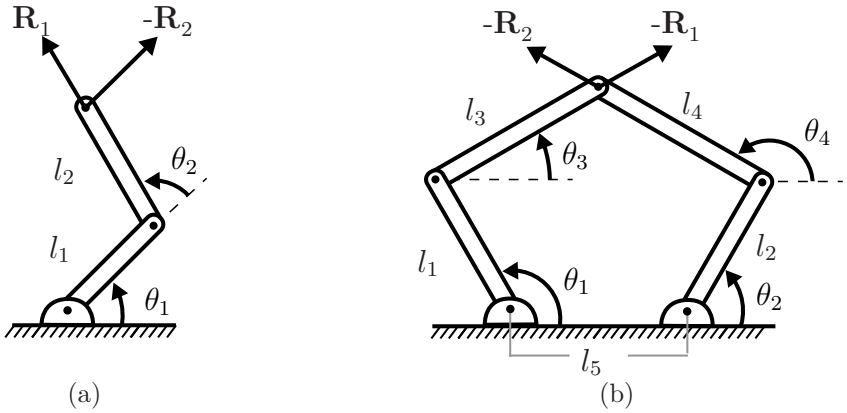

Figure 3.1: Two types of manipulators: a serial RR shown in (a) and parallel five-bar mechanism shown in (b), showing the reference force directions $\mathbf{R}_1$ and $\mathbf{R}_2$.

PLANAR manipulators have only two non-redundant topological variations: serial and parallel [37]. Serial manipulators, see Fig. 3.1(a), are composed of an open chain of actuated links. These manipulators have a larger workspace than their parallel counterparts with similar link lengths. Parallel manipulators, see Fig. 3.1(b), are formed by connecting two or more serial chains to a common end-effector. Distributing the load onto multiple links minimizes the relative motion of each actuator, resulting in lower apparent inertia of the device [37, 120], increased rigidity, and higher precision than in similar serial manipulators [120].

There are many tools available for the examining performance of conventionally actuated manipulator. Condition number, used in [121], and global workspace condition number, proposed in [122], evaluate the accuracy of velocity and force output of a manipulator throughout its workspace. In [123] a unified framework for a holistic analysis of a manipulator, which is simultaneous analysis of acceleration, velocity, and force output capability, was developed using dynamic capability equations. Generalized manipulability ellipsoids, introduced in [124] and adapted for parallel manipulators in [125], aid in visualizing and quantifying the ability of a manipulator to generate force in any direction. The ellipsoids were also used in [126] to determine the optimal pose for a redundant manipulator. The concept of ellipsoids was adopted for passive devices in [96], where passive manipulability ellipsoids were used to optimize a kinematically redundant planar 2-degree-of-freedom (DOF) parallel passive device.

The accuracy and the dynamic performance of serial and parallel manipulators was compared in [120] and [127], respectively. One unexplored issue is the impact of the kinematic structure on the force output capability of a passive device. This chapter address this issue by introducing a set of metrics measuring the output force capability of a generic passive haptic device. The novel metrics attempt to isolate the effects of actuator passivity by considering the percentage of the workspace where a desired force can be generated provided a velocity direction. These metrics, complement the metrics for active devices, such as [121–125] and unlike metrics proposed in [96], they provide a global overview of the performance changes due to change in velocity or desired force output directions. The metrics are evaluated on a subset of planar serial and parallel manipulators to demonstrate the impact of the kinematic structure on force displayability. The significant differences and trade-offs are highlighted, to aid in the choice between serial and parallel structures for the design of a passive device.

To this end, a set of new performance metrics is derived in Section 3.1 and then used to evaluate 9 manipulators in Section 3.2. The results are then used to compare the performance of the manipulators in Section 3.3, and conclude with a set of guidelines and recommendations for designing a 2-DOF passive haptic device in Section 3.4.

3.1 Performance Metrics for Passive Haptic Devices

To better understand the impact of the kinematic structure on force output capability of a passive haptic device one must isolate the effects of actuator passivity from the dynamics of the device. To this end, let us consider the area of the workspace where a given force can be either fully or partially displayed as a performance metric.

The total workspace of a device A_t can be divided into 3 regions: A_d, A_p, and A_n, where subscript d, p and n correspond to fully, partially, and non-displayable regions, respectively, see Fig. 3.2. The displayability of the force at each point depends on directions of velocity and desired force. As shown in Fig. 3.3(a), the directions of the

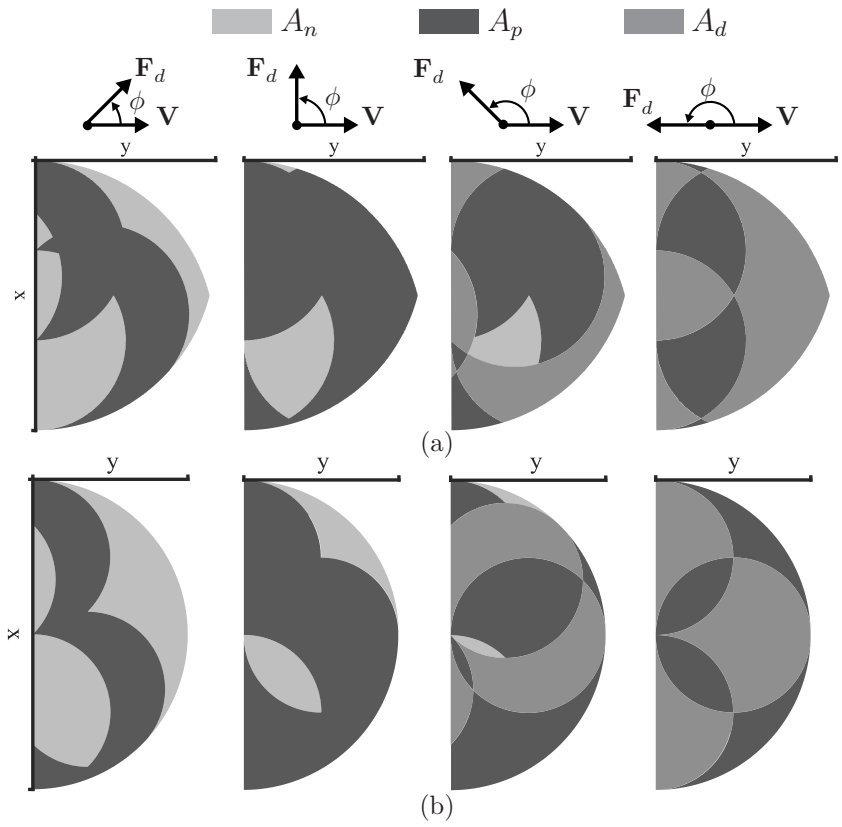

Figure 3.2: The fully, partially, and non-displayable regions in workspace of parallel (a) and serial (b) passive devices for $\phi = \pi/4, \pi/2, 3\pi/4, \pi$, and $\alpha = \pi/2$. The parallel manipulator in (a) has link lengths $l_1 = l_2 = l_3 = l_4 = l_5 = 1$, and the serial manipulator in (b) has $l_1 = l_2 = 1$.

velocity are defined as an angle $\boldsymbol{\alpha}$ which for planar devices has one component, the angle from positive x axis, and for spatial devices two components, along x and y axes. The direction of the desired force is defined as an angle $\boldsymbol{\phi}$ separating velocity and the desired force along the same axes as $\boldsymbol{\alpha}$. Ideally, the device must be able to generate a force in any direction, for any velocity, everywhere in its workspace. A passive device, however, can only generate the desired force in some parts of its workspace.

The total workspace area of a device can be found by integrating all of the points in the workspace. Since the geometry of the workspace reassembles a circle, the total workspace area is found with a polar integral such that,

$$A = \int_0^{2\pi} \int_0^{\pi} \int_0^1 r \, dr \, d\theta \, d\sigma \tag{3.1}$$

where $r = ||\mathbf{P}(r, \theta, \sigma)||$ is a point within the device's workspace, θ, σ, and r are the polar coordinates. The area of the region where a force can be fully displayed or approximated is found by integrating only the points located in a given displayability region. Currently, there is no analytical formulation to describe fully or partially displayable points. As a result, the area of these regions is approximated by,

$$A \simeq \sum_{j=1}^{n} \sum_{k=1}^{m} \sum_{l=1}^{p} ||\mathbf{P}(r_l, \theta_k, \sigma_k)|| \, \Delta r \, \Delta\theta \, \Delta\sigma \tag{3.2}$$

where $\mathbf{P}(r_l, \theta_k, \sigma_j)$ represents a point in the workspace satisfying the desired constraint.

To compare multiple types of manipulators with differing workspaces the area of each region must be normalized

$$\boldsymbol{\mu} = \frac{\mathbf{A}}{A_t} \tag{3.3}$$

where $\mathbf{A} = [A_d, A_p, A_n]$, with $A_t = A_d + A_p + A_n$, and the corresponding area fractions are $\boldsymbol{\mu} = [\mu_d, \mu_p, \mu_n]$. These metrics quantify the ability of a device to generate an arbitrary force for a specific input velocity direction. If the manipulator can display

the desired force in all of its workspace, $\mu_d = 1$. On the other hand, $\mu_p = 1$ represents a situation where all the forces in the workspace of the device can be partially displayed. Note that $\boldsymbol{\mu}$ depends on angles $\boldsymbol{\alpha}$ and $\boldsymbol{\phi}$. Assuming $\boldsymbol{\alpha}$ is constant, one can observe the change in the displayability through the workspace of the device, as a function of the angle between velocity and the desired force along one of the components $\boldsymbol{\alpha}_a$, represented by ϕ_a, as shown in Fig. 3.2. Let the mean value of $\boldsymbol{\mu}$ of the three types of regions for all values of ϕ_a be

$$\boldsymbol{\eta}_a = \frac{1}{2\pi} \sum_{0}^{2\pi} \boldsymbol{\mu} \; \Delta\phi_a \tag{3.4}$$

where $\boldsymbol{\eta}_a = [\eta_d, \eta_p, \eta_n]$. This measure represents the ability of a device to generate any force for an arbitrary velocity. If $\eta_d = 1$, the device can generate all desired forces in all directions for the specified value of α_a. Extending this measure of displayability to all possible values of α_a yields:

$$\bar{\boldsymbol{\eta}}_a = \frac{1}{2\pi} \sum_{0}^{2\pi} \boldsymbol{\eta} \; \Delta\alpha_a \tag{3.5}$$

where $\bar{\boldsymbol{\eta}}_a = [\bar{\eta}_d, \bar{\eta}_p, \bar{\eta}_n]$. These metrics measure the relative percentage of the forces a haptic device can generate for all possible combinations of velocity and desired force. If $\bar{\eta}_d = 1$, the manipulator can display a desired force in any direction. These metrics can highlight the trade-offs and characteristics of each topology, thus, aiding in the design of a passive device. This chapter analyzes only planar robots, thus, $\boldsymbol{\alpha} = \alpha_a = \alpha$, $\boldsymbol{\phi} = \phi_a = \phi$, $\eta_a = \eta$ and $\bar{\eta}_a = \bar{\eta}$.

3.2 Evaluating Passive Haptic Devices

The performance of serial and parallel manipulators are evaluated using metrics in (3.3), (3.4), and (3.5). To determine force displayability of the manipulators the Jacobian matrix is required. For a serial manipulator the Jacobian is [128]

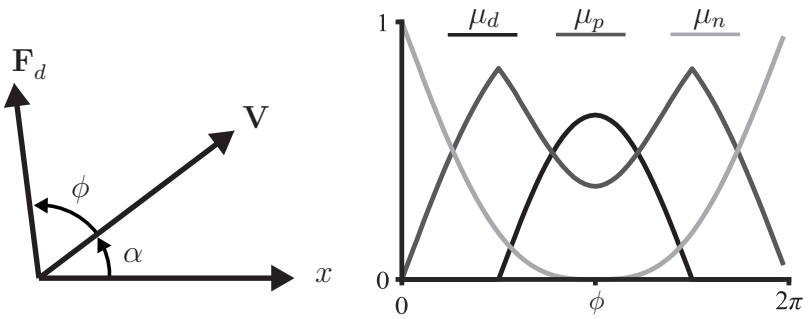

Figure 3.3: The ability of a device to generate a desired force depends on the angle α and ϕ, shown in (a). The performance of serial manipulators, shown in (b), was the same for $R = 0.5, 1$, and 2, and did not vary with α.

$$\mathbf{J} = \begin{bmatrix} -l_2 \sin(\theta_1 + \theta_2) - l_1 \sin\theta_1 & -l_2 \sin(\theta_1 + \theta_2) \\ l_2 \cos(\theta_1 + \theta_2) + l_1 \cos\theta_1 & l_2 \cos(\theta_1 + \theta_2) \end{bmatrix} \tag{3.6}$$

and for the parallel manipulator [129],

$$\mathbf{J} = \frac{1}{\sin(\theta_3 - \theta_4)} \begin{bmatrix} l_1 \sin(\theta_1 - \theta_3) \sin(\theta_4) & l_2 \sin(\theta_4 - \theta_2) \sin(\theta_3) \\ -l_1 \sin(\theta_1 - \theta_3) \cos(\theta_4) & -l_2 \sin(\theta_4 - \theta_2) \cos(\theta_3) \end{bmatrix}. \tag{3.7}$$

To reduce the number of possible kinematic solutions and singularities in the workspace of the two manipulators, both manipulators were constrained to half of the reachable workspace. The analysis also assumed all parallel manipulators to be symmetric i.e., $l_1 = l_2$ and $l_3 = l_4$, with $l_5 = 0$ or 1. Link lengths of the two manipulators are normalized and only the link length ratio, $R = l_1/l_3 = l_2/l_4$ for parallel and $R = l_1/l_2$ for serial manipulators, varies. There are 3 general cases to consider for each manipulator $R = 0.5, 1, 2$. In total, 9 manipulator configurations, listed in Table 3.1 were considered.

Their performance is aggregated and summarized in Table 3.1, while the detailed results are divided into three sets. Fig. 3.3(b) shows the performance measures for all serial manipulators. The results for parallel manipulators are grouped by length of l_5. Fig. 3.4(a) and (b) shows the performance results of parallel manipulators with $l_5 = 0$. For manipulators with $l_5 = 1$, on the other hand, the performance is shown in Fig. 3.4(c) and (d) as well as, Fig. 3.6 and Fig. 3.5.

Table 3.1: The 9 configurations of serial and parallel manipulators, with their link lengths, link length ratio R, and the corresponding performance as a percentage of the workspace.

Type	R	l_1	l_2	μ_{d-max}	μ_{p-max}	$\bar{\eta}_d$	$\bar{\eta}_p$	$\bar{\eta}_n$
Serial	0.5	0.5	1	63.9	81.6	17.9	50.0	32.1
	1	1	1	63.9	81.6	17.9	50.0	32.1
	2	1	0.5	63.9	81.6	17.9	50.0	32.1
Parallel $l_5 = 0$	0.5	0.5	1	54.7	77.3	17.9	50.0	32.1
	1	1	1	63.9	81.6	17.9	50.0	32.1
	2	1	0.5	50.3	75.1	18.1	50.0	31.9
Parallel $l_5 = 1$	0.5	0.5	1	90.5	98.4	22.6	50.0	27.4
	1	1	1	62.9	92.2	18.2	50.0	31.8
	2	1	0.5	97.0	98.5	15.1	50.0	34.9

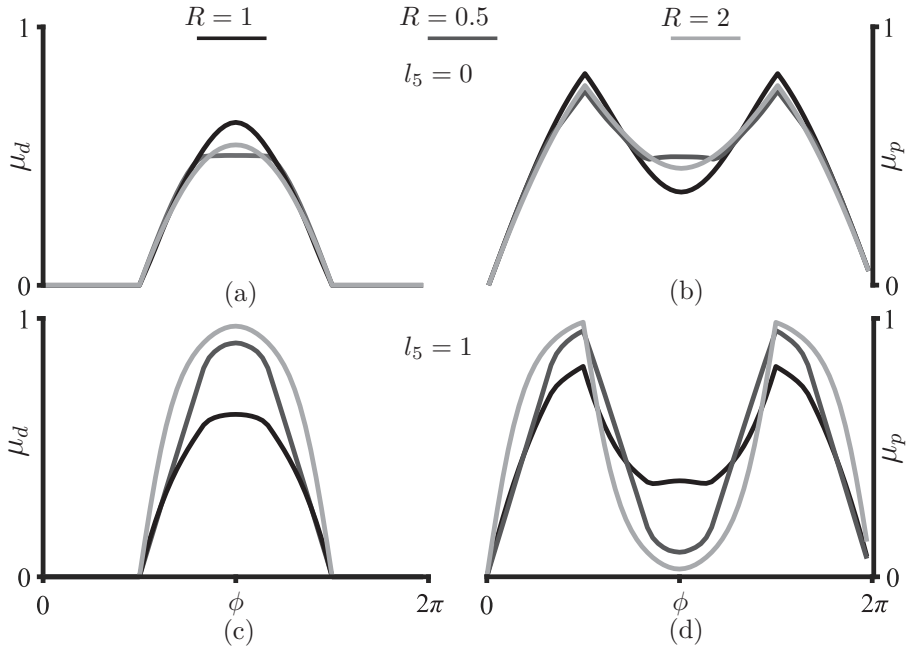

Figure 3.4: Performance of the two types of parallel manipulators. Performance, μ_d and μ_p, of devices with $l_5 = 0$ for any α is shown (a) and (b), respectively. The performance of device with $l_5 = 1$, at $\alpha = \pi/2$ is shown in (c), and (d).

3.3 Discussion

There are clear distinctions in performance across the spectrum of manipulators. All serial manipulators performed the same, irrespective of their link length ratio R or direction of velocity α. The performance of parallel manipulators varied significantly as a function of both R and l_5. As a result, the performance of parallel manipulators will be analyzed separately for manipulators with $l_5 = 0$ and $l_5 = 1$.

3.3.1 Serial Manipulators

The results for all serial manipulators, independent of the link length ratio or the direction of velocity were the same as shown in Table 3.1. Let $\mu_{d-max} = \max(\mu_d)\ \forall\phi,\ \forall\alpha$ represent the highest percentage of the fully displayable region μ_d. For a serial manipulator, this angle occurs when the angle between the velocity and the desired force is $\phi = \pi$, as shown in Fig. 3.3(b). Note that since $\mu_{d-max} < 1$, there are parts of the workspace where a force directly opposing the velocity cannot be rendered. When $\phi = \pi$, $\mu_d = 0.63$ and $\mu_p = 0.37$, which means that desired force can be generated in 63% of the device's workspace while in the remaining 37% the force can be approximated. Since $\bar{\eta}_d = \eta_d = 0.179$ and $\bar{\eta}_p = \eta_p = 0.5$, the performance of these manipulators does not vary with α. Consequently, for all combinations of α, the mean percentage of the fully and partially displayable regions in the workspace was 17.9% and 50.0% respectively. All serial manipulators, therefore, can fully or partially display 67.9% of all forces irrespective of the velocity direction.

3.3.2 Parallel Manipulators with $l_5 = 0$

Like serial manipulators, the performance of parallel manipulators with base link length $l_5 = 0$ is insensitive to change in α, meaning that $\bar{\eta}_d = \eta_d$ and $\bar{\eta}_p = \eta_p$. Unlike serial manipulators, the performance varies depending on the link length ratio R, which is optimal when $R = 1$. Their optimal values are exactly the same as all serial manipulators, as shown in Fig. 3.4 (a) and (b).

Any link ratio other than $R = 1$ deteriorates μ_d, μ_p, η_d, and η_p. As shown in Table 3.1 and Fig. 3.4(a) and (b), the manipulator with $R = 2$ has the lowest maximum μ_d and μ_p, and the lowest $\bar{\eta}_p$, meaning it could generate a smaller range of forces than the manipulators with $R = 1$ or 0.5. From Fig. 3.4(a) and (b), the manipulator with $R = 1$ performed slightly better than manipulator with $R = 0.5$. This change is reflected in the maximum value of μ_d listed in Table 3.1. However, the difference in η and $\bar{\eta}$ of the two manipulators is insignificant given the working precision. Thus, the link lengths of this manipulator must be equal to maximize performance, and there is no advantage to varying the link length from the perspective of a passive haptic device.

3.3.3 Parallel Manipulators with $l_5 = 1$

The performance of parallel manipulators with $l_5 = 1$ varies as a function of α and ϕ. To start, consider μ_d and μ_p of the device for $\alpha = \pi/2$, shown in Fig. 3.4 (c) and (d), respectively. This manipulator is much more sensitive to changes in link ratio R. The maximum fraction of the partially displayable region μ_d for the 3 manipulators varies from 0.639 to 0.97. For some velocity directions, these manipulators can create a force that opposes velocity anywhere in the workspace. The results change significantly depending on the angle α. From Fig. 3.6(a), the maximum value of μ_d for all angles of ϕ is shown as a function of α. Notice that at both $\alpha = 0$ and $\alpha = \pi/2$, the maximum μ_d are the same, for each of the three manipulators. This shows that at $\alpha = 0, \pi/2, \pi$, and $3\pi/2$, the manipulator with $R = 2$ can generate a force at any point in its workspace. The peak value of μ_d for this manipulator, however, experiences the steepest drops, as shown in Fig. 3.6(a).

Let us focus on Fig. 3.6(b), which shows the variation of average fraction of the displayable region μ_d that is η_d, for the three manipulators as a function of α. Notice that, compared with Fig. 3.6(a), peaks of μ_d and η_d do not align. To investigate the discrepancy, let us examine Fig. 3.5, where μ_d and μ_p are shown for the three manipulators, at $\alpha = 0, \pi/4$, and $\pi/2$. Fig. 3.5(a) (c) and (e), all show that for $\alpha = 0$

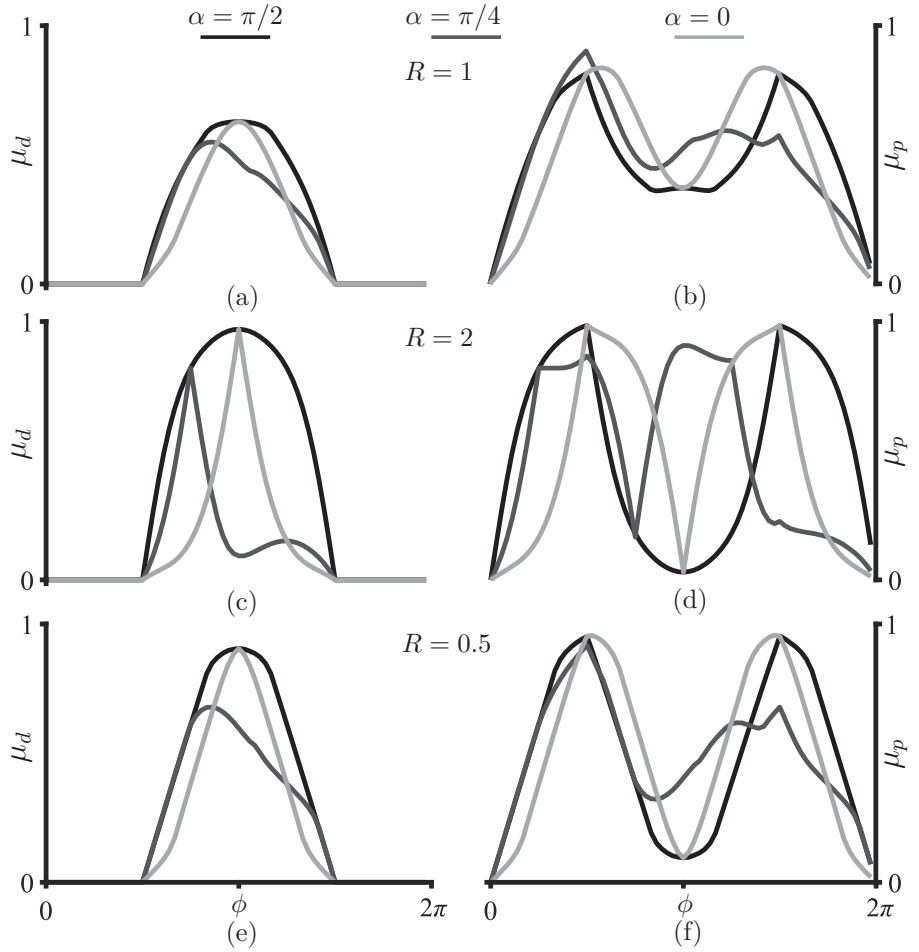

Figure 3.5: Performance of parallel manipulators with $l_5 = 1$ for $\alpha = 0, \pi/4, \pi/2$. For manipulators with $R = 1$, the results are in (a) and (b), for $R = 2$ in (c) and (d), and for $R = 0.5$ in (e) and (f).

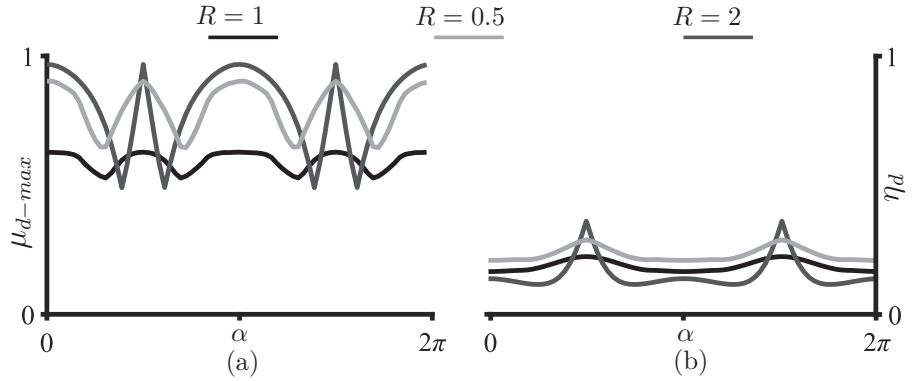

Figure 3.6: The performance for parallel manipulators with $l_5 = 1$. In (a), the variation of the maximum μ_d is shown as a function of α. The variation in η_d, on the other hand, is shown in (b).

and $\alpha = \pi/2$, the performance has the same peak μ_d. As the curves of μ_d and μ_p illustrate at $\alpha = \pi/2$ all 3 of the manipulators can render more forces than at $\alpha = 0$ in directions other than $\phi = \pi/2$. The peaks in Fig. 3.6(a) that do not correspond with peaks in (b), represent directions where force at a specific direction, can be generated almost anywhere in the workspace, but all other forces will be difficult to render.

Lastly, consider the variation in performance of the 3 manipulators, shown in Fig. 3.6. The performance, μ_{d-max} and η_d, clearly varies the least in the manipulator with $R = 1$. The manipulator with $R = 2$, on the other hand, has the highest peak performances, but also steepest declines. The performance of the manipulator with $R = 0.5$ is almost as high as for the manipulator with $R = 2$, but it does not have as steep of declines i.e, $\partial\eta_d/\partial\alpha$. As a result, this manipulator performs the best, as indicated by a high value of $\bar{\eta}_d$ listed in Table 3.1. Notice that all parallel manipulators with both manipulators with $R = 1$ and 0.5, had the highest value of $\bar{\eta}_d$ of all manipulators.

3.4 Conclusions

This chapter presents the first analysis of the effects of the kinematic structure on the ability of a passive haptic device to generate forces. The performance metrics introduced here evaluate the areas of the device's workspace where the desired force can be either fully displayed, or partially displayed.

The analysis considers 9 manipulators, 3 serial and 6 parallel kinematic chains, with link length ratios of 0.5, 1, and 2. The following recommendations can be made for 2-DOF RR serial and symmetric 2-DOF five-bar parallel manipulators from the findings of this chapter:

- Passive serial manipulators generate forces in all directions equally well independent of the link length ratio;
- Parallel manipulators with a base link length of zero generate the widest range of forces in their workspace when all links have the same length;

- Parallel manipulators with a base link length equal to one perform better in a larger percentile of the workspace than serial manipulators;

This performance, however, varies significantly depending on the direction of the velocity. Parallel manipulators perform best when the velocity acts perpendicular to the base of the manipulator, and worst when the velocity acts at an angle of $\pi/4$ from the base link. In this category of manipulators, the one with link length ratio of 0.5, performs the best.

Serial manipulators perform equally well for all combinations of link length ratios, so no optimal configuration of this manipulator exists in terms of force displayability. For parallel manipulators there exists no global optimum solution; force displayability can only be improved for certain velocity directions. Thus, optimization of a parallel manipulator should be conducted on a case-by-case basis. During the design, the metrics presented here should be used in conjunction with other dexterity metrics to develop a fitness equation tailored to the application. These results aid in the design of 2-DOF passive haptic devices. Serial and parallel manipulators with $l_5 = 0$ are equally suitable for applications where the user is expected to move in all directions equally i.e., the most general use case. For specialized applications where the motion has a predominant direction, parallel manipulators with $l_5 > 0$ are a better choice. These applications include simulation of needle insertion tasks [130], teleoperation of robots in constrained workspaces, or upper limb patient rehabilitation [69].

The metrics proposed in this chapter should be used in conjunction with other metrics, like manipulability [124, 125], dynamic capability equations [123] and workspace condition number [121, 122], to design a passive haptic device with the desired force output capability and dynamic characteristics.

Assuming that the findings for 2-DOF manipulators are at least partially applicable to 3-DOF manipulators, a passive device intended for minimally invasive surgery, where the motion of the tool is constrained to a defined path, could make excellent use of parallel kinematic structure with base link distance greater than zero. The next chapter presents a new 3-DOF passive device with parallel kinematic structure

with these exact properties. The device is controlled using a novel controller developed specifically for 3-DOF passive haptic devices. It takes advantage of the two types of partially displayable regions, discussed in Chapter 2, to expand the range of displayable forces and eliminate stiction.

Chapter 4

A 3-DOF Passive Haptic Device

The Design and Control of a Novel Haptic Device with Parallel Kinematic Structure

ANY haptic device intended for surgical applications must move in in at least three translational DOF [131, 132]. A passive device with 3-DOF, however, will have a relatively small fully displayable region, as it will also contain contains two types of partially displayable regions to approximate forces. The main challenge in the development of a higher DOF passive device is, therefore, the design of a controller capable of using all partially displayable regions. This chapter presents the design of a 3-DOF parallel passive device and a new controller that approximates forces in the partially displayable regions using all available brakes.

To date, there has only been one documented example of a passive haptic device with 3-DOF translational motion. This device was developed for dental implant surgery simulation and used a 5-bar regional kinematic structure, like the one in PHANToM devices [99]. The kinematic structure minimized the effects of gravity on the device but also introduced inertia [133], reducing transparency. As discussed in the previous chapter, devices with parallel kinematic structure have low inertia, high rigidity, and higher preferable force displayability characteristics in certain virtual environments. For this reason, the proposed 3-DOF device uses a parallel kinematic structure, making it the first passive parallel 3-DOF device.

The detailed design breakdown of the novel passive device is presented in Section 4.1. Next, Section 4.2 models the force output of the device and uses it to develop a novel controller in Section 4.3. This controller aims to alleviate the issues caused by brakes namely stiction and the uncontrollable direction of the force output. The performance of the controller is then tested in Section 4.4 and discussed in the context of surgical applications in Section 4.5. Finally, Section 4.6 reviews the results and determine whether the device and the controller are suitable for surgical applications. To begin, let us start with the design of the 3-DOF passive haptic device.

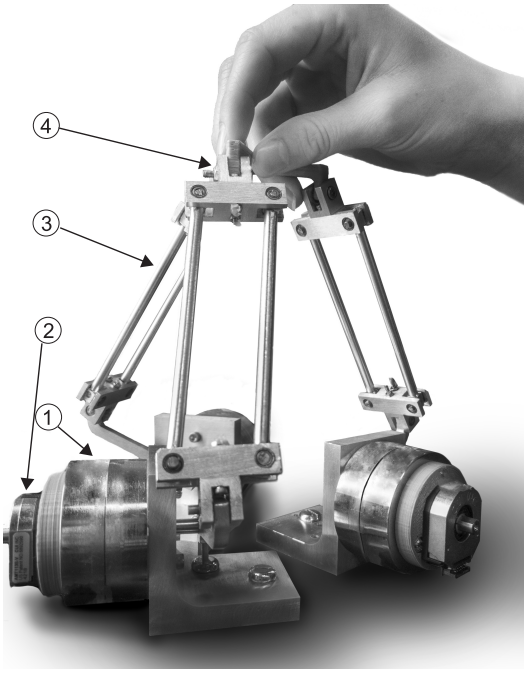

Figure 4.1: The assembled device consists of 3 identical legs (3) attached to the end-effector (4). Each leg is actuated by a brake (1), and its angular position is measured using an encoder (2).

4.1 3-DOF Parallel Passive Haptic Device

The 3-DOF device, shown in Fig. 4.1, uses a variation of the parallel kinematic structure known as the *Delta* configuration. This kinematic structure was chosen due its high rigidity, transparency, and lack of spherical joints, commonly found in other parallel manipulators. The device has only translational DOF, meaning that the end-effector remains parallel to the base at all times. By employing parallel kinematics the heavy brakes are fixed at the bottom platform reducing the mass of the moving parts, minimizing the apparent inertia of the device. Furthermore, the links of the device were custom made from aluminium, keeping the device light and rigid and each joint included a pair of bearings minimizing the joint friction.

The device is actuated by three Placid Industries B-2 magnetic particle brakes. The choice of these brakes was dictated by their wide torque range spanning from $8.5\,\mathrm{mN \cdot m}$ (off-state torque) to $280\,\mathrm{mN \cdot m}$ resulting in a max-to-min torque ratio of 32.9. The angular position of each brake is measured using an incremental encoder with a res-

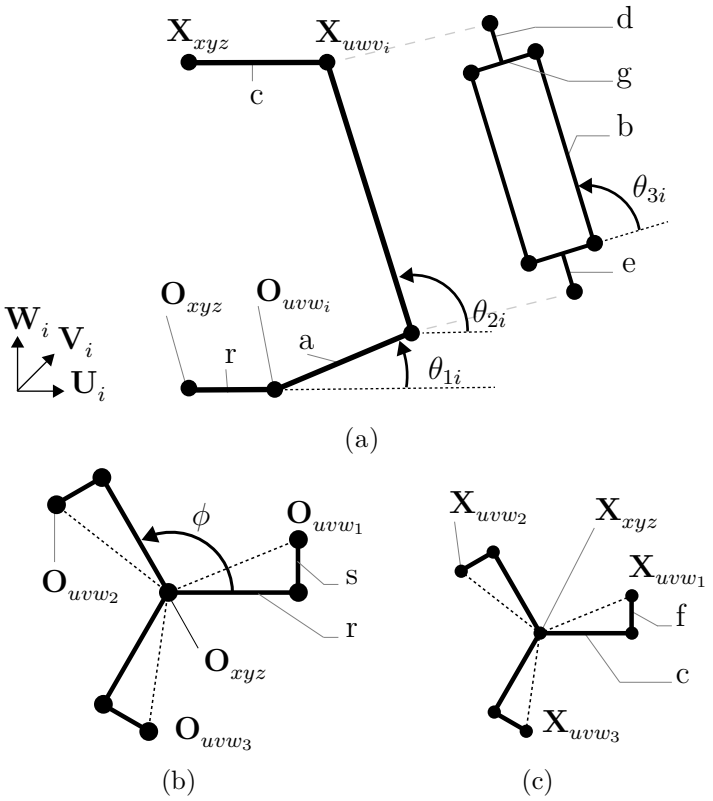

Figure 4.2: Fig (a) shows the schematic of the i^{th} leg in the u_i, v_i, w_i reference frame. The leg attaches to the base at $\mathbf{O}_{uvw_i}$, shown in (b), and to the top platform at $\mathbf{X}_{uvw_i}$, shown in (c)

olution of 2048 pulses-per-revolution (AMT112Q from CUI Inc.). Using the encoder data, the position of the device can be determined within 1.5 mm accuracy. The device generates a peak force of approximately 10 N satisfying the requirements for laparoscopic procedures [134]. Note, however, that for applications requiring higher force output other, stronger brakes can be used. To the best of our knowledge the modified Delta kinematic structure has never been used with passive actuators for haptic applications. The kinematic structure of the device includes 3 legs shown in Fig. 4.2(a), as well as top and bottom platforms, in Fig. 4.2(c) and Fig. 4.2(b) respectively. The link lengths of the device were chosen based on previously established designs, namely the Novint Falcon, and they are listed in Table 4.1. Using these link lengths, it is possible to solve the inverse kinematics of the device.

Table 4.1: Links (top row) of the haptic device and their corresponding lengths in millimeters (bottom row).

Link Lengths in millimeters								
a	b	c	d	e	f	g	r	s
60.0	102.5	14.4	13.0	13.0	25.0	27.9	36.6	27.2

4.1.1 Inverse Kinematics

In an inverse kinematics problem the joint angles of the device are calculated for a specified position of the end-effector $\mathbf{X}_{xyz}$ in the xyz fixed coordinate frame. To solve this problem it is convenient to independently consider each of the three legs composing the device. In Fig. 4.2(a), leg i has three defining angles, $\boldsymbol{\theta}_{1i}$, $\boldsymbol{\theta}_{2i}$, $\boldsymbol{\theta}_{3i}$. Each leg in the system is independent of the others, therefore, one can solve for the angle in each leg independent of any other leg. Let uvw_i represent the new reference frame for leg i defined such that u acts along the rotation axis of the brake at an angle ϕ_i from the original reference frame, like in Fig. 4.2(a). The position of the attachment point for each leg in the uvw_i reference frame, $\mathbf{X}_{uvw_i} = [U_i \quad V_i \quad W_i]$, is given by,

$$\begin{bmatrix} U_i \\ V_i \\ W_i \end{bmatrix} = \begin{bmatrix} \cos\phi_i & \sin\phi_i & 0 \\ -\sin\phi_i & \cos\phi_i & 0 \\ 0 & 0 & 1 \end{bmatrix} \begin{bmatrix} X_x \\ X_y \\ X_z \end{bmatrix} + \begin{bmatrix} -r \\ -s \\ 0 \end{bmatrix} \tag{4.1}$$

where $\phi_i = [0 \quad 2\pi/3 \quad 4\pi/3]$ corresponds to the angle between the base frame and link a of leg i [135–137].

In the new reference frame the end-effector position is:

$$U_i = a\,\cos\theta_{1i} - c + \cos\theta_{2i}\,(d + e + b\,\sin\theta_{3i}) \tag{4.2a}$$
$$V_i = b\,\cos\theta_{3i} \tag{4.2b}$$
$$W_i = a\,\sin\theta_{1i} + \sin\theta_{2i}\,(d + e + b\,\sin\theta_{3i}). \tag{4.2c}$$

Solving (4.2b) gives,

$$\theta_{3i} = \arccos\left(\frac{V_i}{b}\right). \tag{4.3}$$

Note that a positive and a negative solution to (4.3) exists but due to the physical constraints of the manipulator links, only the positive solution is possible [136, 137]. Similarly, only the positive solution is valid for θ_{1i}, found using

$$\theta_{1i} = \arcsin\left(\frac{2\,t_i}{1+t_i^2}\right) \tag{4.4}$$

with

$$t_i = \frac{-l_i - \sqrt{l_i^2 - 4\,l_{2i}\,l_{0i}}}{2\,l_{2i}}$$

where $t_i \in \mathbb{R}$, and

$$\begin{aligned}
l_{0i} =& W_i^2 + U_i^2 + 2cU_i - 2aU_i + a^2 + c^2 - d^2 - e^2 \\
& - b^2\sin^2\theta_{3i} - 2be\sin\theta_{3i} - 2bd\sin\theta_{3i} - 2de - 2ac \\
l_{1i} =& -4aW_i \\
l_{2i} =& W_i^2 + U_i^2 + 2cU_i + 2aU_i + a^2 + c^2 - d^2 - e^2 \\
& - b^2\sin^2\theta_{3i} - 2be\sin\theta_{3i} - 2bd\sin\theta_{3i} - 2de + 2ac.
\end{aligned}$$

Knowing θ_{1i} and θ_{3i}, the last angle, θ_{2i}, is

$$\theta_{2i} = \arccos\left(\frac{W_i - a\,\sin\theta_{1i} - \sin\theta_{2i}}{d + e + b\,\sin\theta_{3i}}\right). \tag{4.5}$$

With all three angles in the three legs of the device known, it is possible to find the Jacobian matrix for the device.

4.1.2 Jacobian Matrix

The Jacobian of the manipulator relates angular velocity of the joints $\dot{\boldsymbol{\theta}}$ to the velocity of the end-effector in Cartesian space $\dot{\mathbf{X}}$ such that,

$$\dot{\mathbf{X}} = \mathbf{J}\,\dot{\boldsymbol{\theta}}. \tag{4.6}$$

The Jacobian is obtained by taking a partial derivative of the loop equations $\partial(U_i, V_i, W_i)/\partial(\theta_{11}, \theta_{12}, \theta_{13})$, and solving for the joint rates $\dot{\theta}_{11}, \dot{\theta}_{12}, \dot{\theta}_{13}$ resulting in,

$$\mathbf{J} = \begin{bmatrix} J_{11} & J_{12} & J_{13} \\ J_{21} & J_{22} & J_{23} \\ J_{31} & J_{32} & J_{33} \end{bmatrix} \tag{4.7}$$

where each element of the Jacobian is [135, 136]:

$$\begin{aligned} J_{1i} &= \frac{\cos\theta_{3i}\,\sin\phi_i - \cos\phi_i\,\cos\theta_{2i}\,\sin\theta_{3i}}{a\,\sin\left(\theta_{1i} - \theta_{2i}\right)\,\sin\theta_{3i}} \\ J_{2i} &= -\frac{\cos\phi_i\,\cos\theta_{3i} + \cos\theta_{2i}\,\sin\phi_i\,\sin\theta_{3i}}{a\,\sin\left(\theta_{1i} - \theta_{2i}\right)\,\sin\theta_{3i}} \\ J_{3i} &= -\frac{\sin\theta_{2i}}{a\,\sin\left(\theta_{1i} - \theta_{2i}\right)}. \end{aligned}$$

4.1.3 Forward Kinematics

In contrast to the inverse kinematics, the forward kinematics of a parallel manipulator is significantly more difficult to compute as it involves solving a 32^{nd} order polynomial with a total of 32 solutions, of which 16 are extraneous [135, 136]. The high computational cost, the considerable difficulty of implementation, and the multitude of solutions make the analytical solution impractical to use. As a result, the forward kinematics of parallel manipulators is commonly approximated using iterative solvers like the damped Newton's method [113, 137].

Similar to other variants of iterative solvers, damped Newton's Method starts with an initial position guess and then iteratively improves the solution until the error is minimized. The method gives the position of the end-effector at iteration k

$$\mathbf{X}_k = \mathbf{X}_{k-1} - \mathbf{J}(\boldsymbol{\theta}_{k-1})^{\mathrm{T}}\left(\boldsymbol{\theta} - \boldsymbol{\theta}_{k-1}\right) G \tag{4.8}$$

where $\mathbf{X}_{k-1}$ is the estimated position taken at sample $k-1$ that is used to find the

joint angles $\boldsymbol{\theta}_{k-1}$ and the Jacobian matrix $\mathbf{J}(\theta_{k-1})^{\mathrm{T}}$. The actual angular position of θ_{1i} is represented by $\boldsymbol{\theta}$, and G is an adaptive scaling factor. The error between the estimated and actual position is $E(k) = ||\boldsymbol{\theta} - \boldsymbol{\theta}_{k-1}||$. If the error between iterations decreased, $E(k) < E(k-1)$, then the solution is accepted, $\mathbf{X}_{k+1} = \mathbf{X}_k$, and the loop is repeated. If, however, the error increased, $E(k) > E(k-1)$, the solution is rejected, $\mathbf{X}_k = \mathbf{X}_{k-1}$, and the scaling factor is decreased $G = G/2$. The loop ends after a set number of iterations, or when an acceptable answer is reached. In most cases, the solver converges onto a solution within 15 iterations [138].

Once all joint angles are calculated, the Jacobian matrix can be calculated using (4.7). Using the Jacobian it is also possible to convert forces into joint torques of the device. For a passive haptic device, however, the torque generated by the brakes depends on factors other than the desired torque.

4.2 Modelling the Force Output of a Passive Haptic Device

The kinematic structure of the device creates a non-linear relationship between the motion and forces at the end-effector and at the brakes. The description of the force output of a passive device is further complicated by the nonlinear force output capability of the device. As a result, the analysis of passive devices is typically conducted using reference forces.

4.2.1 Force Output of a Haptic Device

An ideal haptic device can create any force output. This can be represented as a sum of the scaled reference forces from (2.4),

$$\mathbf{F}_a = \sum_{i=1}^{n} a_i \, \mathbf{R}_i \tag{4.9}$$

where $a_i \in \mathbb{R}$ represents the scaling factors of the reference force i. In Fig. 4.3(a)

forces $+\mathbf{R}_1$ and $+\mathbf{R}_2$ can be generated. To generate $\mathbf{F}_1$, however, -$\mathbf{R}_1$ and $+\mathbf{R}_2$ must be used. By setting a_i to a negative value, the direction of the resulting force will equal -$\mathbf{R}_i$. On the other hand, to generate $+\mathbf{R}_i$, no sign change is necessary, meaning $a_i > 0$. Note that (2.3) and (4.9) are equivalent, thus making $a_i = \tau_i$.

For an ideal device, there always exists a set of a_i values that can make the output force $\mathbf{F}_a$ and the desired force $\mathbf{F}_d$ equal to each-other, $\mathbf{F}_a = \mathbf{F}_d$. For a realistic device, however, there is a limit to the torque an actuator can generate, thus, the scaling factor must be bound to $a_i \in \mathbb{R}[-\tau_{max_i} \quad \tau_{max_i}]$, where τ_{max_i} is the maximum torque output of the i^{th} actuator. This confines the force range of the device and leads to the limited manipulability shown as the region Ω_1 in Fig. 4.3(b). The contour of this region represents the manipulability of a device in a given direction. A realistic device, therefore, can create a finite force output in all directions but the magnitude of the maximum force in any of these directions can vary.

4.2.2 Force Output of a Passive Device

When a haptic device uses brakes as actuators, the force output is further constrained. Recall that when moving, a brake can only generate torque opposing the angular velocity of the respective joint, i.e. $\dot{\theta}_i \, \tau_i < 0$. As a result, one can control the magnitude of the force generated at the end-effector but not its direction. If the brake is stationary, however, neither the direction nor the magnitude of the torque can be controlled. Instead, the brake generates torque opposing any torque input τ_{in}, i.e. $\tau_{out} = -\tau_{in}$. Consider the case with two moving brakes in Fig. 4.3(a), where joint 1 rotates in the positive (CW) direction and joint 2 rotates in the negative (CCW) direction. As a result, the device can produce a negative torque at joint 1 and a positive torque at joint 2. At the end-effector the torque developed in joint 1 creates the reference force -$\mathbf{R}_1$, and the torque in joint 2 gives $+\mathbf{R}_2$.

To describe the force output of a passive device, (4.9) must be modified to account for these additional restrictions. The sign of the scaling factors is determined by the velocity or torque input to each brake. For a positive velocity, the brake can only

generate a negative torque, which results in a negative reference force, and vice-versa. If the velocity is zero the sign is determined by the force input to the device. The force output in such a case must oppose the force input, i.e. $\mathbf{F}_d \cdot \mathbf{F}_{in} < 0$. This condition must be evaluated for each actuator, which means that both the desired and the input forces must be projected onto the relevant reference force. If the product of the two projections is less than zero, i.e., $(\mathbf{R}_i \cdot \mathbf{F}_{in})(\mathbf{R}_i \cdot \mathbf{F}_d) < 0$, the forces oppose each other and the reference force can be used to display the force, otherwise the brake must be released. Thus, the sign of the scaling factor in a passive device is determined by

$$S(\dot{\theta}_i) = \begin{cases} -1 & \text{if } \dot{\theta} > 0 \\ H\left[-(\mathbf{F}_{in} \cdot \mathbf{F}_d)(\mathbf{R}_i \cdot \mathbf{F}_d)\right] \frac{\mathbf{F}_{in} \cdot \mathbf{R}_i}{||\mathbf{R}_i||^2 \, \alpha_i} & \text{if } \dot{\theta} = 0 \\ 1 & \text{if } \dot{\theta} < 0 \end{cases} \tag{4.10}$$

which yields either -1, the force applied by a stationary brake divided by α_i, or 1, and where $H()$ is the Heaviside step function which determines if a force is displayable[1].

Since the direction of the scaling factor is determined by (4.10), one must redefine the scaling factor such that its value is always positive. To differentiate between the active and passive devices, let us use $\alpha_i \in \mathbb{R}\,[0 \quad \tau_{max}]$ when referring to passive devices. Now, the range of forces a passive device can generate is given by

$$\mathbf{F}_a = \sum_{i=1}^{n} \alpha_i \, S(\dot{\theta}_i) \, \mathbf{R}_i. \tag{4.11}$$

Note, that in a static case α_i is eliminated from the equation.

Unlike in (4.9), the device can only generate a desired force provided that a solution to (4.11) exists such that $\mathbf{F}_a = \mathbf{F}_d$. As shown in Fig. 4.3(b), this greatly restricts the range of *displayable forces*, i.e., the forces such a device can generate. The force output of the passive device is bounded by Ω_2 where $\Omega_2 \subset \Omega_1$. Such a limited range of force makes it difficult to implement passive devices in most applications. The next section

[1]The force applied by a stationary brake is uncontrollable, therefore the term α_i needs to be eliminated in the formulation. Dividing the result of (4.10) by α_i is the simplest method of achieving this mathematically.

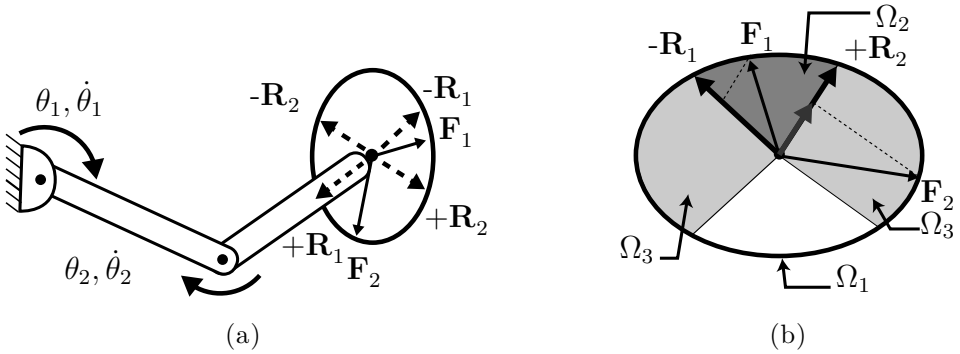

Figure 4.3: (a) A 2-DOF manipulator and its reference force vectors. (b) Regions formed by the reference forces of the device in (a), and the decomposition of the forces along the reference vectors.

describes a method of expanding this range by approximating the desired forces.

In Fig. 4.3, the force $\mathbf{F}_2$ cannot be displayed by the device since $+\mathbf{R}_1$ is required to replicate the force but only $-\mathbf{R}_1$ is available. It is still possible to use a component of $+\mathbf{R}_2$ to approximate $\mathbf{F}_2$. This is shown in Fig. 4.3(b) where $\mathbf{F}_2$ is projected onto $+\mathbf{R}_2$, as indicated by the dotted line. This projection represents the closest approximation of $\mathbf{F}_2$ that $+\mathbf{R}_2$ can generate alone. As long as this projection is greater than zero, the reference force may be used. In Fig. 4.3(b), the forces satisfying this condition are bounded by Ω_3, where $\Omega_3 \subset \Omega_1$. Notice that $\Omega_2 \subset \Omega_3$ which means that if a force can be reproduced based on (4.11) it can also be approximated. Thus, the best approximation of the desired force becomes:

$$\mathbf{F}_a = \sum_{i=1}^{n} \alpha_i \, D_i \, \mathbf{R}_i \tag{4.12}$$

where $\mathbf{F}_a \simeq \mathbf{F}_d$, and

$$D_i = S(\dot{\theta}_i) \, H \left(S(\dot{\theta}_i) \, \mathbf{R}_i \cdot \mathbf{F}_d \right). \tag{4.13}$$

It may be convenient to think of (4.12) as a matrix, such as,

$$\mathbf{F}_a = \begin{bmatrix} \mathbf{R}_1 & \mathbf{R}_2 & \cdots & \mathbf{R}_i \end{bmatrix} \, (\boldsymbol{\alpha} \circ \mathbf{D}) \tag{4.14}$$

where $\boldsymbol{\alpha} = [\alpha_1, \alpha_2, \cdots, \alpha_i]^{\mathrm{T}}$, $\mathbf{D} = [D_1, D_2, \cdots, D_i]^{\mathrm{T}}$, and the operator $\circ$ is the Hadamard product. If $\mathbf{F}_a$ has a full rank, the force can be displayed accurately. If the rank is not full but also not zero, the force output of the device may be approximated. If the rank is zero no forces can be displayed. Let us explore a method of approximating the desired force using 1, 2, or 3 reference forces.

4.3 Controller Design

The control approach chosen here forces the device to slide along a rigid frictionless surface. The sliding motion reduces brake stiction and force distortions induced by force approximation. The sliding is enforced by balancing the forces at the end-effector such that they are in an equilibrium along the direction normal to the surface.

Consider a virtual environment composed of a wall defined by an arbitrary surface, with some stiffness and no friction, like the one in Fig. 4.4(a). In an ideal case shown in Fig. 4.4(a) (1), the user applies force $\mathbf{F}_{in}$ to the device which, in turn, generates a force output $\mathbf{F}_a = \mathbf{F}_d$. The sum of these two forces result in a net force

$$\mathbf{N} = \mathbf{F}_a + \mathbf{F}_{in} \tag{4.15}$$

which acts parallel to the surface of the plane. This means that the user is not allowed to penetrate the surface while moving along the surface. Thus, in an ideal situation the net force $\mathbf{N}$ should act tangentially to surface i.e., the normal component of $\mathbf{N}$ is

$$||\mathbf{N}^{\perp}|| = 0 \tag{4.16}$$

which will be referred to as the *sliding constraint*. Note that there always exists a theoretical solution to the sliding constraint, however due to physical limitations of the haptic device it may not be possible to adequately render the force required to satisfy the constraint.

In reality, haptic devices struggle to satisfy this condition primarily due to delays [18].

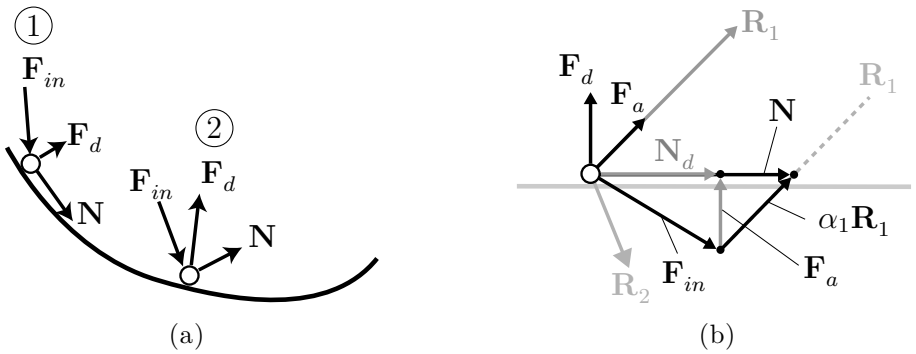

Figure 4.4: (a) Ideal and realistic forces acting at an end-effector of a haptic device when rendering a frictionless surface. (b) Sliding can be maintained even if the force output cannot be accurately displayed.

As a result, the force applied by the device can be too high, pushing the user out of the virtual wall, like in Fig. 4.4(a) case (2). Because the brake only dissipates energy, applying an excessive force blocks the user from moving, resulting in stiction [64, 66]. By inducting the sliding on the surface, the user is free to move at least in one direction unimpeded, reducing the likelihood of stiction and preserving the geometry of the virtual object.

However, completely eliminating the normal component of the net force creates problems. Consider a situation where the end-effector of a passive device penetrates a virtual surface. Eliminating the normal component of the force means that the device cannot push the user out of the wall, which could minimize the surface penetration. By allowing the net force to have a small positive component perpendicular to the plane, the device will slowly move out of the wall. To control this behavior, let $||\mathbf{N}^{\perp}|| = c$ where $c \in \mathbb{R}^{+}_{\to 0}$ is the net force constant. If a positive component of the net force is desired, c should be set to a small positive value. On the other hand, if no net force is to be displayed set $c = 0$.

To eliminate stiction in a passive device the sliding constraint must be satisfied. Note that there are many possible forces that could satisfy this constraint. If the desired force cannot be displayed by the device, it is possible to generate an approximate force to satisfy the sliding constraint.

4.3.1 Force Approximation using 1 Reference Force

Consider the situation depicted in Fig. 4.4(b). Like in Fig. 4.4(a), the frictionless virtual wall creates $\mathbf{F}_d$ normal to the surface of the wall, to stop the user from penetrating the wall. Since $\mathbf{F}_d$ does not lie on either one of the reference forces, both $\mathbf{R}_1$ and $\mathbf{R}_2$ will need to be used. Notice that the projection of $\mathbf{R}_2$ onto $\mathbf{F}_d$ is negative meaning that it must be approximated with only one force, $\mathbf{R}_1$. Let us now consider how such a force can be used to approximate $\mathbf{F}_d$.

Using only one actuator, the direction of the force output will always be the same. What changes is the net force acting on the end-effector of the device. Notice that in Fig. 4.4(b) the ideal net force $\mathbf{N}_d$, i.e. the sum of force input and the desired force, acts parallel to the wall. By applying some scaling factor α_1 to $\mathbf{R}_1$, the net force on the end-effector $\mathbf{N}$ will be generated. The direction of both $\mathbf{N}_d$ and $\mathbf{N}$ will be parallel to the wall but their magnitude will differ. This means that in either case the user will be unable to penetrate the virtual wall and in the approximated case interaction with the wall will cause more sliding. As shown in [64], to find the value of α_1 that satisfies the sliding constraint, let us take the sum of forces along the direction perpendicular to the surface of the wall,

$$||\mathbf{N}^{\perp}|| = \mathbf{F}_{in} \cdot \mathbf{F}_d + \alpha_i \ (\mathbf{R}_i \cdot \mathbf{F}_d) \tag{4.17}$$

and solve for α, replacing $||\mathbf{N}^{\perp}||$ with the net force constant

$$\alpha_i = \frac{c - \mathbf{F}_{in} \cdot \mathbf{F}_d}{\mathbf{R}_i \cdot \mathbf{F}_d}. \tag{4.18}$$

When only one reference force is available to approximate a desired force there is at most only one solution that satisfies the passivity constraint. However, as discussed in chapter 2 in devices with more DOF the forces may be approximated using several reference forces at once. For instance in a 3-DOF device, a force can be approximated using two reference forces. Using two reference forces allows the controller to better control the direction of sliding, thus, improving the force output sensation.

4.3.2 Approximating Forces with 2 Reference Forces

Consider, the case shown in Fig. 4.5(a) with a desired force $\mathbf{F}_d$, a force input $\mathbf{F}_{in}$, and two displayable reference forces $\mathbf{R}_1$ and $\mathbf{R}_2$. According to (4.18) each force can independently generate a net force satisfying the sliding constraint

$$\mathbf{N}_i = \mathbf{F}_{in} + \mathbf{R}_i \, \alpha_i \tag{4.19}$$

as shown in Fig. 4.5(b). Both $\mathbf{N}_1$ and $\mathbf{N}_2$ satisfy the sliding constraint, though their directions vary significantly. Both of these net forces lie on a plane with a normal unit vector

$$\mathbf{P} = \frac{\mathbf{N}_1 \times \mathbf{N}_2}{||\mathbf{N}_1||\mathbf{N}_2||}, \tag{4.20}$$

containing all possible forces satisfying the sliding constraint[2].

The forces a device can generate are all positive combinations of $\mathbf{R}_1$ and $\mathbf{R}_2$. These forces lie on a plane containing these two vectors. The intersection of the plane containing these forces with the plane satisfying the sliding constraint forms a line

$$\mathbf{L}_r = \mathbf{N}_1 + \mathbf{L} \, b \tag{4.21}$$

where $b \in \mathbb{R}$ $[0 \quad 1]$ is a controllable parameter, and

$$\mathbf{L} = \mathbf{R}_1 \, \alpha_1 - \mathbf{R}_2 \, \alpha_2 = \mathbf{N}_1 - \mathbf{N}_2. \tag{4.22}$$

Any point on this line can be generated using the two reference vectors and, because the lines lie on the plane defined by $\mathbf{P}$, satisfies the sliding constraint. Clearly, b can have infinitely many solutions. Which solution results in the most accurate rendering of the virtual surface?

[2]If α_i was calculated with $c = 0$ then $\mathbf{P} \parallel \mathbf{F}_d$. On the other hand, if $c > 0$, $\mathbf{P}$ will act at an angle from $\mathbf{F}_d$.

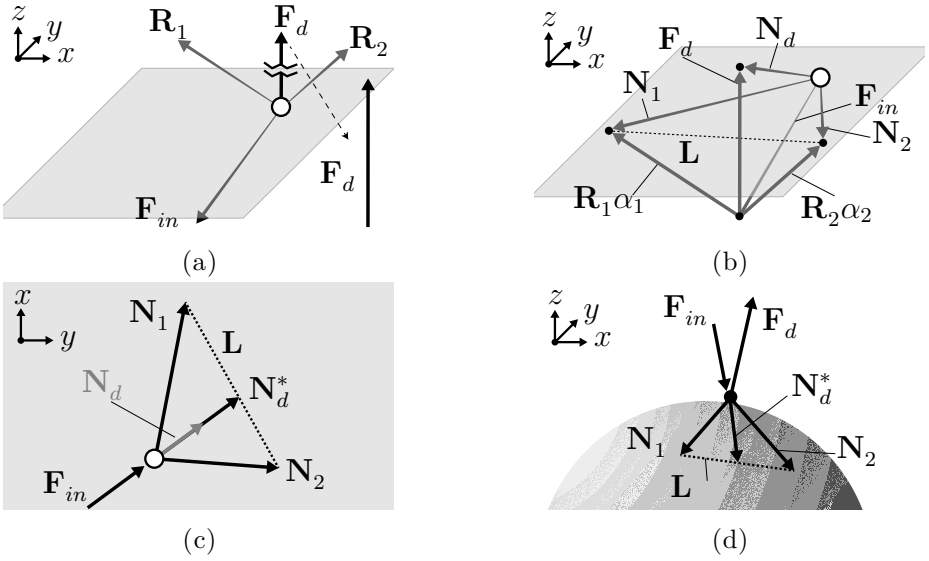

Figure 4.5: (a) Two reference vectors can approximate a force resulting from touching a plane. (b) Either of the reference forces can create a force satisfying sliding constraint. In (c) a range of net forces produced by the device is shown. By choosing a net force with the same direction as the projection of $\mathbf{N}_d$ onto the plane, results in sliding motion approximating the rendered geometry, as shown in (d).

Assume one want to render a 3D object, like a sphere, with a 3-DOF device that can only approximate the desired force with two actuators. The net forces resulting from this interaction can be seen in Fig. 4.5(d), along with the resulting line $\mathbf{L}_r$. Applying $\mathbf{R}_1$, however, results in $\mathbf{N}_1$ which is tilted counterclockwise from $\mathbf{F}_{in}$. Similarly, by using $\mathbf{R}_2$ the resulting net force $\mathbf{N}_2$ is tilted clockwise from the user input. From Fig. 4.5(d), the desired net force,

$$\mathbf{N}_d = \mathbf{F}_{in} + \mathbf{F}_d \tag{4.23}$$

lies between the two reference vectors and its scaled copy $\mathbf{N}_d^*$ lies on $\mathbf{L}_r$, making it displayable. The controller seeks to find the values of α_i that will result in $\mathbf{F}_a = \mathbf{N}_d^*$. In reality the desired force does not necessarily satisfy the sliding constraint as is the case in Fig. 4.5(a). One must, therefore, start by projecting $\mathbf{N}_d$ onto the plane defined by $\mathbf{P}$

$$\mathbf{N}_d' = \frac{\mathbf{P}}{||\mathbf{P}||^2} \times (\mathbf{N}_d \times \mathbf{P}) \,. \tag{4.24}$$

It is unlikely that this projection will coincide with the achievable net forces represented by $\mathbf{L}_r$. If $\mathbf{N}_d$ is scaled to intersect with $\mathbf{L}_r$ the resulting net force will be displayable. To find this intersection point $\mathbf{N}_d^*$, an augmented matrix may be used such that[3],

$$\left[\mathbf{L} \quad \mathbf{N}_1 \mid \mathbf{N}_d'\right] = \left[\begin{array}{cc|c} 1 & 0 & b_1 \\ 0 & 1 & b_2 \\ 0 & 0 & 0 \end{array}\right] \tag{4.25}$$

which when solved yields two constants; b_2 can be disregarded, while $b_1 \in \mathbb{R}$ $[0 \quad 1]$ gives the location of the intersection point

$$\mathbf{N}_d^* = \mathbf{N}_1 + \mathbf{L}\, b_1. \tag{4.26}$$

Finally, knowing the desired location, the set of α_i that will create the desired force is found using[4]

$$\left[\mathbf{R}_1 \quad \mathbf{R}_2 \mid \mathbf{N}_d^*\right] = \left[\begin{array}{cc|c} 1 & 0 & \alpha_1 \\ 0 & 1 & \alpha_2 \\ 0 & 0 & 0 \end{array}\right]. \tag{4.27}$$

It may be possible for b_2 to exceed its bounds. In such a case the nearest reference force should be used as the approximation. If $b_2 < 0$, $\mathbf{F}_a = \mathbf{R}_1\, \alpha_1$, and if $b_2 > 1$, $\mathbf{F}_a = \mathbf{R}_2\, \alpha_2$.

4.3.3 Approximating Forces with 3 Reference Forces

A fully displayable force may at times violate the sliding constraint due to discretization, delays, etc. Applying such a force directly can result in stiction. As a result, it is better to modify the force output such that $\mathbf{N}^{\perp} \simeq 0$. Like in previous cases, one can find a value of α_i to satisfy the sliding constraint. Unlike in previous cases, the

[3]The augmented matrix equates the equation of $\mathbf{L}_r$ and $\mathbf{N}_d'$. Note that $\mathbf{L}_r$ contains two vectors, the starting point $\mathbf{N}_1$ and the direction $\mathbf{L}$, while $\mathbf{N}_d'$ starts at the origin eliminating the need for the starting point

[4]Both (4.25) and (4.27) are 3x3 matrices with a row of zeros. This indicates that the combined vectors act in a single plane.

calculation of the scaling factors α_i can be simplified by applying a different scaling factor β_f directly to the desired torque

$$\alpha_i = \tau_{d_i}\,\beta_f \tag{4.28}$$

where β_f is the scaling factor, and τ_{d_i} is calculated using (2.3). To find β_f, once again, the sum of forces perpendicular to the plane is set to c,

$$\mathbf{N}^{\perp} = c\,\frac{\mathbf{F}_d}{||\mathbf{F}_d||} = \mathbf{F}_d\frac{\mathbf{F}_{in}\cdot\mathbf{F}_d}{||\mathbf{F}_d||^2} + \beta_f\,\mathbf{F}_d \tag{4.29}$$

and then solved for β_f

$$\beta_f = \frac{c}{||\mathbf{F}_d||} - \frac{\mathbf{F}_d\cdot\mathbf{F}_{in}}{||\mathbf{F}_d||^2}. \tag{4.30}$$

Applying β_f to the desired torques simply scales the magnitude of the force satisfying the sliding constraint.

4.3.4 Controller Design Summary

Two inputs are required to control the haptic device, namely the angular position of each actuator and the user force input, as shown in Fig. 4.6(a). The position of the end-effector, found using the forward kinematics, is then used in the virtual environment to calculate the desired force. The controller uses the desired force, along with the reference force and angular velocity, to determine the force output of the device.

The controller attempts to satisfy the sliding constraint reducing the effects of stiction and improving the force output capability of the device, using the method outlined in Fig. 4.6(b). First, the number of actuators capable of approximating the force is found using (4.13). Based on their number, the force is approximated using 1, 2 or all 3 actuators where each method is outlined in Section 4.3.1, 4.3.2, and 4.3.3 respectively.

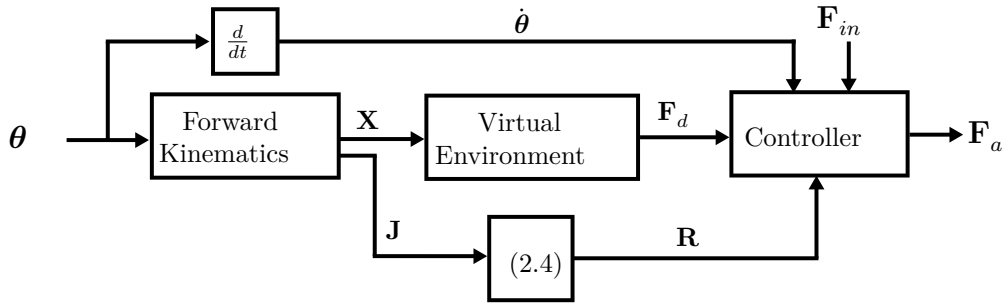

(a)

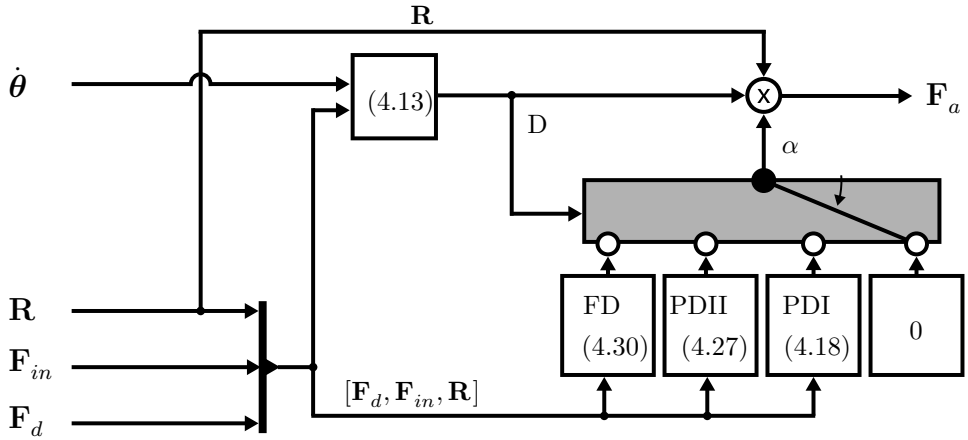

(b)

Figure 4.6: (a) The general structure of the control scheme used to control a passive haptic device. (b) A detailed breakdown of the controller, and various control cases: FD - Fully displayable, PDII - Partially displayable using two actuators, PDI - Partially displayable using one actuator, and 0 for non-displayable forces.

4.4 Experimental Evaluation

Frictionless objects are the most difficult objects to render using a passive haptic device, making them a good evaluation benchmark. A device capable of rendering a smooth virtual surface will also be able to render other types of environments with ease. To evaluate this controller six surfaces were used: 4 unique inclined planes identified by the angle separating them form the horizontal plane, shown in Fig. 4.9(a), a convex, and a concave surface, shown in Fig. 4.10. These surfaces were selected to either isolate a single mode of operation or test a combination of them.

Scenario 1 - 10° plane: The nearly horizontal plane can be rendered using all 3 actuators.

Scenario 2 - 30° plane: When rendering this plane, the device will be able to use two actuators for the majority of the trial, testing the two reference force approximation method.

Scenario 3 - 45° plane: This plane is oriented such that the device can approximate the force using only one actuator, hence testing the single reference force approximation method.

Scenario 4 - 45° plane: To render this plane the device has to switch between one and two reference force approximation methods, testing the controller's ability to switch between the different control modes.

Scenario 5 - Convex surface: To generate this geometry the desired force varies from vertical to horizontal. Therefore this test evaluates all aspects of the controller, starting with displayable forces and finishing with approximations.

Scenario 6 - Concave surface: This surface is opposite of the one in Scenario 5. Initially the desired forces must be approximated, and at the end, the forces are fully displayable.

Each of these scenarios was run with the net force constant values set to $c = 0$, $c = 0.1$, and $c = 0.5$. To generate these geometries a virtual environment must be created to

simulate interactions of the device with the virtual surfaces.

4.4.1 Virtual Environment

The desired force resulting from contact with a virtual frictionless object is dependent only on the depth of object penetration. As a result, the desired force for all cases is

$$\mathbf{F}_d = \begin{cases} \hat{\mathbf{u}}\, d\, K & \text{if } d < 0 \\ 0 & \text{otherwise} \end{cases} \tag{4.31}$$

where $\hat{\mathbf{u}}$ is the unit vector normal to the surface, d is the penetration depth into the wall, and K is the stiffness of the plane. The surfaces used in the experiments had stiffness $K = 75\,\text{kN/m}$. The unit vector normal to the inclined planes $\hat{\mathbf{u}}_p$ is known and it can be used to determine the penetration depth,

$$d = d_p = \hat{\mathbf{u}}_p \cdot (\mathbf{X} - \mathbf{X}_f) \tag{4.32}$$

where $\mathbf{X}$ is the position of the end-effector, and $\mathbf{X}_f$ is the vertical offset of the plane from the workspace origin.

A convex surface, on the other hand, is defined by the radius r from a focal point $\mathbf{O}$. Using this point and the position of the end-effector, the penetration depth and the normal unit vector for this surface are, respectively:

$$d = d_{vex} = ||\mathbf{O} - \mathbf{X}|| - r \tag{4.33}$$

$$\hat{\mathbf{u}} = \hat{\mathbf{u}}_{vex} = \frac{\mathbf{O} - \mathbf{X}}{||\mathbf{O} - \mathbf{X}||} \tag{4.34}$$

while for a concave surface the direction of the two is inverted, $d_{con} = -d_{vex}$ and $\hat{\mathbf{u}}_{con} = -\hat{\mathbf{u}}_{vex}$.

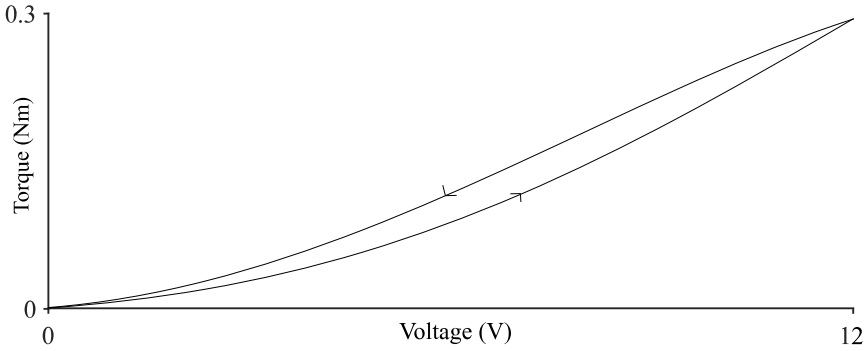

Figure 4.7: Hysteresis curve for Placid Industries B-2 Particle Brake [139]

4.4.2 Experimental Setup

A Humusoft MF 634 Data Acquisition Card measured the angular position from the encoders and controlled the voltage applied to the brakes. The forward kinematics, the virtual environment, and the controller were programmed using Simulink 2019a. The simulation ran at 2 kHz in the external mode, which minimized delays in the execution of the code.

The torque of the brake was controlled using a PWM signal with frequency of 35 kHz. The relationship between duty cycle (i.e. voltage) and the torque of the brake, shown in Fig. 4.7, indicates that the brakes are non-linear, and subject to hysteresis. In these experiments, however, the hysteresis was neglected, and only the increasing curve in Fig. 4.7 was used.

To ensure consistent behavior of the device, a 500 g mass was placed at the end-effector generating a constant downward force of 4.90 N. It was assumed that the mass of the device observed from the end-effector was 350 g meaning that the total force acting on the end-effector was 8.3 N. Notably, a force sensor was not used in these experiments. During each trial, the end-effector was lifted using a string to a region outside of the virtual object, and then slowly released onto the virtual surface.

4.4.3 Results

The experimental results are divided into three sets: Fig. 4.8 and Fig. 4.9 show the results for the four inclined planes while the results for the two curved surfaces are in Fig. 4.10. The figures are divided into sets for each evaluated scenarios. Each set contains 3 runs each with a different value of the net force constant. The first figure in each set, labelled (a), contains a 3-D plot of the rendered surface along with the path taken by the end-effector when it was in contact with this surface. Next, figures labelled (b) show the projected path of the end-effector onto the surface it slid on. The depth of plane penetration for all cases is shown in (c) while (d) shows the number of actuators used to display the forces. The magnitude of the applied force is plotted in (e), while (f) shows the estimated component of the force acting perpendicular to the plane.

4.5 Discussion

To assess the effectiveness of the controller, let us consider the controller's ability to prevent stiction, the depth of surface penetration, and the effects of the net force constant.

4.5.1 Stiction and Sliding Along a Plane

In an ideal situation, after initiating the contact with the surface the end-effector moved smoothly along the surface. To observe the motion of the end-effector with respect to the virtual surface the path of the device is projected onto the surface in Fig. 4.8(c), Fig. 4.9(c), and Fig. 4.10(c). The projection of the path on an inclined plane should be a vertical line, indicating that the device moved down the plane without any sideways motion. For a curved surface, the equivalent of the ideal path is a longitudinal line.

To set a baseline for evaluation, required geometries were rendered without using the proposed control scheme by actuating the brakes with the desired torque. In all cases,

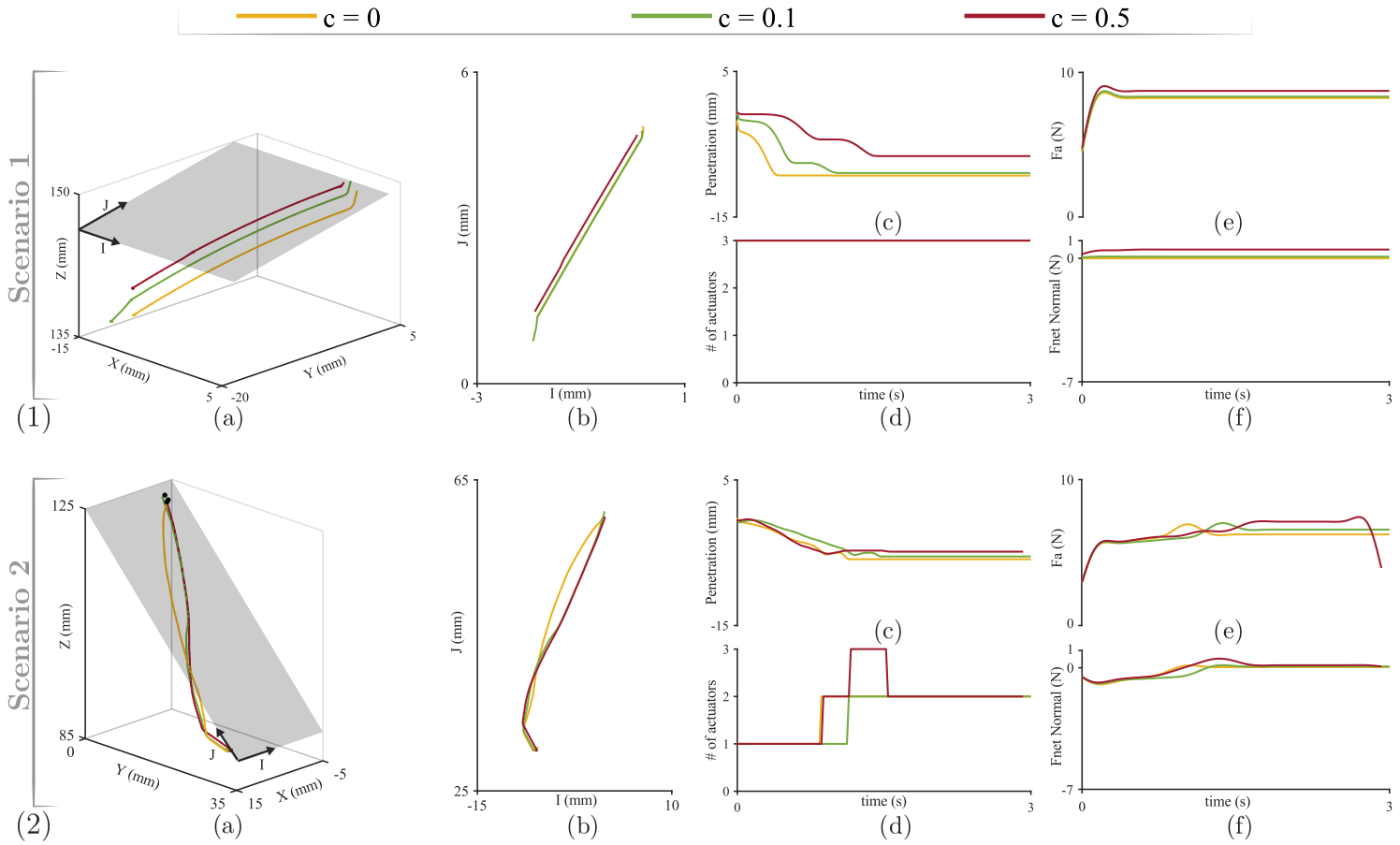

Figure 4.8: The results of rendering two inclined planes: a 10° in (1) , 30° in (2). For each case, the 3D overview of device's path along with the rendered geometry is shown in (a). In (b) the projection of the path onto the virtual plane is shown in the coordinate system of the plane. (c) shows the depth of penetration, while (d) displays the number of actuators used to generate the force. The filtered magnitude of the applied force is shown in (e), while the filtered net force perpendicular to the plane is shown in (f).

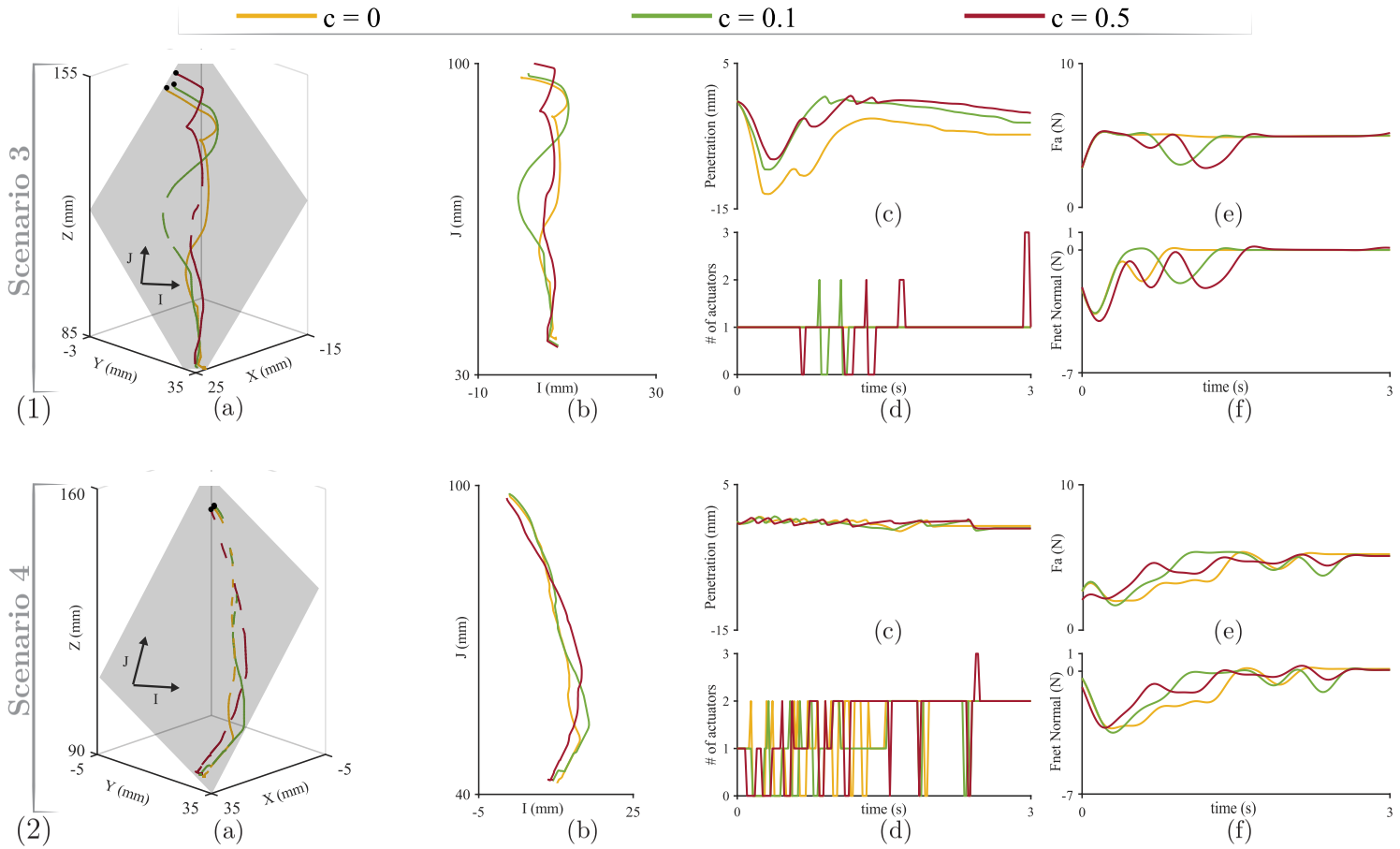

Figure 4.9: The results of rendering two inclined planes: 45° in (3), and 45° (4). For each case, the 3D overview of device's path along with the rendered geometry is shown in (a). In (b) the projection of the path onto the virtual plane is shown in the coordinate system of the plane. (c) shows the depth of penetration, while (d) displays the number of actuators used to generate the force. The filtered magnitude of the applied force is shown in (e), while the filtered net force perpendicular to the plane is shown in (f).

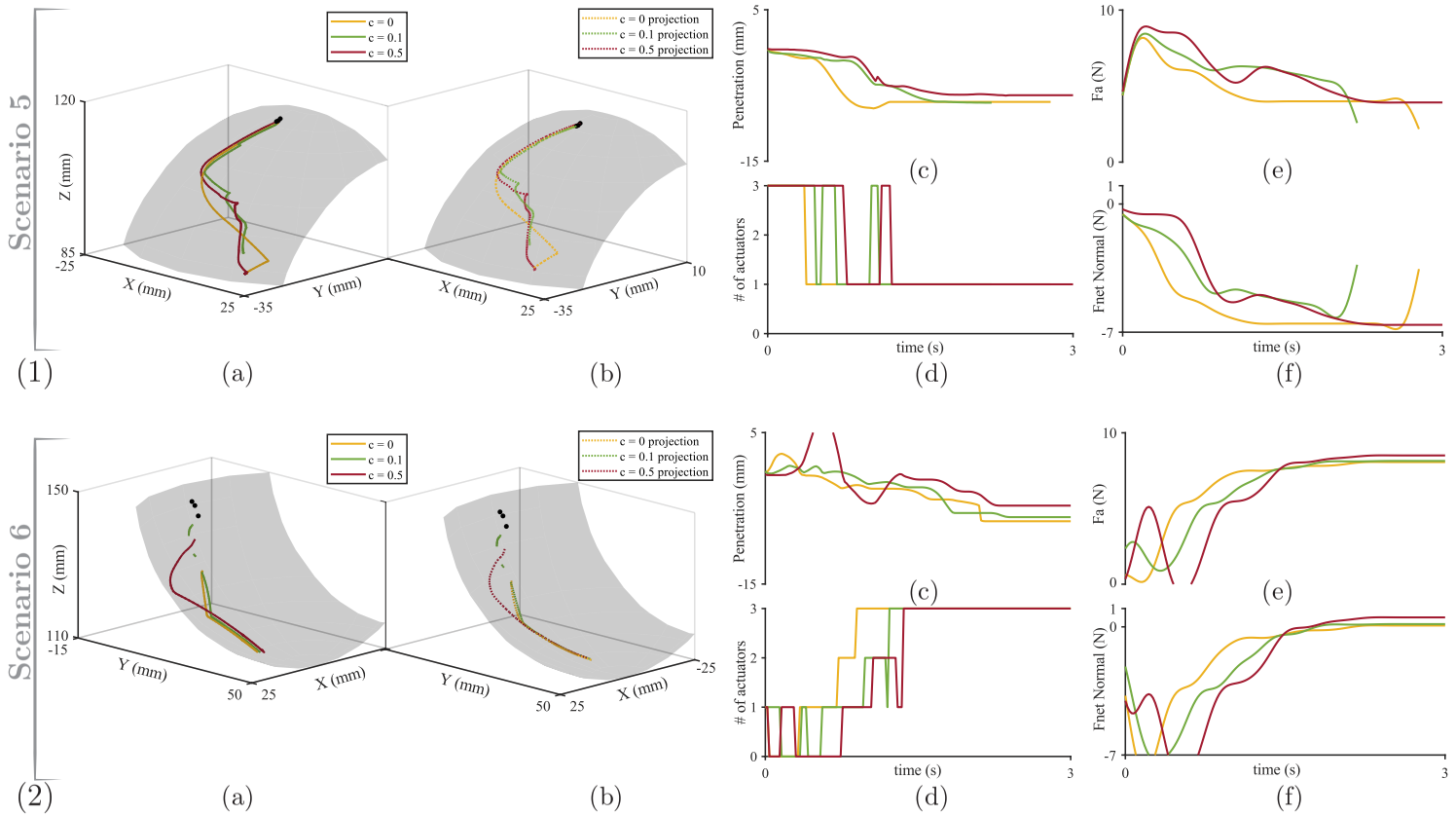

Figure 4.10: The results of rendering two curved surfaces: one convex (1), and the other concave (2). For each case, the 3D overview of device's path along with the render surface is shown in (a). (b) shows the projection of the path onto the surface. (c) shows the depth of penetration, while (d) displays the number of actuators used to generate the force. The filtered magnitude of the applied force is shown in (e), while the filtered net force perpendicular to the surface is shown in (f).

this led to immediate stiction as the desired force imminently saturated the brakes. The results for this case were indistinguishable among different test scenarios. The end-effector did not move past the initial contact point with the plane, and due to saturation, the same force was applied for all the case. This behavior was consistent through all the experiments, and thus, it is not shown here. In contrast, when using the controller the device consistently slid along the surfaces, as shown in Fig. 4.8(b) and Fig. 4.9-(b) for scenarios 1 to 4 and in Fig. 4.10-(b) for scenarios 5 and 6.

In the majority of the tests, however, the projection of the line was not perfectly vertical which indicates that the device moved sideways on the plane. One of the reasons for this motion is the effect of the single reference force approximation, like in Fig. 4.9 for scenario 3 and in Fig. 4.10 for scenario 5. When only one reference force was available, as expected, the direction of sliding was not controllable. In all other runs, the sideways motion was consistent between runs. This may have been caused by the initial conditions like the horizontal velocity of the end-effector and its initial contact point with the plane. This maximum sideways motion was approximately 10 mm and it occurred in scenario 4, shown in Fig. 4.9. This error may be eliminated in cases where two or more actuators are used, and by obtaining a more accurate force input which would account for the force resulting from the dynamics of the device. Despite this error the controller can eliminate stiction and induce sliding along the various surfaces.

4.5.2 Surface Penetration

Ideally, the device should stop the user from penetrating the rendered surfaces. Any plane penetration is a result of an imbalance of forces perpendicular the virtual surface. When rendering the 10° plane, shown in Fig. 4.8 for scenario 1, the balance of forces was theoretically maintained at or near 0, depending on the value of the net force constant, as shown in (f). In (c), however, the surface penetration clearly increased during the run, and ultimately levelled near the depth of 10 mm. The difference between the theoretical and the actual behavior suggests that the cause of this

penetration is external to the controller. Likely, this error is caused by a combination of the delay in the response time of the brakes, the simplified model of the device dynamics, and error in approximating the hysteresis of the brakes.

Surface penetration was also caused by the single brake force approximation. Consider the net force perpendicular to the plane in Fig. 4.8 and Fig. 4.9 for scenarios 2 to 4 and in Fig. 4.10 for scenarios 5 and 6. In these cases, the net force was less than zero at some instances which indicates that the controller could not eliminate the non-zero net force. Notice, also, that these cases correspond to instances when a single reference force approximation was in use and thus the force output capability of the device is bounded to the force and torque capability of a single actuator.

The plane penetration is, therefore, the result of unmodelled behaviors, linearization, and the single reference force approximation. Improving the model can result in a significantly smaller penetration depth in all of the runs. Despite these limitations and simplifications, the controller was able to stop the user from penetrating the virtual surfaces. By tuning the net force constant, the effects of plane penetration can be improved even without the aforementioned improvements.

4.5.3 Tuning the net force constant

The net force constant c from (4.18) is a tunable parameter which changes the balance of forces perpendicular to the surface. If $c = 0$, the device will move without attempting to eliminate any potential surface penetration. Increasing the value of the net force constant increases the magnitude of the applied force, as shown in Fig. 4.8(e), Fig. 4.9(e), and Fig. 4.10(e). This, in turn, results in a higher net force acting perpendicular to the plane, as shown in Fig. 4.8(f), Fig. 4.9(f), and Fig. 4.10(f). The effect of c on both the applied and the net force is the easiest to observe in Fig. 4.8 for scenario 1 since all the forces in this scenario are fully displayable.

By increasing the net force perpendicular to the plane, the device can eventually eliminate penetration, as shown in Fig. 4.9 for scenario 3. In some cases, however, an increase in the net force constant caused the device to move out of the surface

repeatedly, leading to the chattering visible in Fig. 4.9 for scenario 4. To eliminate it, the net force constant needs to be reduced, which should result in a plane that feels smooth.

4.5.4 Rendering Other Virtual Environments

The testing scenarios considered here represent the worst-case scenario for a passive haptic device; simple frictionless objects with constant force input. In most haptic applications, however, the virtual environment behaves much differently from these extreme cases. For instance, sliding along a plane is an uncommon occurrence. It is much more common for the device to interact with soft objects, such as human tissue, which involves rendering damping and friction. Forces due to friction oppose the motion of the user, and the resulting desired force should, therefore, be easier to recreate. Virtual environments are often significantly more complex than spheres and planes used in the validation experiments. If the rendered object is more intricate, then the penetration depth of the device is less likely to accumulate over time.

Despite the assumptions, un-modelled dynamics, and nonlinearities, the controller successfully eliminated stiction, while rendering the desired geometry. These uncertainties can be eliminated using either a force sensor, better dynamic model of the device, or tuning of the net force constant. In addition, the impact of these errors is amplified in the experimental results; in real applications the penetration depth and sideways motion will be more subtle. As a result, the controller should accurately render the forces in many haptic simulations.

4.6 Conclusions

The lack of haptic feedback is a limiting factor in the field of robotic surgery and surgical simulation. These applications require transparent haptic devices producing a wide range of impedance in a stable and controllable way. To satisfy these requirements a 3-DOF passive haptic device with a parallel kinematic structure was

developed along with a novel controller aimed at improving its performance.

The novel controller improves the range of forces the device generates and eliminates stiction. By adjusting the force output of individual brakes, the controller eliminates the normal component of the net force perpendicular to the virtual surface. Unlike other documented controllers, it approximates forces using combinations of 1, 2, and 3 actuators. The controller was experimentally validated using six testing scenarios. In these tests, the controller successfully modified the force output of the device resulting in a smooth motion along the given surface. Despite numerous model simplifications, such as the simplified dynamic model of the device and linearized hysteresis, the controller was able to accurately render the desired geometry. Naturally, the device experiences some position error attributed to factors other than the controller function.

The device uses passive actuators with a parallel kinematic structure which has many advantages over conventional haptic devices. Due to the parallel kinematics, the structure of the device is light and rigid. It uses brakes as actuators, therefore, it does not require the use of gearboxes, which harm transparency, making it ideal for operations where transparency is a key requirement, like simulation of laparoscopic procedures. Due to its intrinsic stability, the device can also generate high impedance without the risk of instability. As a result, the device is well suited for rendering virtual fixtures guiding the user towards a target in a safe, and controllable way. This stability of the device also makes it ideal for applications where the surgeon interacts with sensitive tissue like nerves or the brain.

An intrinsic feature of passive haptic devices is their inability to generate active forces. This makes the device less suitable for applications like beating heart surgery, lung operations, or drilling operations, where the virtual environment induces motion on the tools i.e., the environment is active. On the other hand, the impedance range of the device limits the usefulness for specialized procedures, like eye surgery, which involves minimal force-feedback. Lastly, the device has 3 translational DOF which makes the device unsuitable for procedures requiring torque feedback. However, since

the device motion is purely translational, a 3 DOF rotational feedback device can be easily added on the top of the device, like in [102]. In such a case, the proposed controller will function the same as before.

The dynamic range of the device could be improved by using magnetorheological (MR) brakes that have lower off-state torque and a higher torque output capability [51, 140]. Lastly, using a brake and a motor in tandem can either increase the impedance displayable by the device [69, 77] or to compensate inertia, friction, and gravity, improving its transparency. Since the actuators in the system are attached to an immobile base platform, this addition will not increase the apparent mass of the device. Using the device to render virtual environments requires an accurate force measurement which conventionally is provided by a force sensor. Using a more accurate force input estimation can aid in eliminating the plane penetration. Since force sensors are heavy and expensive a force observer could be implemented to estimate the force input of the user without introducing additional mass which is the focus of the next chapter.

Chapter 5

Force Input Estimation using a Nonlinear Disturbance Observer

FORCE measurements are indispensable to control passive haptic devices. Force sensors, however, are challenging to integrate as the added mass reduces transparency and measurement noise narrows the bandwidth [65]. While the force approximation schemes presented in Chapter 4 requires an accurate force measurement, the control of stationary brakes only requires the direction of the force input. Recall that per (1.9) the user force input determines both the direction and magnitude of the force output. Assuming that a low fidelity force estimate can be obtained when the device is stationary, it may be possible to adapt the controller presented in the previous chapter such that it requires no accurate force measurement when the device moves.

One method of achieving this goal is through the use of the energy-based controller introduced in [66]. Much like the force approximation scheme presented in the previous chapter, this controller attempts to eliminate the net force acting perpendicular to the virtual surface, but instead of force measurements it uses the estimated energy exchanged between the user and the virtual environment. This non-model-based controller is simple to integrate, however, it is difficult to adapt for multi-DOF force approximations. Thus, to achieve sensorless control of a 3-DOF device the force input must actually be estimated.

Force estimation schemes generally use model-based disturbance observers to estimate an external force. In [141, 142], the disturbance observer uses an inverse dynamic model with a low-pass filter to estimate the disturbances acting on the device. Expanding this observer to each joint of a multi-DOF manipulator allows for the estimation of the torque applied to each joint [143]. The observers presented in [141–143] base their structure on linearized models of highly nonlinear device dynamics which means that their global stability is not guaranteed.

Nonlinear disturbance observers (NDOs) are a superior choice for robotic manipulators as they require no model linearization, no acceleration measurement, and are proven to be asymptotically stable. The first NDOs, introduced in [144], were limited to 2-DOF planar device, however their use quickly expanded to devices functioning in

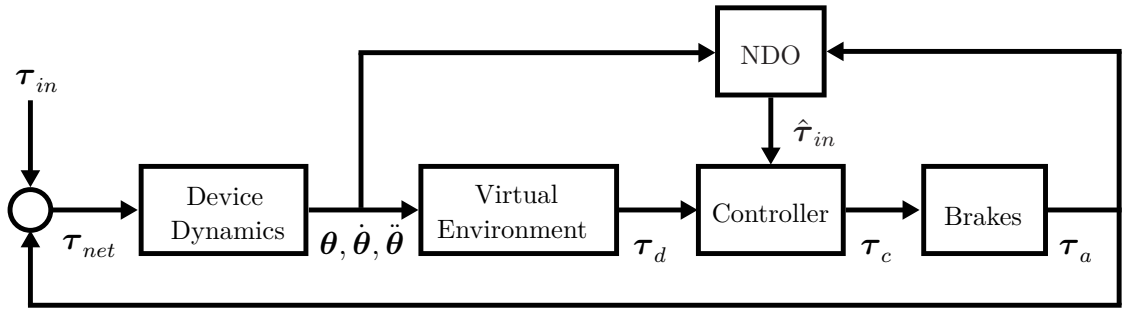

Figure 5.1: The torque input estimate $\hat{\boldsymbol{\tau}}_{in}$ of the NDO replaces the torque measurement $\boldsymbol{\tau}_{in}$ as the input to the controller. To this end, the NDO requires measurements of the joint positions $\boldsymbol{\theta}$ and velocities $\dot{\boldsymbol{\theta}}$, along with the plant output estimate $\boldsymbol{\tau}_a$.

3D space [145] followed by n-DOF manipulators in [146]. NDOs were previously used in haptic applications for closed-loop force [147] or impedance control [148] and in many other applications [149]. To the best of our knowledge, NDOs have not been used for control of passive haptic devices.

This chapter explores the possibility of using a nonlinear disturbance observer to estimate the force input in a passive haptic device. The preliminary analysis is based on the 3-DOF parallel device introduced in Chapter 4 and aims to prove, using a simulation, that the force applied to a moving end-effector can be estimated and that such an estimate is sufficient for the control of the device using a force approximation controller.

To this end Section 5.1 introduces the structure of the NDO, along with the dynamic model of the 3-DOF parallel passive device from Chapter 4. Next, in Section 5.2 the observer is validated using a series of simulated tests aimed at proving the observer's ability to estimate various types of force inputs. The preliminary results are then evaluated in Section 5.3 to determine the feasibility of the presented approach in context of controlling a multi-DOF passive haptic device without an accurate force measurement.

5.1 Observer Design

The controller proposed in Chapter 4 requires an estimate of the force input, see Fig. 4.6. By integrating an NDO, the estimated force input can be fed directly into the controller like in Fig. 5.1. Since NDO is a model-based scheme, it requires a dynamic model of the device. The modelling approach used here is based on the analysis presented in [135].

5.1.1 Dynamic Model

The 3-DOF parallel passive device has three actuated joints with position represented by $\boldsymbol{\theta} = [\theta_{11}\ \theta_{12}\ \theta_{13}]^{\mathrm{T}}$, velocity $d\boldsymbol{\theta}/dt = \dot{\boldsymbol{\theta}}$ and acceleration $d\dot{\boldsymbol{\theta}}/dt = \ddot{\boldsymbol{\theta}}$. Its dynamic model is given by the second order nonlinear differential equation:

$$\mathbf{M}(\boldsymbol{\theta})\ddot{\boldsymbol{\theta}} + \mathbf{C}(\boldsymbol{\theta}, \dot{\boldsymbol{\theta}})\dot{\boldsymbol{\theta}} + \mathbf{G}(\boldsymbol{\theta}) = \boldsymbol{\tau}_a + \boldsymbol{\tau}_{in} \tag{5.1}$$

where $\{\boldsymbol{\tau}_a, \boldsymbol{\tau}_{in}, \mathbf{G}(\boldsymbol{\theta})\} \in \mathbb{R}^{3\times 1}$, $\{\mathbf{M}(\boldsymbol{\theta}), \mathbf{C}(\boldsymbol{\theta}, \dot{\boldsymbol{\theta}})\} \in \mathbb{R}^{3\times 3}$ represent the applied torque, the input torque, the gravity vector, and the inertia, and Coriolis matrices, respectively. The matrices in (5.1) are given using Newtonian dynamic analysis [135] as:

$$\begin{aligned}
\mathbf{M}(\boldsymbol{\theta}) &= I_a\mathbf{I} + m(\mathbf{J}^{-1})^{\mathrm{T}}\ \mathbf{J}^{-1} \\
\mathbf{C}(\boldsymbol{\theta}, \dot{\boldsymbol{\theta}}) &= c_d\mathbf{I} + m(\mathbf{J}^{-1})^{\mathrm{T}}\ \frac{d}{dt}(\mathbf{J}^{-1}) \\
\mathbf{G}(\boldsymbol{\theta}) &= -ag\left(\frac{m_a}{2} + m_b\right)\cos(\boldsymbol{\theta}) - m(\mathbf{J}^{-1})^{\mathrm{T}}\begin{bmatrix}0\\0\\g\end{bmatrix}
\end{aligned}$$

with the Jacobian matrix $\mathbf{J} \in \mathbb{R}^{3\times 3}$ given in (4.7) and

$$\begin{aligned}
I_a &= I_m + \frac{m_a a^2}{3} + m_b\ a^2 \\
m &= 3m_b + m_c
\end{aligned}$$

Table 5.1: Physical characteristics of each link in the 3-DOF passive haptic device. I_m is the brakes' mass moment of inertia, c_d is the viscous damping of the actuator, m_a the mass of link a, m_b is the equivalent mass of link b, and m_c is the mass of the end-effector.

I_m (mm^4)	m_a (g)	m_b (g)	m_c (g)	c_d (Ns/m)
8.5	6.8	16	10	.01

where m_a, m_b, and m_c, represent the mass of links a, b, and the end-effector; c_d is the viscous damping of the brake and g is the acceleration due to gravity. Note that there is no known closed form solution to d/dt $(\mathbf{J}^{-1})$ therefore this term must be approximated numerically [136]. The link lengths of the device are given in Table 4.1 while Table 5.1 summarizes their physical characteristics.

This dynamic model disregards the forces resulting from motion of link b, see Fig. 4.2, as link b is assumed to move slowly and has insignificant mass.

5.1.2 Nonlinear Disturbance Observer

The nonlinear disturbance observer, shown in Fig. 5.2, has the following form:

$$\dot{\mathbf{z}} = -\mathbf{L}(\boldsymbol{\theta}, \dot{\boldsymbol{\theta}})\mathbf{z} + \mathbf{L}(\boldsymbol{\theta}, \dot{\boldsymbol{\theta}}) \left(\mathbf{C}(\boldsymbol{\theta}, \dot{\boldsymbol{\theta}}) + \mathbf{G}(\boldsymbol{\theta}) - \boldsymbol{\tau}_a - \mathbf{p}(\boldsymbol{\theta}, \dot{\boldsymbol{\theta}}) \right) \tag{5.2a}$$

$$\hat{\boldsymbol{\tau}}_d = \mathbf{z} + \mathbf{p}(\boldsymbol{\theta}, \dot{\boldsymbol{\theta}}) \tag{5.2b}$$

where $\mathbf{z} \in \mathbb{R}^{3\times 1}$ represents internal observer states, $\mathbf{L}(\boldsymbol{\theta}, \dot{\boldsymbol{\theta}}) \in \mathbb{R}^{3\times 3}$ is the observer gain matrix which is given as

$$\mathbf{L}(\boldsymbol{\theta}, \dot{\boldsymbol{\theta}})\ \mathbf{M}(\boldsymbol{\theta})\ddot{\boldsymbol{\theta}} = \begin{bmatrix} \dfrac{\partial \mathbf{p}(\boldsymbol{\theta}, \dot{\boldsymbol{\theta}})}{\partial \boldsymbol{\theta}} & \dfrac{\partial \mathbf{p}(\boldsymbol{\theta}, \dot{\boldsymbol{\theta}})}{\partial \dot{\boldsymbol{\theta}}} \end{bmatrix} \begin{bmatrix} \dot{\boldsymbol{\theta}} \\ \ddot{\boldsymbol{\theta}} \end{bmatrix} \tag{5.3}$$

and the auxiliary function $\mathbf{p}(\boldsymbol{\theta}, \dot{\boldsymbol{\theta}})$ eliminates the need for the acceleration measurements [144]. For a 3-DOF manipulator a possible formulation for the auxiliary variable is [148]

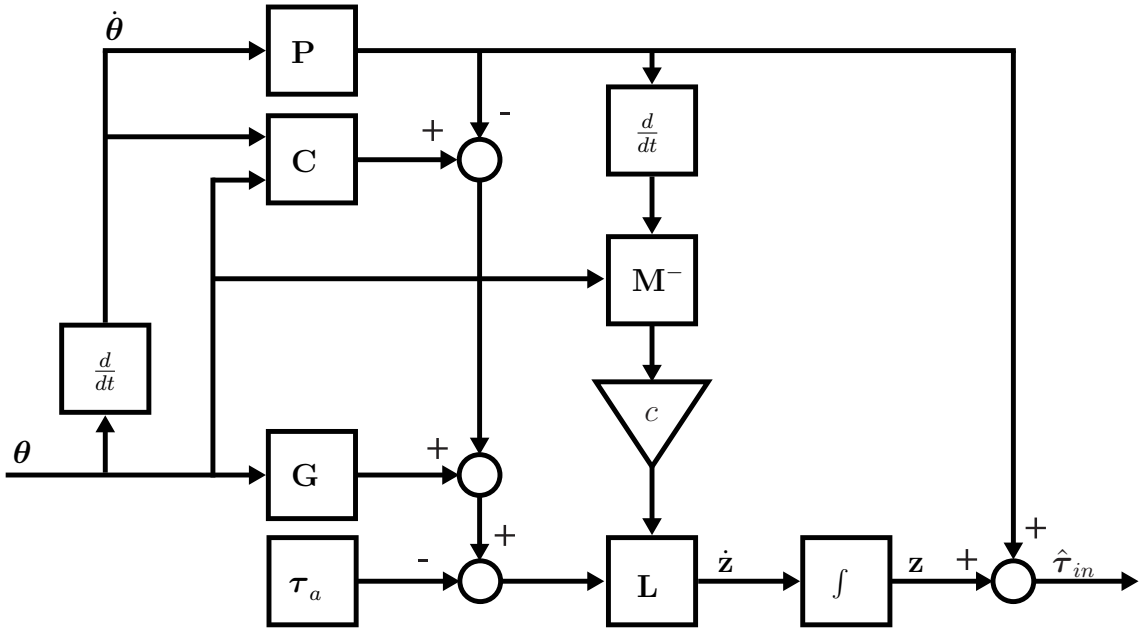

Figure 5.2: The nonlinear disturbance observer uses angular position $\boldsymbol{\theta}$ and velocity $\dot{\boldsymbol{\theta}}$ of the device along with the torque applied by the brakes $\boldsymbol{\tau}_a$ to estimate torque input $\hat{\boldsymbol{\tau}}_{in}$.

$$\mathbf{p}(\boldsymbol{\theta}, \dot{\boldsymbol{\theta}}) = c \begin{bmatrix} \dot{\theta}_{11} \\ \dot{\theta}_{11} + \dot{\theta}_{12} \\ \dot{\theta}_{11} + \dot{\theta}_{12} + \dot{\theta}_{13} \end{bmatrix} \tag{5.4}$$

giving the observer gain matrix as

$$\mathbf{L}(\boldsymbol{\theta}, \dot{\boldsymbol{\theta}}) = c \begin{bmatrix} 1 & 0 & 0 \\ 1 & 1 & 0 \\ 1 & 1 & 1 \end{bmatrix} \mathbf{M}(\boldsymbol{\theta})^{-1} \tag{5.5}$$

which can be proven to be asymptotically stable for a range of c, which represents a controllable observer gain [144, 145].

NDOs are formulated on the assumptions that disturbance varies relatively slowly and that all functions in the dynamic model of the device are smooth. As shown in [144], however, NDOs can estimate fast varying disturbances. In context of passive haptic devices, it must also be assumed that no brake is stationary during the operation, as the states of a stationary brake are not observable.

5.2 Simulation Results

A human operator can apply a wide range of forces to the device, at a wide range of frequencies. The simulations must, therefore, test the ability of the observer to estimate the input force in a variety of conditions. The testing scenarios 1 and 2, detailed below, validate the observer for cases where the device is not rendering forces to the user, so called free motion. Scenarios, 3 and 4, on the other hand, test the observer as a component in the force approximation scheme from Chapter 4. Finally, scenarios 5 and 6 compare the observer and the controller performance with uncompensated brake hysteresis in the dynamic model of the device.

Scenario 1 - Free motion with constant vertical force input: In this scenario, the force applied to the end-effector has only a vertical Z component following a square wave pattern to $\pm$400mN at a frequency of 1Hz. This scenario tests the NDO's ability to converge when subjected to an un-smooth force input.

Scenario 2 - Free motion with varying force input: The force in this scenario simulates the input of a user; the forces are smooth and vary in the X, Y, and Z axes. The magnitude of the applied forces in the Z axis is approximately 10N and about 5N along the X and Y exes with a frequency of 3.5Hz. This scenario evaluates observer's ability to estimate fast varying forces acting in arbitrary directions.

Scenario 3 - Rendering a displayable desired force in the vertical axis: Similar to the first scenario, the force input is a square wave in the Z axis with a magnitude of 400mN and a frequency of 2Hz. In this scenario the haptic device attempts to display a desired force. The desired force is a sine wave with a magnitude of 100mN and a frequency of 1Hz. This scenario compares the output of the force control scheme from Chapter 4 when using the actual and estimated force input, where the desired force is displayable.

Scenario 4 - Rendering partially displayable forces, with a varying force input: Like in Scenario 2 the force input simulates the user moving the device in the X, Y, axes and Z axes with a force magnitude of 10N in the Z axis, and 5N in the X and Y,

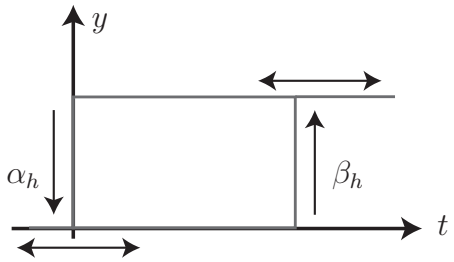

Figure 5.3: Hysteresis loop of a nonideal relay with excitation thresholds of α and β.

all at a frequency of 3.5Hz. The desired force has a magnitude of 5N in the Z axis, and 2N in the X and Y axes all at a frequency of 0.5Hz. This scenario compares the output of the force approximation control scheme when using the force input and its estimate when the force is fully, partially, and non-displayable.

Scenario 5 - Rendering a force in the vertical axis and uncompensated hysteresis: The force input and the desired force are the same as in scenario 3, however, the torque generated by the brake is subject to hysteresis. This scenario tests the ability of the observer to converge when the device model does not account for all device dynamics.

Scenario 6 - Rendering a varying force, with a varying force input and uncompensated hysteresis: The force input and the desired force are the same as in scenario 4, however, the torque generated by the brakes is subject to hysteresis. This scenario tests the performance of the NDO and force control scheme from Chapter 4 when the force input is not the only disturbance in the system.

The simulations were conducted using MATLAB Simulink 2020a running at 1kHz sampling frequency. The device dynamics obey the equations given in Section 5.1.1 while the forward kinematics is found using the method presented in Section 4.1.3. For simplicity, gravity is omitted in the simulations such that the only force acting on the device is the force input. The brake hysteresis in scenarios 5 and 6 is modeled using Presiach hysteresis model described below.

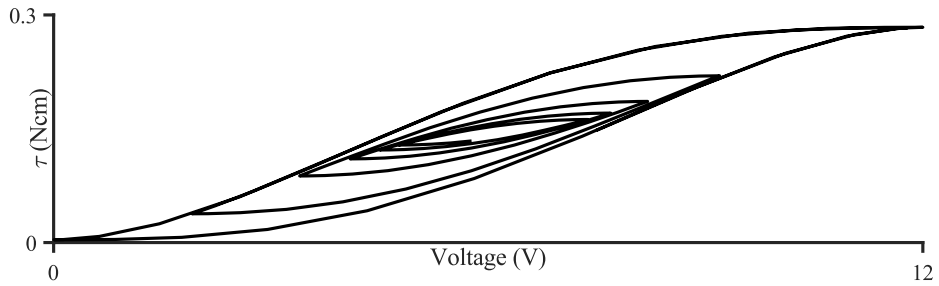

Figure 5.4: The hysteresis curve for the simulation imitates the curve of the actual particle brakes.

5.2.1 Hysteresis Model

The Preisach model is constructed using the model of a nonideal relay hysteron, see Fig. 5.3, with a square hysteresis loop described by α_h and β_h excitation thresholds such that,

$$y(t) = \begin{cases} 1 & \text{if } t \leq \alpha_h \\ y(t-1) & \text{if } \alpha_h < t < \beta_h \\ 0 & \text{if } t \geq \beta_h \end{cases} \tag{5.6}$$

where $y(t)$ is the output of the relay for input t, and $y(t-1)$ represents the previous output value. The model assumes that the magnetization properties of an object are a result of integrating the magnetization of many independent hysterons $\gamma_{\alpha_h,\beta_h}$ modelled in (5.6), such that

$$y(t) = \iint\limits_{\alpha_h \geq \beta_h} \mu(\alpha_h, \beta_h)\ \gamma_{\alpha_h,\beta_h}\ d\alpha_h\ d\beta_h \tag{5.7}$$

where $\mu(\alpha_h, \beta_h)$ is the Preisach density function [150, 151]. The analytical solution to (5.7) does not exist and, thus, its implementation is discretized into a finite number of hysterons. The shape of the resulting hysteresis loop is defined by the Preisach density function, however finding such a function is difficult [151]. The Presach function is approximated as a matrix of coefficients created using a series of linear operations. Thus obtained model results in the hysteresis loop in Fig. 5.4.

5.2.2 Results

The results for scenarios 1 and 2 are given in Fig. 5.5. Each set of results compares the force input and its estimate in the X, Y, and Z axes in (a), (b), (c), respectively. Subfigures (e), (f), (g), compare the actual torque input and its estimate at each of the three actuated joints. The angle between the actual force input and its estimate is shown in (d), while (h) compares their magnitudes.

Scenario 3 and 4 results are presented in Fig. 5.6. Subfigures (a), (b), and (c) show the force input and its estimate in the X, Y, and Z axes, respectively. The force calculated by the force approximation scheme using the force input and its estimate are compared in (e), (f), and (g), one for each of the spatial exes. The angle between the force input and its estimate is shown in (d), while (h) compares their magnitude.

Lastly, scenarios 5 and 6 are shown in Fig. 5.7, with (a), (b), (c) showing the force input and its estimate in the X, Y, and Z axes; (e), (f), (g) compare the output of the force approximation scheme using force input and its estimate; (i), (j), (k) compare desired torque and the hysteresis-uncompensated torque output of the brakes; while (l) shows the normalized error between the ideal and the actual torque applied to the brakes. The angle between the force input and its estimate is shown in (d). Finally (h) compares the actual and estimated force magnitudes. The mean and maximum direction error as well as the mean magnitude errors between the force input and its estimate are given in Table 5.2 for all six scenarios.

5.3 Discussion

To determine the feasibility of using a force estimate for force approximation in a 3-DOF passive device, let us analyze the performance of the NDO in terms of force estimation first, then discuss how errors in the force estimate affects the performance of the force approximation control scheme, and finish with the discussion of unmodlled hysteresis and its impact on the force estimation and control.

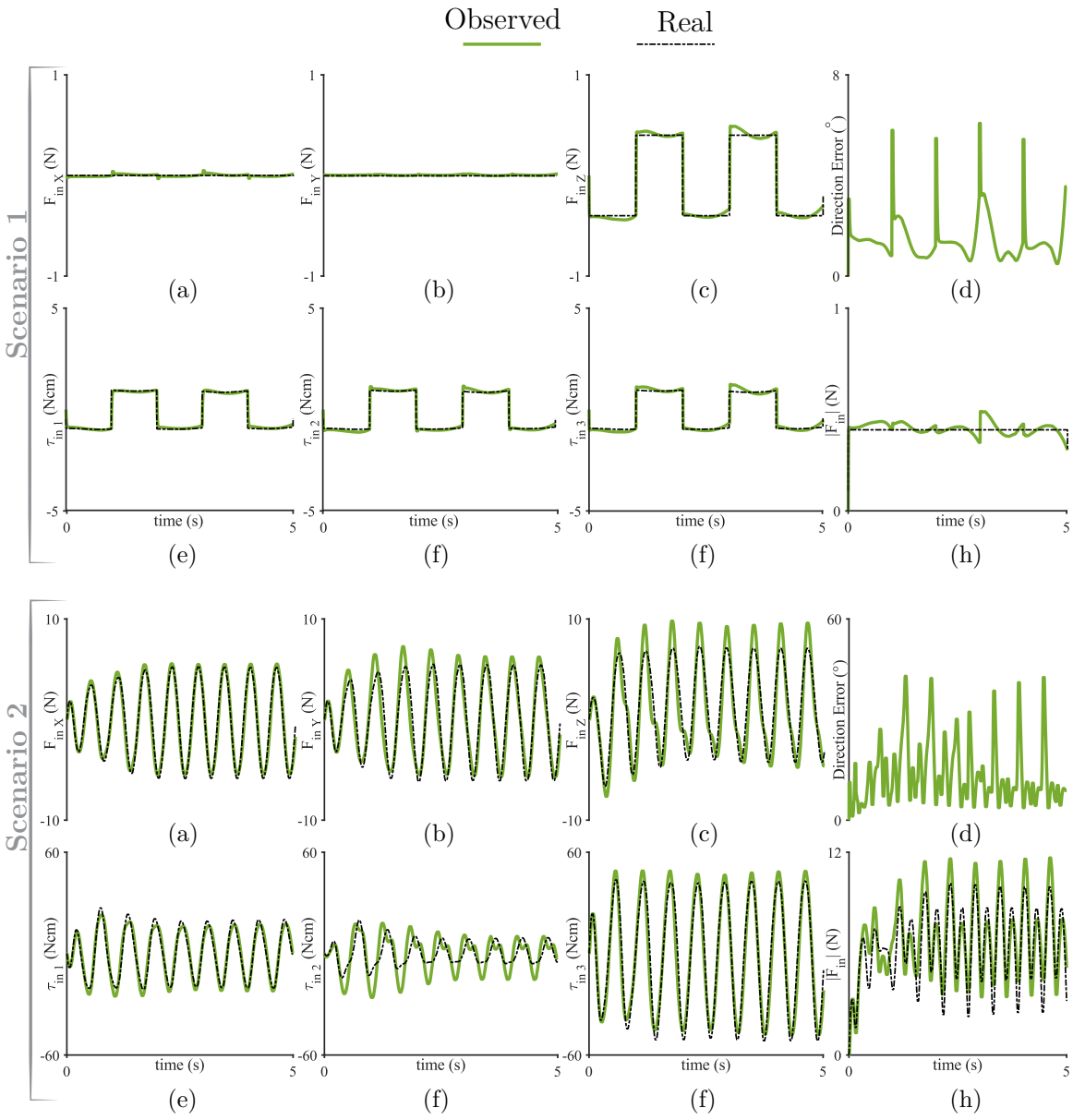

Figure 5.5: The results for scenarios 1 and 2 where (a), (b), (c) show the forces input and its estimate in the X, Y, and Z axes, the torque inputs for the three joints are in (e), (f), (g). The angle between the actual force input and the estimate is shown in (d) and the magnitude difference in (h).

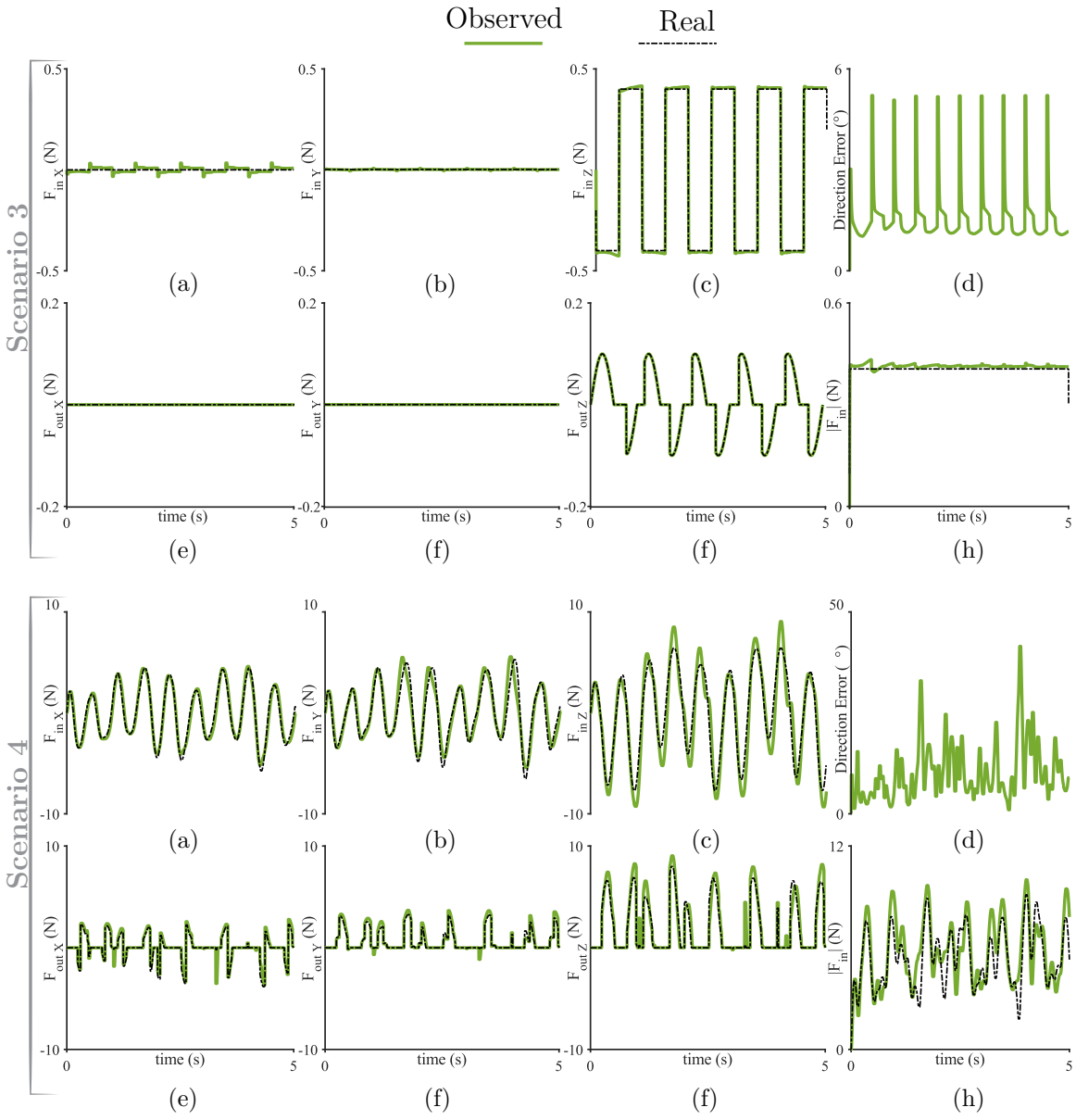

Figure 5.6: The results for scenarios 3 and 4 where (a), (b), (c) show the forces input and its estimate in the X, Y, and Z axes and the force calculated by the controller using the actual and the estimated force input in the X, Y, and Z axes is shown in (e), (f), (g). The angle between the actual force input and the estimate force input is shown in (d) and the magnitude difference is given in (h).

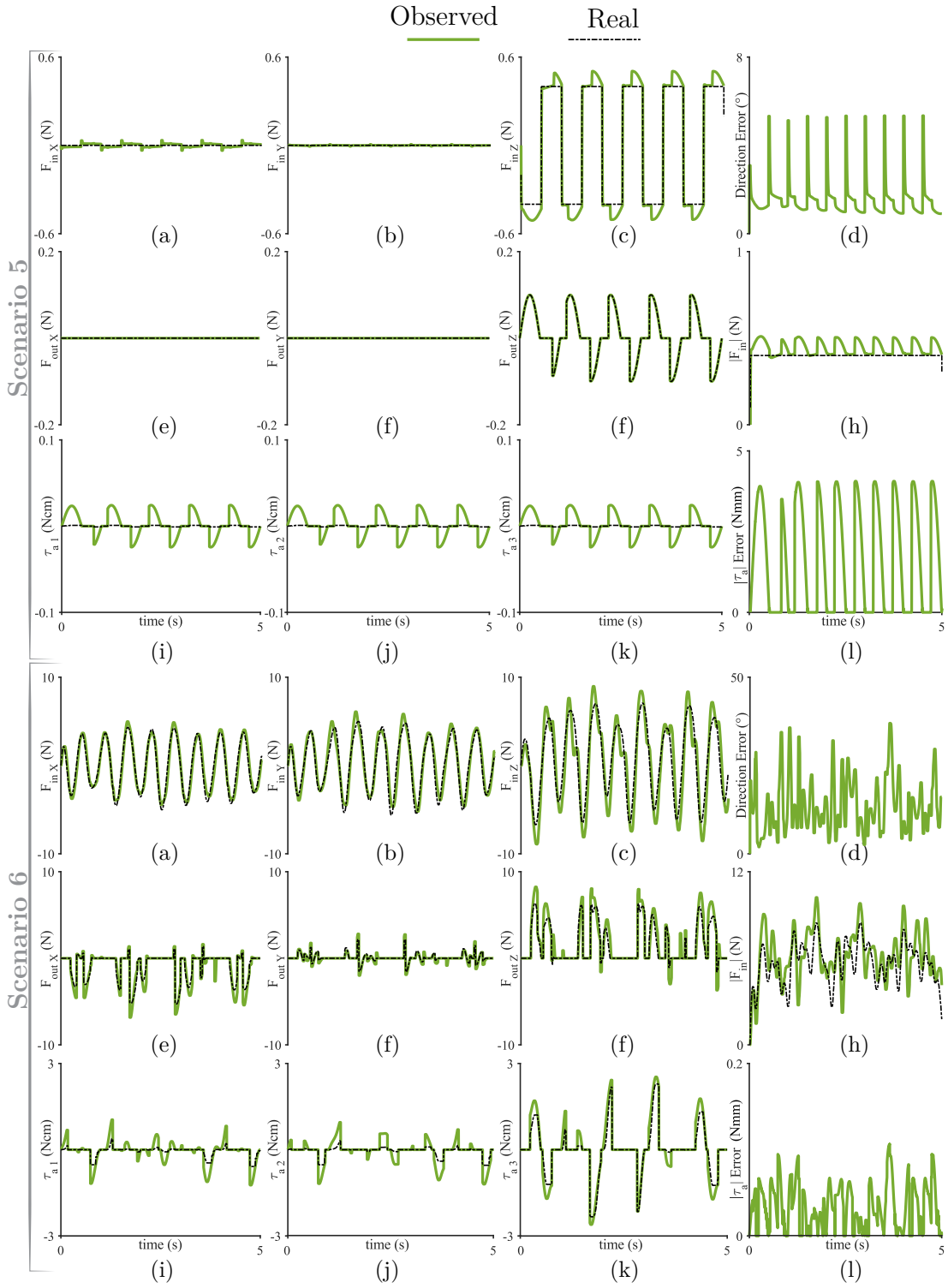

Figure 5.7: The results for scenarios 5 and 6 where (a), (b), (c) show the force input and its estimate in the X, Y, and Z axes and the force calculated by the controller using the actual and estimated force input in the X, Y, and Z axes is shown in (e), (f), (g). The angle between the actual force input and the estimate is shown in (d) and the magnitude difference in (h). The effects of hysteresis on torque output of each brake is shown in (i), (j), and (k). Lastly, (l) shows the normalized error between the ideal applied torque and the actual applied torque.

Table 5.2: The mean and maximum direction error along with the mean magnitude error between the force input and its estimate for the six scenarios.

Scenario	mean direction error (deg)	max direction error (deg)	mean magnitude error (%)
1	1.46	6.07	1.88
2	13.55	42.93	7.86
3	1.62	5.2	1.92
4	10.31	41.5	8.61
5	1.60	5.35	11.57
6	13.78	36.96	11.15

5.3.1 Force and Torque Estimation

In scenarios 1 and 2 the device is subjected only to the force input of the user. Ideally, there should be no difference between the real force and torque input and their estimates. In reality, however, the observer approximates the torque input at each joint and the resulting force estimate through kinematic of the device leading to a difference in both the magnitude and direction.

In the first scenario a vertical force is applied to the end-effector, and since the device was in the center of its workspace, that is $\theta_{11} = \theta_{12} = \theta_{13}$, the torque applied to each brake is the same. The results from Fig. 5.5 show that the estimated torques differs depending on the brake; the estimates torque at the first joint, shown in (e), is accurate while the estimates for joints two and three, see (f) and (g), have some overshoot. This type of inaccuracy is an intrinsic property of the NDO as similar patters can be seen in results obtained in [144, 145]. These errors in the torque estimate translate to errors in the estimated force, as shown in (a), (b), and (c). From (d) and (f) it is evident that when the force input changes direction there is a delay in the response of the observer resulting in the angle and magnitude difference between the force input and its estimate. The direction error after the instantaneous change in the force direction is initially 6°, but it quickly converges to below 2°. The magnitude of the force also shows a large initial spike but it also quickly converges to

approximately 2%. On average the direction of the force estimate is off by 2° and the magnitude has an error of 1.5%. Note, however, that this is the worst-case scenario for the NDO as the disturbance is not a smooth function. Despite the unfavorable conditions, the observer can still provide an accurate force estimate.

The force input in the second scenario is a smooth sinusoidal function acting in all three axes. The observer estimates the torque applied to each of the three joints with varying results. For instance, the estimate for the first and third joints, shown in Fig. 5.5(e) and (g), closely tracks the torque input, however, joint two, shown in (f), differs from the actual input torque. This error, however, does not seem to significantly affect the force estimate, shown in (a), (b) and (c). Like in scenario 1, the error in the estimate is the greatest when the force direction changes rapidly, however, since the input is smooth the spikes in the direction error, shown in (d), and magnitude, shown in (h), are far less pronounced. The maximum direction error is 43° but on average the error is only 14° while the average magnitude error is about 8%.

5.3.2 Force Approximation using Estimated Forces

Scenarios 3 and 4 incorporate the force approximation scheme from the previous chapter and compares forces calculated by the controller using the input force measurement and its estimate. Ideally, the force output calculated by the controller based on the input force estimate should be the same as the one calculated using the actual force input. The results for scenarios 1 and 2, however, show that the estimate force may have a different direction and magnitude than the actual force. In scenario 3, the force input and the desired force act in the vertical direction, meaning that the force is either fully or non-displayable; the force is never partially displayable. On the other hand, in scenario 4 both the force input and the desired force act in all three directions meaning that the force approximation will be required.

Like in the previous two scenarios, the observer estimates the force input with an average direction error of 2° and 10° for scenarios 3 and 4, respectively and an average magnitude error of 2% and 9%, respectively. The controller output using the true and

estimated force input are similar for the two scenarios, as shown in Fig. 5.6(e), (f), and (g) for each of the three axes. Notably, the output based on the observed force input is higher when the force estimate is used. The cause of this anomaly is likely the overestimation of the force input magnitude which can be observed in (h). Such overestimation changes the balance of forces at the end-effector which may lead to stiction. The direction error, on the other hand, does not seem to have a major effect on the output of the controller.

5.3.3 Effects of Unmodelled Dynamics

Scenarios 5 and 6 test the sensitivity of the NDO to unmodelled dynamics, such as the brake hysteresis. Since the user is no longer the sole contributor of disturbance in the system, the resulting force estimate is subjected to both the hysteresis and the user input.

The results in Fig. 5.7 (i), (j), and (k) show a significant difference between the output of the brake with and without unmodelled of hysteresis. In both scenarios 5 and 6, the torque output by the brake is significantly smaller than the desired torque and the error is most pronounced when rending low torques. The resulting force input estimate, shown in (a), (b), and (c), causes a noticeable increase in the error when compared with Fig. 5.6. In scenario 5 the error in the direction of the force input is nearly the same as in scenario 3, which is to be expected as the torque applied to each brake was equal. However, both the mean and the maximum magnitude errors in scenario 5, respectively 12% and 35%, were higher than in scenario 3 which were 2% and 6%. In scenario 6, on the other hand, the mean direction error was higher than in scenario 4, 14° compared with 10°, but still within a reasonably range. The magnitude error was also higher in scenario 6 compared with scenario 5, respectively 11% and 8%, which should result in an increased error in the force output of the force approximation controller.

In scenario 5 there is no difference in the output of the controller using the force input and its estimate, as shown in (e), (f), and (g). In scenario 6, on the other

hand, the error in the force input estimate is noticeably higher than that in scenario 5. This indicates that unmodled dynamics of the device can further promote stiction and, thus, must be compensated to guarantee best performance. It is worth keeping in mind, however, that the modelled hysteresis is more nonlinear than that of an actual particle brake, compare Fig. 4.7 and Fig. 5.4, and ,thus, represent the worst-case scenario. Despite the exaggerated effects of hysteresis, the results clearly show that the NDO is versatile and it can provide an estimate of the force input.

5.4 Conclusions

Control schemes for passive haptic devices depend on force measurements to render and approximate forces. The forces are typically measured using force sensors which are heavy and expensive. To reduce the reliance on the force sensor, this chapter proposes the use of a nonlinear disturbance observer (NDO) as a sensorless force estimator. The proposed approach was tested in a dynamic simulation of the 3-DOF parallel passive device from Chapter 4. The results show that the NDO can estimate the force input with a magnitude error lower than 9% and the direction error of 13° or less. The preliminary tests show that the force estimate obtained using the NDO can be used in the force approximation control schemes as a replacement for a force sensor, though the concept requires further experimental validation.

It remains to be seen how unmodelled dynamics affect the force estimation in the real world. When the force input is high, the disturbances caused by hysteresis, friction, and unmodeled dynamics should be relatively insignificant, meaning that the observed disturbance should match the user force input. On the other hand, when the force input is small the effects of internal disturbances may dominate the response. To minimize these disturbances it is necessary to use an accurate model of the device. For the 3-DOF passive device a Lagrangian model proposed in [135] may improve accuracy at a cost of increasing the computational cost [113, 152]. The hysteresis of the brakes needs to be compensated for optimal performance. This could be done using relatively simple methods, like the Presiach model [151], or more sophisticated

approach like Boc-Wen Model [153].

The NDO can only estimate forces when the device is in motion; if brakes stop moving the system is no longer observable. Note that the observer and the force approximation control are complementary in solving this problem. The force approximation scheme requires a force measurement to reduce stiction while the observer estimates the force input as long as the brakes are not stationary. In situations where the brakes do not move, for instance if the virtual environment imposes high viscous damping, a force measurement will still be required. The control of stationary brakes, however, requires only the measurement of the force input direction which can be estimated using a low fidelity force senors such as strain gauges placed in links of the device.

Chapter 6

Conclusions and Recommendations

CONVENTIONAL haptic devices that use electric motors as actuators suffer from an innate trade-off between stability and transparency, which limits their range of displayable impedance. This is a particular concern in surgical applications like robotic surgery and surgical simulation where haptic consoles need to render both high and low impedances while remaining stable and safe. One way to make haptic device more suitable for these applications involves replacing electric motors with passive actuators such as brakes. Since passive haptic devices are intrinsically stable, they can have a much higher impedance range and transparency making them ideal for surgical applications. However, the passive nature of brakes makes them difficult to control as only the magnitude of their torque can be controlled, but not the direction. As a result, these devices cannot generate forces in arbitrary directions and stiction may occur when rendering high impedance at low velocities.

For passive haptic devices to be useful in surgical applications they must have at least 3 translational DOF. The passive devices developed to date, however, are mostly constrained to planar motion. Furthermore, there is a lack of analytical frameworks and controllers capable of compensating for the drawback of passive devices with higher DOF. With the goal of developing a passive haptic device for surgical applications, this thesis presents a new set of analytical tools and controllers for higher DOF passive devices. The contributions presented in this thesis simplify the design process and provide an insight into the design trade-offs observed in higher DOF passive devices.

A feasibility analysis of higher DOF haptic devices revealed that increasing DOF also increases number of partially displayable regions while reducing the size of the fully displayable region. The analysis also introduced the concept of Degree-of-Displayability (DOD), which represents the number of actuators capable of partially rendering a force in a given region. A detailed examination of a 3-DOF manipulator revealed two types of partially displayable regions with differing DOD. The analysis also showed that the use of higher DOD regions to approximate the force is the key to developing higher DOF passive haptic devices as it not only expands the range of displayable forces but also improves the quality of the force approximation.

The analysis can be further expanded to investigate how the displayability regions change shape and size throughout the workspace of the device. A set of new performance metrics was created to measure the ability of a device to display a force in arbitrary directions as a function of the end-effector velocity direction. Applying these metrics to planar serial and parallel manipulators revealed the impact of the kinematic structure on their force displayability. The results indicated that serial manipulators and parallel manipulators with equal link lengths and base link length of zero are the best choice for general use haptic devices as their force displayability is insensitive to changes in velocity direction. The results also suggest that parallel manipulators with the base link length greater than zero could generate more forces when moving in certain directions than any other manipulator, making them ideal for applications where the virtual environment constrains the user motion to a known path. Even though the analysis was limited to planar devices, the performance metrics can accommodate spatial and redundantly actuated devices enabling the design optimization of parallel passive devices.

Based on the observations listed above, a first of its kind 3-DOF parallel haptic device was constructed. The device was intended for surgical applications therefore it used the modified *Delta* kinematic structure to make it light and rigid. The links of the device were fabricated using a combination of 3D printing and manual machining in the lab. Bearings in the joints of the device minimize friction, resulting in a device with minimal losses and damping. The device was controlled by a new force approximation scheme designed specifically for 3-DOF passive haptic devices. The controller uses all available DOD to render the desired forces, which includes a single and double reference force approximation. The controller was validated experimentally proving its ability to eliminate stiction and increase the range of displayable forces. Even though the controller was designed for 3-DOF passive devices, it can be used in non-redundant devices with more than 3 DOF, as long as the spatial and rotational DOF are decoupled. The main drawback of the controller is its reliance on the measurement of the user force input as it requires the use of a force sensor.

The reliance on force sensor can be reduced by using a nonlinear disturbance observer (NDO) to estimate the force input when the device is in motion. The preliminary simulation results indicated that the NDO can reliably estimate the force input. Using the estimate force in the force approximation control scheme provides similar results to those obtained using the true force input signal. Note, however, that the NDO cannot observer forces when the brakes of the device stop moving, meaning that a force sensor still needs to be included in the design of a passive haptic device. This control strategy requires further experimental validation to evaluate its sensitivity to unmodeled dynamics such as inertia and friction.

The contributions presented in this thesis are not exhaustive and leave room for further investigation in the aspect of analysis, design, and control of passive devices. Improving the performance of these devices requires a combination of solutions previously developed for other robotic applications, and new ones tailored specifically towards passive devices.

6.1 Recommendations

As any haptic device, the 3-DOF device presented in this thesis has a limited Z-width and transparency. Both of the issues could be solved with methods previously developed for other haptic systems. One potential method to improve transparency is to use either an active or passive gravity compensation scheme. For instance, springs could be added to balance most of the gravity forces acting on the device without introducing additional mass [106]. Alternatively, small electric motors could be added in parallel to the brakes and a separate controller could compensate not only for gravity but also for friction and inertia of the brakes [74, 81, 82, 84]. Of the two methods, the active compensation scheme offers better performance, but it adds more complexity and cost compared to the passive scheme. Increasing the dynamic range of the device can be easily solved by using stronger brakes with lower off-state torque. Compared with particle brakes used in the current design, MR brakes have a much higher torque-to-volume ratio and typically a lower off-state torque [51] making

them ideal for the application.

On a more fundamental level, passive devices are subject to two major limitations. The first issue is the reliance of these devices on a force sensor. Even though the observer presented in Chapter 5 can estimate the force input, it can only do so when the device is moving. When the device stops moving, a force measurement will still be required when the device stops moving, thus, a lower fidelity integrated force sensor could be used. Strategically placing strain gauges directly on the device links could provide a rough estimate of the force applied by the user to a stationary device. Since only the direction of torque is needed to control a stationary brake, the force estimate should not compromise the accuracy of the controller. Unlike force sensors, however, strain gauges are small, light, and inexpensive which means that they should not significantly affect the transparency or cost of the device.

The second issue is the limited range of displayable forces. As much as it is a fundamental limitation of passive devices, it is possible to greatly expand the size of the fully displayable region by introducing actuator redundancy [96]. Adding more actuators into the device increases the number of reference forces and, consequently, the range of fully displayable region, hence, improving the quality of force approximation. The analysis in this thesis was limited to non-redundant devices. The frameworks and controllers presented here for non-redundant actuators can easily be adapted for use in redundant devices. Furthermore, the analysis presented in this thesis could also be adopted for devices with more than 3 DOF, particularly in devices with coupled translational and rotational DOF.

The analytical frameworks presented in this thesis can be adopted for the analysis of all passive devices, including n-DOF and redundantly actuated manipulators, but also for analysis and design of hybrid devices. Clearly, passive actuators in multi-DOF devices, if used to their full potential, are a viable alternative to conventional actuation technique for haptic devices which may lead to the development of the ultimate transparent haptic device.

References

[1] G. Robles-De-La-Torre, "The importance of the sense of touch in virtual and real environments," *IEEE Multimedia*, vol. 13, no. 3, pp. 24–30, 2006.

[2] G. Hubens *et al.*, "What have we learnt after two years working with the Da Vinci robot system in digestive surgery?" *Acta Chir. Belg.*, vol. 104, no. 6, pp. 609–614, 2004.

[3] M. Kitagawa *et al.*, "Effect of sensory substitution on suture-manipulation forces for robotic surgical systems," *The Journal of thoracic and cardiovascular surgery*, vol. 129, no. 1, pp. 151–158, 2005.

[4] S. M. Prasad *et al.*, "The effect of robotic assistance on learning curves for basic laparoscopic skills," *The American journal of surgery*, vol. 183, no. 6, pp. 702–707, 2002.

[5] G. Jayaraman and Z. Szulyk, "Active sidestick design using impedance control," in *2009 IEEE International Conference on Systems, Man and Cybernetics*. IEEE, 2009, pp. 4432–4437.

[6] J. J. Gil *et al.*, "New driving control system with haptic feedback: Design and preliminary validation tests," *Transportation research part C: emerging technologies*, vol. 33, pp. 22–36, 2013.

[7] V. Hayward *et al.*, "Haptic interfaces and devices," *Sensor review*, 2004.

[8] B. Sainsbury *et al.*, "Evaluation of a virtual reality percutaneous nephrolithotomy (PCNL) surgical simulator," *Frontiers in Robotics and AI*, vol. 6, p. 145,

2019.

[9] E. M. Overtoom *et al.*, "Haptic feedback, force feedback, and force-sensing in simulation training for laparoscopy: a systematic overview," *Journal of surgical education*, vol. 76, no. 1, pp. 242–261, 2019.

[10] M. Bajka *et al.*, "Evaluation of a new virtual-reality training simulator for hysteroscopy," *Surg. Endosc.*, vol. 23, no. 9, p. 2026, 2009.

[11] G. Ahlberg *et al.*, "Proficiency-based virtual reality training significantly reduces the error rate for residents during their first 10 laparoscopic cholecystectomies," *The American journal of surgery*, vol. 193, no. 6, pp. 797–804, 2007.

[12] B. T. Bethea *et al.*, "Application of haptic feedback to robotic surgery," *Journal of Laparoendoscopic & Advanced Surgical Techniques*, vol. 14, no. 3, pp. 191–195, 2004.

[13] N. Hogan, "Impedance control: An approach to manipulation: Part i—theory," *J. Dyn. Syst. Meas. Contr.*, vol. 107, no. 1, pp. 1–7, Mar. 1985.

[14] ——, "Impedance control: An approach to manipulation: Part II-implementation," *J. Dyn. Syst. Meas. Contr.*, vol. 107, no. 1, pp. 8–16, 1985.

[15] R. J. Adams and B. Hannaford, "Stable haptic interaction with virtual environments," *IEEE Trans. Robot. Autom.*, vol. 15, no. 3, pp. 465–474, 1999.

[16] D. A. Lawrence, "Stability and transparency in bilateral teleoperation," *IEEE Trans. on Robotics and Automation*, vol. 9, no. 5, pp. 624–637, 1993.

[17] J. E. Colgate and J. M. Brown, "Factors affecting the Z-width of a haptic display," in *Proceedings of the 1994 IEEE International Conference on Robotics and Automation*, IEEE. IEEE Comput. Soc. Press, 1994, pp. 3205–3210.

[18] J. E. Colgate and G. G. Schenkel, "Passivity of a class of sampled-data systems: Application to haptic interfaces," *Journal of robotic systems*, vol. 14, no. 1, pp. 37–47, 1997.

[19] N. Hogan, "Controlling impedance at the man/machine interface," in *Proceedings, 1989 International Conference on Robotics and Automation*, IEEE. IEEE Comput. Soc. Press, 1989, pp. 1626–1631.

[20] T. Hulin, C. Preusche, and G. Hirzinger, "Stability boundary for haptic rendering: Influence of human operator," in *2008 IEEE/RSJ International Conference on Intelligent Robots and Systems*. IEEE, 2008, pp. 3483–3488.

[21] J. E. Colgate *et al.*, "Implementation of stiff virtual walls in force-reflecting interfaces," in *Proceedings of IEEE Virtual Reality Annual International Symposium*, IEEE. IEEE, 1993, pp. 202–208.

[22] N. Miandashti and M. Tavakoli, "Stability of sampled-data, delayed haptic interaction passive or active operator," *IET Control Theory & Applications*, vol. 8, no. 17, pp. 1769–1780, 2014.

[23] J. M. Brown and J. E. Colgate, *Passive implementation of multibody simulations for haptic display*. Northwestern University, 1998.

[24] M. Sreelakshmi and T. D. Subash, "Haptic technology: A comprehensive review on its applications and future prospects," *Mater. Today:. Proc.*, vol. 4, no. 2, pp. 4182–4187, 2017.

[25] V. Hayward and O. R. Astley, "Performance measures for haptic interfaces," in *Robotics research*. Springer, 1996, pp. 195–206.

[26] J. An and D.-S. Kwon, "Stability and performance of haptic interfaces with active/passive actuators-theory and experiments," *The International Journal of Robotics Research*, vol. 25, no. 11, pp. 1121–1136, 2006.

[27] N. K. Sinha, C. D. Dicenzo, and B. Szabados, "Modeling of DC motors for control applications," *IEEE Trans. Ind. Electron. Contr. Instrum.*, no. 2, pp. 84–88, 1974.

[28] T. Verstraten *et al.*, "Modeling and design of geared DC motors for energy efficiency: Comparison between theory and experiments," *Mechatronics*, vol. 30,

pp. 198–213, 2015.

[29] F. Roos, H. Johansson, and J. Wikander, "Optimal selection of motor and gearhead in mechatronic applications," *Mechatronics*, vol. 16, no. 1, pp. 63–72, 2006.

[30] R. Pastorino *et al.*, "Geared PM coreless motor modelling for driver's force feedback in steer-by-wire systems," *Mechatronics*, vol. 21, no. 6, pp. 1043–1054, 2011.

[31] H. Noma *et al.*, "The proactive desk: A new haptic display system for a digital desk using a 2-DOF linear induction motor," *Presence: Teleoperators & Virtual Environments*, vol. 13, no. 2, pp. 146–163, 2004.

[32] A. Ortega *et al.*, "Linear induction actuators for a haptic interface: a quasi-perfect transparent mechanism," in *2017 IEEE World Haptics Conference (WHC)*. IEEE, 2017, pp. 575–580.

[33] D. Senkal and H. Gurocak, "Haptic joystick with hybrid actuator using air muscles and spherical MR-brake," *Mechatronics*, vol. 21, no. 6, pp. 951–960, 2011.

[34] H. Li *et al.*, "Achieving haptic perception in forceps' manipulator using pneumatic artificial muscle," *IEEE/ASME Trans. Mechatronics*, vol. 18, no. 1, pp. 74–85, 2011.

[35] O. R. Astley and V. Hayward, "Design constraints for haptic surgery simulation," in *Proceedings 2000 ICRA. Millennium Conference. IEEE International Conference on Robotics and Automation. Symposia Proceedings (Cat. No.00CH37065)*, vol. 3, IEEE. IEEE, 2000, pp. 2446–2451.

[36] R. B. Gillespie and M. R. Cutkosky, "Stable user-specific haptic rendering of the virtual wall," in *Proceedings of the ASME International Mechanical Engineering Congress and Exhibition*, vol. 58, 1996, pp. 397–406.

[37] V. Hayward and K. E. MacLean, "Do it yourself haptics: part I," *IEEE Robotics & Automation Magazine*, vol. 14, no. 4, 2007.

[38] J. E. Colgate, M. C. Stanley, and J. M. Brown, "Issues in the haptic display of tool use," in *Proceedings 1995 IEEE/RSJ International Conference on Intelligent Robots and Systems. Human Robot Interaction and Cooperative Robots*, vol. 3, IEEE. IEEE Comput. Soc. Press, 1995, pp. 140–145.

[39] B. E. Miller, J. E. Colgate, and R. A. Freeman, "Guaranteed stability of haptic systems with nonlinear virtual environments," *IEEE Trans. Robot. Autom.*, vol. 16, no. 6, pp. 712–719, 2000.

[40] D. Weir and J. Colgate, "Stability of haptic displays," *Haptic Rendering: Foundations, Algorithms and Applications*, pp. 123–156, jul 2008.

[41] B. Hannaford and J.-H. Ryu, "Time-domain passivity control of haptic interfaces," *IEEE Trans. Robot. Autom.*, vol. 18, no. 1, pp. 1–10, 2002.

[42] J.-H. Ryu, Y. S. Kim, and B. Hannaford, "Sampled-and continuous-time passivity and stability of virtual environments," *IEEE Trans. Robot.*, vol. 20, no. 4, pp. 772–776, 2004.

[43] J.-H. Ryu *et al.*, "Time domain passivity control with reference energy following," *IEEE Trans. Control Syst. Technol.*, vol. 13, no. 5, pp. 737–742, 2005.

[44] Y. Ye, Y.-J. Pan, and Y. Gupta, "A power based time domain passivity control for haptic interfaces," in *Proceedings of the 48h IEEE Conference on Decision and Control (CDC) held jointly with 2009 28th Chinese Control Conference*. IEEE, 2009, pp. 7521–7526.

[45] J.-P. Kim, S.-Y. Baek, and J. Ryu, "A force bounding approach for multi-degree-of-freedom haptic interaction," *IEEE/ASME Trans. Mechatronics*, vol. 20, no. 3, pp. 1193–1203, 2014.

[46] C. Preusche *et al.*, "Time domain passivity control for 6 degrees of freedom haptic displays," in *Proceedings 2003 IEEE/RSJ International Conference on Intel-*

ligent Robots and Systems (IROS 2003)(Cat. No. 03CH37453), vol. 3. IEEE, 2003, pp. 2944–2949.

[47] J.-H. Ryu, D.-S. Kwon, and B. Hannaford, "Stable teleoperation with time-domain passivity control," *IEEE Trans. Robot. Autom.*, vol. 20, no. 2, pp. 365–373, 2004.

[48] T. D. C. Thanh and K. K. Ahn, "Intelligent phase plane switching control of pneumatic artificial muscle manipulators with magneto-rheological brake," *Mechatronics*, vol. 16, no. 2, pp. 85–95, 2006.

[49] W. A. Bullough *et al.*, "The electro-rheological clutch: design, performance characteristics and operation," *Proceedings of the Institution of Mechanical Engineers, Part I: Journal of Systems and Control Engineering*, vol. 207, no. 2, pp. 87–95, 1993.

[50] O. Erol *et al.*, "Magnetic induction control with embedded sensor for elimination of hysteresis in magnetorheological brakes," *J. Intell. Mater. Syst. Struct.*, vol. 23, no. 4, pp. 427–440, 2012.

[51] C. Rossa *et al.*, "Development of a multilayered wide-ranged torque magnetorheological brake," *Smart Mater. Struct.*, vol. 23, no. 2, p. 025028, 2014.

[52] O. Erol and H. Gurocak, "Interactive design optimization of magnetorheological-brake actuators using the Taguchi method," *Smart Mater. Struct.*, vol. 20, no. 10, p. 105027, 2011.

[53] Y.-M. Han and S.-B. Choi, "Control of an ER haptic master in a virtual slave environment for minimally invasive surgery applications," *Smart Mater. Struct.*, vol. 17, no. 6, p. 065012, 2008.

[54] D. Shin, X. Yeh, and O. Khatib, "A new hybrid actuation scheme with artificial pneumatic muscles and a magnetic particle brake for safe human–robot collaboration," *The International Journal of Robotics Research*, vol. 33, no. 4, pp. 507–518, 2014.

[55] F. Conti and O. Khatib, "A new actuation approach for haptic interface design," *The International Journal of Robotics Research*, vol. 28, no. 6, pp. 834–848, 2009.

[56] E. Simeu and D. Georges, "Modeling and control of an eddy current brake," *Control Eng. Pract.*, vol. 4, no. 1, pp. 19–26, 1996.

[57] A. H. C. Gosline and V. Hayward, "Eddy current brakes for haptic interfaces: Design, identification, and control," *IEEE/ASME Trans. Mechatronics*, vol. 13, no. 6, pp. 669–677, 2008.

[58] M. R. Reed and W. J. Book, "Modeling and control of an improved dissipative passive haptic display," in *Proceedings of IEEE International Conference on Robotics and Automation*, vol. 1. IEEE, 2004, pp. 311–318.

[59] O. Topçu *et al.*, "Experimental investigation of a magneto-rheological fluid damper with permanent magnet for haptic finger grasping," in *Machine Vision and Mechatronics in Practice*. Springer, 2015, pp. 105–112.

[60] D. Karnopp, "Computer simulation of stick-slip friction in mechanical dynamic systems," *J. Dyn. Syst. Meas. Contr.*, vol. 107, no. 1, pp. 100–103, 1985.

[61] D. K. Swanson and W. J. Book, "Obstacle avoidance methods for a passive haptic display," in *2001 IEEE/ASME International Conference on Advanced Intelligent Mechatronics. Proceedings (Cat. No.01TH8556)*, vol. 2, IEEE. IEEE, 2001, pp. 1187–1192.

[62] J. Furusho *et al.*, "Development of ER brake and its application to passive force display," *J. Intell. Mater. Syst. Struct.*, vol. 13, no. 7-8, pp. 425–429, 2002.

[63] C. Melchiorri, M. Montanari, and G. Vassura, "Control strategies for a defective, wire-based, haptic interface," in *Intelligent Robots and Systems, 1997. IROS'97., Proceedings of the 1997 IEEE/RSJ International Conference on*, vol. 1. IEEE, 1997, pp. 181–187.

[64] C. Cho, M. Kim, and J.-B. Song, "Direct control of a passive haptic device based on passive force manipulability ellipsoid analysis," *International Journal of Control, Automation, and Systems*, vol. 2, no. 2, pp. 238–246, 2004.

[65] S. Katsura, Y. Matsumoto, and K. Ohnishi, "Analysis and experimental validation of force bandwidth for force control," *IEEE Trans. Ind. Electron.*, vol. 53, no. 3, pp. 922–928, 2006.

[66] C. Cho, J.-B. Song, and M. Kim, "Energy-based control of a haptic device using brakes," *IEEE Trans. Syst., Man, Cybern.*, vol. 37, no. 2, pp. 341–349, 2007.

[67] C.-M. Chew, G.-S. Hong, and W. Zhou, "Series damper actuator: a novel force/torque control actuator," in *4th IEEE/RAS International Conference on Humanoid Robots, 2004.*, vol. 2. IEEE, 2004, pp. 533–546.

[68] A. Mohand-Ousaid *et al.*, "Haptic interface transparency achieved through viscous coupling," *The International Journal of Robotics Research*, vol. 31, no. 3, pp. 319–329, 2012.

[69] B. DeBoon *et al.*, "Differentially-clutched series elastic actuator for robot-aided musculoskeletal rehabilitation," in *2019 International Conference on Robotics and Automation (ICRA)*. IEEE, 2019, pp. 1507–1513.

[70] M. Badescu, C. Wampler, and C. Mavroidis, "Rotary haptic knob for vehicular instrument controls," in *Haptic Interfaces for Virtual Environment and Teleoperator Systems, 2002. HAPTICS 2002. Proceedings. 10th Symposium on.* ieee, 2002, pp. 342–343.

[71] J. Chen and W.-H. Liao, "Design and testing of assistive knee brace with magnetorheological actuator," in *Robotics and Biomimetics, 2008. ROBIO 2008. IEEE International Conference on.* IEEE, 2009, pp. 512–517.

[72] J. An and D.-S. Kwon, "Haptic experimentation on a hybrid active/passive force feedback device," in *Robotics and Automation, 2002. Proceedings. ICRA'02. IEEE International Conference on*, vol. 4. IEEE, 2002, pp. 4217–4222.

[73] O. Baser, E. ilhan Konukseven, and H. Gurocak, "Stability and transparency improvement in haptic device employing both MR-brake and active actuator," in *RO-MAN, 2012 IEEE*. IEEE, 2012, pp. 12–18.

[74] Y.-J. Nam and M.-K. Park, "A hybrid haptic device for wide-ranged force reflection and improved transparency," in *2007 International Conference on Control, Automation and Systems*. IEEE, 2007, pp. 1015–1020.

[75] T.-B. Kwon and J.-B. Song, "Force display using a hybrid haptic device composed of motors and brakes," *Mechatronics*, vol. 16, no. 5, pp. 249–257, 2006.

[76] J. Troccaz, M. Peshkin, and B. Davies, "Guiding systems for computer-assisted surgery: introducing synergistic devices and discussing the different approaches," *Med. Image Anal.*, vol. 2, no. 2, pp. 101–119, 1998.

[77] C. Rossa, J. Lozada, and A. Micaelli, "Design and control of a dual unidirectional brake hybrid actuation system for haptic devices," *IEEE Trans. Haptics*, vol. 7, no. 4, pp. 442–453, 2014.

[78] B. Gonenc and H. Gurocak, "Virtual needle insertion with haptic feedback using a hybrid actuator with DC servomotor and MR-brake with hall-effect sensor," *Mechatronics*, vol. 22, no. 8, pp. 1161–1176, 2012.

[79] ——, "Virtual tissue cutting with haptic feedback using a hybrid actuator with DC servomotor and magnetorheological brake," *J. Comput. Inf. Sci. Eng.*, vol. 16, no. 3, p. 030902, 2016.

[80] O. Baser, H. Gurocak, and E. I. Konukseven, "Hybrid control algorithm to improve both stable impedance range and transparency in haptic devices," *Mechatronics*, vol. 23, no. 1, pp. 121–134, 2013.

[81] Y.-J. Nam, Y.-J. Moon, and M.-K. Park, "Performance improvement of a rotary MR fluid actuator based on electromagnetic design," *J. Intell. Mater. Syst. Struct.*, vol. 19, no. 6, pp. 695–705, 2008.

[82] D. Bi *et al.*, "Friction modeling and compensation for haptic display based on support vector machine," *IEEE Trans. Ind. Electron.*, vol. 51, no. 2, pp. 491–500, 2004.

[83] Y.-Q. Yu and J. Lin, "Active balancing of a flexible linkage with redundant drives," *J. Mech. Des.*, vol. 125, no. 1, pp. 119–123, 2003.

[84] J. J. Gil, A. Rubio, and J. Savall, "Decreasing the apparent inertia of an impedance haptic device by using force feedforward," *IEEE Trans. Control Syst. Technol.*, vol. 17, no. 4, pp. 833–838, 2009.

[85] A. Sharon and D. Hardt, "Enhancement of robot accuracy using endpoint feedback and a macro-micro manipulator system," in *1984 American Control Conference*. IEEE, 1984, pp. 1836–1845.

[86] A. Sharon, N. Hogan, and D. E. Hardt, "High bandwidth force regulation and inertia reduction using a macro/micro manipulator system," in *Proceedings of 1988 IEEE International Conference on Robotics and Automation*. IEEE, 1988, pp. 126–132.

[87] L. Stocco and S. E. Salcudean, "A coarse-fine approach to force-reflecting hand controller design," in *Proceedings of 1996 IEEE International Conference on Robotics and Automation*, vol. 1. IEEE, 1996, pp. 404–410.

[88] S. A. Wall and W. Harwin, "A high bandwidth interface for haptic human computer interaction," *Mechatronics*, vol. 11, no. 4, pp. 371–387, 2001.

[89] D. S. Walker, D. J. Thoma, and G. Niemeyer, "Variable impedance magnetorheological clutch actuator and telerobotic implementation," in *Intelligent Robots and Systems, 2009. IROS 2009. IEEE/RSJ International Conference on*. IEEE, 2009, pp. 2885–2891.

[90] P. Fauteux *et al.*, "Dual-differential rheological actuator for high-performance physical robotic interaction," *IEEE Trans. Robot.*, vol. 26, no. 4, pp. 607–618, 2010.

[91] J.-S. Oh and S.-B. Choi, "State of the art of medical devices featuring smart electro-rheological and magneto-rheological fluids," *Journal of King Saud University-Science*, vol. 29, no. 4, pp. 390–400, 2017.

[92] A. Bolopion and S. Régnier, "A review of haptic feedback teleoperation systems for micromanipulation and microassembly," *IEEE Trans. Autom. Sci. Eng.*, vol. 10, no. 3, pp. 496–502, 2013.

[93] D. Escobar-Castillejos *et al.*, "A review of simulators with haptic devices for medical training," *J. Med. Syst.*, vol. 40, no. 4, p. 104, 2016.

[94] P. Xia, "New advances for haptic rendering: state of the art," *The Visual Computer*, vol. 34, no. 2, pp. 271–287, 2018.

[95] E. Samur, *Performance metrics for haptic interfaces*. Springer Science & Business Media, 2012.

[96] C. Cho, J.-B. Song, and M. Kim, "Design and control of a planar haptic device with passive actuators based on passive force manipulability ellipsoid (FME) analysis," *Journal of Robotic Systems*, vol. 22, no. 9, pp. 475–486, 2005.

[97] H. Davis and W. Book, "Torque control of a redundantly actuated passive manipulator," in *Proceedings of the 1997 American Control Conference (Cat. No. 97CH36041)*, vol. 2. IEEE, 1997, pp. 959–963.

[98] S. Munir, L. Tognetti, and W. J. Book, "Experimental evaluation of a new braking system for use in passive haptic displays," in *Proceedings of the 1999 American Control Conference*, vol. 6. IEEE, 1999, pp. 4456–4460.

[99] D. Senkal, H. Gurocak, and E. I. Konukseven, "Passive haptic interface with mr-brakes for dental implant surgery," *Presence: Teleoperators and Virtual Environments*, vol. 20, no. 3, pp. 207–222, 2011.

[100] S.-R. Lee *et al.*, "Repulsive force control of minimally invasive surgery robot associated with three degrees of freedom electrorheological fluid-based haptic

master," *Proceedings of the Institution of Mechanical Engineers, Part C: Journal of Mechanical Engineering Science*, vol. 228, no. 9, pp. 1606–1621, 2014.

[101] J.-S. Oh *et al.*, "A 4-DOF haptic master using er fluid for minimally invasive surgery system application," *Smart Mater. Struct.*, vol. 22, no. 4, p. 045004, 2013.

[102] S.-R. Kang *et al.*, "Controllable magnetorheological fluid based actuators for 6-degree-of-freedom haptic master applicable to robot-assisted surgery," *Sens. Actuators, A*, vol. 279, pp. 649–662, 2018.

[103] W. J. Book *et al.*, "The concept and implementation of a passive trajectory enhancing robot," in *Intelligent Machine Dynamics Laboratory Publications*. Georgia Institute of Technology, 1996.

[104] C. Cho, M. Kim, and J.-B. Song, "Performance analysis of a 2-link haptic device with electric brakes," in *Proceedings of 11th Symposium on Haptic Interfaces for Virtual Environment and Teleoperator Systems.* IEEE, 2003, pp. 47–53.

[105] J. Wang and C. M. Gosselin, "Static balancing of spatial four-degree-of-freedom parallel mechanisms," *Mech. Mach. Theory*, vol. 35, no. 4, pp. 563–592, 2000.

[106] A. Mashayekhi *et al.*, "VirSense: A novel haptic device with fixed-base motors and a gravity compensation system," *Industrial Robot*, 2014.

[107] J. An and D.-S. Kwon, "Five-bar linkage haptic device with DC motors and MR brakes," *J. Intell. Mater. Syst. Struct.*, vol. 20, no. 1, pp. 97–107, 2009.

[108] M. Zinn *et al.*, "A new actuation approach for human friendly robot design," *The International Journal of Robotics Research*, vol. 23, no. 4-5, pp. 379–398, 2004.

[109] ——, "Large workspace haptic devices-a new actuation approach," in *2008 Symposium on Haptic Interfaces for Virtual Environment and Teleoperator Systems.* IEEE, 2008, pp. 185–192.

[110] O. Schneider and J. Troccaz, "A six-degree-of-freedom passive arm with dynamic constraints (PADyC) for cardiac surgery application: Preliminary experiments," *Comput. Aided Surg.*, vol. 6, no. 6, pp. 340–351, 2001.

[111] S. Hirose and S. Ma, "Coupled tendon-driven multijoint manipulator," in *Proceedings. 1991 IEEE International Conference on Robotics and Automation.* IEEE, 1991, pp. 1268–1275.

[112] M. Kaneko, T. Yamashita, and K. Tanie, "Basic considerations on transmission characteristics for tendon drive robots," in *Fifth International Conference on Advanced Robotics' Robots in Unstructured Environments.* IEEE, 1991, pp. 827–832.

[113] J.-P. Merlet, *Parallel Robots*, 2nd ed. Springer Netherlands, 2000, vol. 128.

[114] C. Våpenstad *et al.*, "Limitations of haptic feedback devices on construct validity of the LapSim® virtual reality simulator," *Surg. Endosc.*, vol. 27, no. 4, pp. 1386–1396, 2013.

[115] ——, "Perceiving haptic feedback in virtual reality simulators," *Surg. Endosc.*, vol. 27, no. 7, pp. 2391–2397, 2013.

[116] ——, "Lack of transfer of skills after virtual reality simulator training with haptic feedback," *Minimally Invasive Therapy & Allied Technologies*, vol. 26, no. 6, pp. 346–354, 2017.

[117] J. Duffy, *Statics and Kinematics with Applications to Robotics.* Cambridge University Press, 1996.

[118] X.-D. Pang, H. Z. Tan, and N. I. Durlach, "Manual discrimination of force using active finger motion," *Perception & psychophysics*, vol. 49, no. 6, pp. 531–540, 1991.

[119] J. Voisin, Y. Lamarre, and C. E. Chapman, "Haptic discrimination of object shape in humans: contribution of cutaneous and proprioceptive inputs," *Exp. Brain Res.*, vol. 145, no. 2, pp. 251–260, 2002.

[120] S. Briot and I. A. Bonev, "Are parallel robots more accurate than serial robots?" *Transactions of the Canadian Society for Mechanical Engineering*, vol. 31, no. 4, pp. 445–455, 2007.

[121] C. M. Gosselin, "Dexterity indices for planar and spatial robotic manipulators," in *Proceedings., IEEE International Conference on Robotics and Automation*. IEEE, 1990, pp. 650–655.

[122] C. Gosselin and J. Angeles, "A global performance index for the kinematic optimization of robotic manipulators," *J. Mech. Des.*, vol. 113, no. 3, pp. 220–226, 1991.

[123] A. Bowling and O. Khatib, "The dynamic capability equations: a new tool for analyzing robotic manipulator performance," *IEEE Trans. Robot.*, vol. 21, no. 1, pp. 115–123, 2005.

[124] H. Asada, "A geometrical representation of manipulator dynamics and its application to arm design," *J. Dyn. Syst. Meas. Contr.*, vol. 105, no. 3, pp. 131–142, 1983.

[125] A. Bicchi and D. Prattichizzo, "Manipulability of cooperating robots with unactuated joints and closed-chain mechanisms," *IEEE Trans. Robot. Autom.*, vol. 16, no. 4, pp. 336–345, 2000.

[126] S. L. Chiu, "Task compatibility of manipulator postures," *The International Journal of Robotics Research*, vol. 7, no. 5, pp. 13–21, 1988.

[127] G. T. Pond and J. A. Carretero, "Quantitative dexterous workspace comparison of serial and parallel planar mechanisms," in *Parallel Manipulators, New Developments*. IntechOpen, 2008.

[128] S. Cubero, *Industrial robotics: Theory, modelling and control*. Pro Literatur Verlag, 2006.

[129] X.-J. Liu, J. Wang, and G. Pritschow, "Kinematics, singularity and workspace of planar 5R symmetrical parallel mechanisms," *Mech. Mach. Theory*, vol. 41,

no. 2, pp. 145–169, 2006.

[130] C. Rossa and M. Tavakoli, "Issues in closed-loop needle steering," *Control Eng. Pract.*, vol. 62, pp. 55–69, 2017.

[131] T. R. Coles, D. Meglan, and N. W. John, "The role of haptics in medical training simulators: A survey of the state of the art," *IEEE Trans. Haptics*, vol. 4, no. 1, pp. 51–66, 2010.

[132] C. G. Corrêa *et al.*, "Haptic interaction for needle insertion training in medical applications: The state-of-the-art," *Medical engineering & physics*, 2018.

[133] T. A. Kern, *Engineering Haptic Devices*, C. Hatzfeld and T. A. Kern, Eds. Springer London, 2014.

[134] A. M. Okamura, C. Simone, and M. D. O'leary, "Force modeling for needle insertion into soft tissue," *IEEE Trans. Biomed. Eng.*, vol. 51, no. 10, pp. 1707–1716, 2004.

[135] R. E. Stamper, "A three degree of freedom parallel manipulator with only translational degrees of freedom," Ph.D. dissertation, University of Maryland, 1997.

[136] N. Karbasizadeh *et al.*, "Experimental dynamic identification and model feed-forward control of novint falcon haptic device," *Mechatronics*, vol. 51, pp. 19–30, 2018.

[137] D. J. Block, M. B. Michelotti, and R. S. Sreenivas, "Application of the novint falcon haptic device as an actuator in real-time control," *Paladyn, Journal of Behavioral Robotics*, vol. 4, no. 3, pp. 182–193, 2013.

[138] S. Amat, S. Busquier, and Á. Magreñán, "Reducing chaos and bifurcations in newton-type methods," in *Abstract and applied analysis*, vol. 2013. Hindawi, 2013.

[139] *Magnetic Particle Brake B2*, Placid Industries, [Datasheet]. Available: www.placidindustries.com/wp-content/uploads/downloads/B2-metric-data-sheet.pdf. Accessed Sep, 21, 2019.

[140] C. Rossa *et al.*, "Design considerations for magnetorheological brakes," *IEEE/ASME Trans. Mechatronics*, vol. 19, no. 5, pp. 1669–1680, 2013.

[141] S. Komada and K. Ohnishi, "Force feedback control of robot manipulator by the acceleration tracing orientation method," *IEEE Trans. Ind. Electron.*, vol. 37, no. 1, pp. 6–12, 1990.

[142] S. Komada *et al.*, "Robust force control based on compensation for parameter variations of dynamic environment," *IEEE Trans. Ind. Electron.*, vol. 40, no. 1, pp. 89–95, 1993.

[143] T. Murakami, F. Yu, and K. Ohnishi, "Torque sensorless control in multidegree-of-freedom manipulator," *IEEE Trans. Ind. Electron.*, vol. 40, no. 2, pp. 259–265, 1993.

[144] W.-H. Chen *et al.*, "A nonlinear disturbance observer for robotic manipulators," *IEEE Trans. Ind. Electron.*, vol. 47, no. 4, pp. 932–938, 2000.

[145] M. H. Korayem and R. Haghighi, "Nonlinear disturbance observer for robot manipulators in 3d space," in *International Conference on Intelligent Robotics and Applications*. Springer, 2008, pp. 14–23.

[146] A. Nikoobin and R. Haghighi, "Lyapunov-based nonlinear disturbance observer for serial n-link robot manipulators," *J. Intell. Rob. Syst.*, vol. 55, no. 2-3, pp. 135–153, 2009.

[147] A. Gupta and M. K. O'Malley, "Disturbance-observer-based force estimation for haptic feedback," *J. Dyn. Syst. Meas. Contr.*, vol. 133, no. 1, 2011.

[148] J. de Dios Flores-Mendez *et al.*, "Impedance control and force estimation of a redundant parallel kinematic manipulator," in *International Conference on Informatics in Control, Automation and Robotics*. Springer, 2017, pp. 174–191.

[149] A. Mohammadi, H. J. Marquez, and M. Tavakoli, "Nonlinear disturbance observers: design and applications to euler lagrange systems," *IEEE Control Syst.*

Mag., vol. 37, no. 4, pp. 50–72, 2017.

[150] B. T. Diep, N. Vo, and T. D. Le, "Hysteresis identification of bidirectional magneto-rheological actuators employing preisach model," in *Applied Mechanics and Materials*, vol. 889. Trans Tech Publ, 2019, pp. 355–360.

[151] J. Å. Stakvik *et al.*, "On implementation of the preisach model: Identification and inversion for hysteresis compensation," *Modeling, Identification and Control: A Norwegian Research Bulletin*, vol. 36, no. 3, pp. 133–142, 2015.

[152] S. Briot and W. Khalil, *Dynamics of Parallel Robots*. Springer International Publishing, 2015.

[153] M. Ismail, F. Ikhouane, and J. Rodellar, "The hysteresis Bouc-Wen model, a survey," *Arch. Comput. Methods Eng.*, vol. 16, no. 2, pp. 161–188, 2009.